Journal of
Mechanics of
Materials and Structures

JOURNAL OF MECHANICS OF MATERIALS AND STRUCTURES

msp.org/jomms

Founded by Charles R. Steele and Marie-Louise Steele

Cover photo: Ev Shafrir

∎msp

FLEXURAL BEHAVIOR OF FUNCTIONALLY GRADED SLENDER BEAMS WITH COMPLEX CROSS-SECTION

GHOLAMALI SHARIFISHOURABI, AMRAN AYOB, SCOTT GOHERY,
MOHD YAZID BIN YAHYA, SHOKROLLAH SHARIFI AND ZORA VRCELJ

Deflection and stress analyses of functionally graded beams with complex cross-section and general material variation, under transverse loading, were carried out. The elastic-fundamental solution is used to derive equations satisfied by the normal stresses in arbitrary cross-sections of the beam, assuming that the plane sections remain plane and normal to the beam axis. The technique was verified by existing analytical and finite element models. Numerical experiments were then performed where the material properties vary through thickness or width of the beams according to power-law and exponential gradations. It was found that the quality of material gradation affects the deflection, stresses and neutral axis position significantly. It is concluded that the technique is useful for the elastic behavior analysis of FGBs with complex cross-sections and various material gradations.

1. Introduction

Over the past decades, composite materials with asymmetric material variation, such as asymmetric smart composites [Sharifishourabi et al. 2014a] and functionally graded materials (FGMs) have received the attention of both theoretical and experimental researchers. FGM is a class of material similar to an advanced composite that has a heterogeneous structure in which the constituent varies smoothly, gradually, and continuously from one surface to another. This gradual variation results also in a gradual change in the mechanical and thermal properties [Suresh and Mortensen 1998]. FGMs have the best properties of both ceramics, such as low density, high strength, high stiffness, and temperature resistance, and of metals, such as toughness, electrical conductivity, and machinability. Due to these outstanding properties, FGMs have attracted much attention in industries in many engineering fields such as aerospace, automotive, and the biomedical fields [Miyamoto et al. 1999]. Over the last decades, along with rapid growth in the use of FGMs, different methods have also been developed for analyzing their mechanical behavior [Menaa et al. 2012; Shahba et al. 2013; Ke et al. 2009].

Beams, as the most common engineering structures, are traditionally used as an example. The first exact elasticity solution for a functionally graded beam (FGB) subjected to transverse loads was developed by Sankar [2001]. He assumed that the Poisson's ratio is constant and the elastic modulus of the FGB varies exponentially across the thickness. He also developed the simple Euler–Bernoulli beam theory for FGBs under transverse loads, which is only applicable for long and slender beams with depthwise and exponential variation of materials. Then, Sankar and Tzeng [2002] obtained an exact elasticity solution by solving the thermoelastic governing equations for FGBs subjected to thermal loads. They

showed that when the variation of the material properties was opposite to the distribution of temperature, the residual stresses due to the thermal loading were reduced. Chakraborty et al. [2003], based on the theory of first-order shear deformation, developed a new beam finite element for analyzing the thermal and mechanical behavior of FGBs. They solved static, wave propagation, and free vibration problems considering both exponential and power-law variations of the mechanical and thermal properties. An elastic solution for sandwich beams having an FGM core with exponential variation was obtained by Venkataraman and Sankar [2003]. They employed the Euler–Bernoulli beam theory for modeling the face sheets, and plane elasticity equations for analyzing the core. Numerical solutions based on the meshless local Petrov–Galerkin method (MLPG) for two-dimensional FG elastic solids subjected to thermal and mechanical loads were obtained by Ching and Yen [2005]. They also obtained transient thermoelastic deformations for two-dimensional FGBs subjected to a nonuniform heat supply [Ching and Yen 2006]. Effect of material gradation on thermomechanical stresses in functionally graded beams was studied by Sharifishourabi et al. [2012]. They also developed a tensile testing machine for FG specimens [Sharifishourabi et al. 2014b]. Lü et al. [2006], by employing the state space method, presented a two-dimensional solution for the thermoelastic analysis of thick FGBs. Ding et al. [2007] presented an elasticity solution for plane anisotropic FGBs. They assumed that the material variation was according to an arbitrary function of the thickness direction. Kadoli et al. [2008] studied the static stresses and deflection of FGBs under ambient temperature using higher-order shear deformation beam theory. Free vibration analysis of FGBs was also studied in depth, and several solutions have been presented [Aydogdu and Taskin 2007; Sina et al. 2009; Wattanasakulpong et al. 2012]. Ying et al. [2008] studied an FGB with exponential material variation resting on an elastic foundation. They presented exact solutions based on the two-dimensional theory of elasticity for the free vibration and bending of orthotropic FGBs. Zhong and Yu [2007] developed a two-dimensional analytical solution by using the Airy stress function method for a cantilever FGB with arbitrary variations of material under various loads. Li [2008] introduced a new unified method for the static and dynamic analysis of Euler–Bernoulli and Timoshenko FGBs with shear deformation and rotary inertia. An analytical approach for the free vibration response of FGBs in the case of temperature dependence with arbitrary boundary conditions has been introduced by Mahi et al. [2010]. They assumed that the material properties are temperature-dependent and vary according to the exponential or power-law forms along the thickness of the beam. Hamed [2012] and Piovan et al. [2012] studied the buckling response of FGBs. Numerical and analytical approaches were presented for deflections of FGBs subjected to inclined and transverse loading [Rahimi and Davoudinik 2010; Farhatnia et al. 2009].

A free vibration analysis of functionally graded spatial curved beams on the basis of first-order shear deformation theory was carried out by Yousefi and Rastgoo [2011]. The nonlinear forced vibration analysis of clamped FGBs was also studied by Shooshtari and Rafiee [2011]. Yaghoobi and Feridoon [2010] investigated the effect of neutral surface location on the deflection of FGBs subjected to a uniform distributed loading. Thai and Vo [2012] presented analytical solutions for the bending and free vibration of FGBs using Hamilton's principle and other higher-order shear deformation beam theories. An experimental work to validate a model based on third-order zigzag theory for the bending and free vibration response of layered FGBs was carried out by Kapuria et al. [2008]. They used the modified rule of mixtures to obtain the effective Young's modulus. Apetre et al. [2008] investigated several existing theories for sandwich beams to determine their appropriateness for sandwich plates with a functionally graded core.
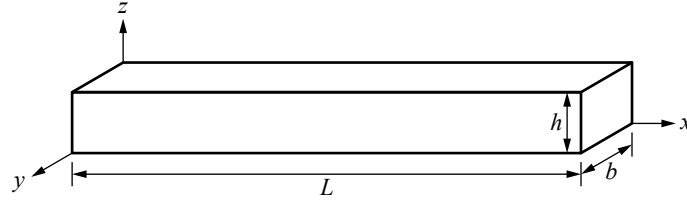
Figure 1. Geometry and coordinates of an FGB.

They found good agreement between the results of the finite element method, the higher-order theory, and the Fourier–Galerkin method. The bending of cantilever FGBs subjected to an end force using small and large deformation theories was investigated by Kang and Li [2009]. They investigated the influence of a nonlinearity parameter and Young's modulus on the rotations and deflections. A free and forced vibration analysis for FGBs under a concentrated moving harmonic loading by employing Lagrange's equations and the Euler–Bernoulli beam theory was carried out by Şimşek and Kocatürk [2009]. A free vibration and stability analysis of tapered FGBs with axial gradation of material, based on the Euler–Bernoulli beam theory, was studied by Shahba and Rajasekaran [2012]. A mechanical behavior analysis of FGBs employing the theory of directed curves was carried out by Bîrsan et al. [2012]. They presented a general analytical solution using the effective stiffness properties for beams with arbitrary cross-sectional shape.

Although several analytical solutions are available, the majority of these solutions involve cumbersome calculations to apply them to complex geometries. On the other hand, previous studies only focused on FGBs with material gradation along the thickness direction, while there are many applications of FGBs in which the material properties vary through the width of the beam. This study attempts to use a technique simpler than the currently available ones. For simplicity, the method is compared with applicable models for static analysis of FGBs with complex cross-section and general material gradation along either the thickness or width direction of the beam.

2. Problem formulation and solution

Figure 1 shows the geometry and coordinate system of a FGB. The length, width, and thickness of the beam are L, b, and h, respectively. The coordinate system originates at the corner of the cross section of the beam. The material properties vary continuously and gradually across the thickness or width according to arbitrary functions. Two examples of possible material gradation for FGBs are shown in Figure 2. Since the power-law and exponential law are the two most common models, here these material variations will also be considered. The power-law modeling which is introduced by Wakashima et al.
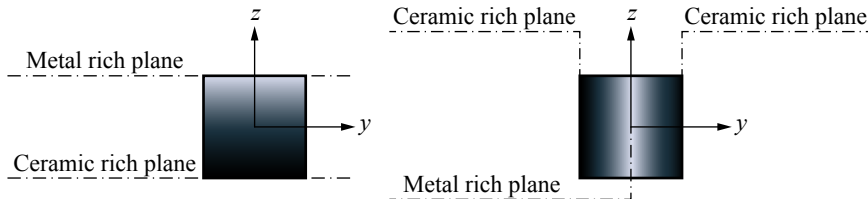
Figure 2. Two examples of possible material gradations for FGBs.

[1990] is given by

$$p(z) = (p_m - p_c)\left(\frac{z}{h} + \frac{1}{2}\right)^n + p_c. \tag{1}$$

The exponential law, which is more favorable, is given by

$$p(z) = p_m \exp(-\delta(1 - 2z/h)), \quad \delta = \tfrac{1}{2}\log\frac{p_m}{p_c}. \tag{2}$$

Since this study attempts to use a simple and applied technique for FGBs with complicated geometry and material variation, these basic assumptions were made:

(1) The classical Euler–Bernoulli beam theory was applied.

(2) The Poisson's ratio was held constant.

(3) The normal stresses σ_{zz} were assumed to be negligible.

The classical strain-stress relations for a homogenous beam are given by

$$\sigma_x = E\epsilon_x, \tag{3}$$

$$\tau_{xz} = G\gamma_{xz}. \tag{4}$$

The normal strain ϵ_x, based on the assumptions, takes the form

$$\epsilon_x = \epsilon_{x_0} + z\kappa, \tag{5}$$

where ϵ_{x_0}, κ, and z are the middle plane strain, the curvature, and the distance from the neutral axis of the beam. The axial force (N), bending moment (M), and shear force (V) resultants, based on the classical beam theory, are

$$N = \int_0^h \sigma_x \, dA, \tag{6}$$

$$M = \int_0^h z\sigma_x \, dA, \tag{7}$$

$$V = \int_0^h \tau_{xz} \, dA. \tag{8}$$

Since no assumption was made regarding the material of the beam in deriving equations (5)–(8), they are still valid for FGBs. While (8) is typically neglected due to its insignificant value, (3) and (4) for FGBs become the following equations, given by Sankar [2001]:

$$\sigma_x = E(z)\epsilon_x, \tag{9}$$

$$\tau_{xz} = G(z)\gamma_{xz}. \tag{10}$$

The axial force (N) and bending moment (M) resultants for a discretized beam cross-section can be

derived, based on the classical beam theory, as

$$N = \sum_{i=1}^{m} \int_{\frac{h}{m}(i-1)}^{\frac{h}{m}i} \sigma_i \, dA, \tag{11}$$

$$M = \sum_{i=1}^{m} \int_{\frac{h}{m}(i-1)}^{\frac{h}{m}i} z\sigma_i \, dA. \tag{12}$$

In these equations, m indicates the total numbers of sublayers (see Figure 3). By substituting (9) in (11) and (12), the resultant force and moment expressions under bending are

$$N = \sum_{i=1}^{m} \int_{\frac{h}{m}(i-1)}^{\frac{h}{m}i} E_i b_i \epsilon_x \, dz = 0, \tag{13}$$

$$M = \sum_{i=1}^{m} \int_{\frac{h}{m}(i-1)}^{\frac{h}{m}i} z E_i b_i \epsilon_x \, dz, \tag{14}$$

where E_i and b_i denote the values of the Young's modulus and the width in the i-th sublayer. By substituting (5) in (13) and (14), we get the system of equations

$$\begin{cases} \sum_{i=1}^{m} \int_{\frac{h}{m}(i-1)}^{\frac{h}{m}i} E_i b_i (\epsilon_{x_0} + z\kappa) \, dz = 0, \\ \sum_{i=1}^{m} \int_{\frac{h}{m}(i-1)}^{\frac{h}{m}i} z E_i b_i (\epsilon_{x_0} + z\kappa) \, dz = M. \end{cases} \tag{15}$$

This system of equations can be written in the short form

$$\begin{cases} \tilde{A}\epsilon_{x_0} + \tilde{Q}\kappa = 0, \\ \tilde{Q}\epsilon_{x_0} + \tilde{I}\kappa = M. \end{cases} \tag{16}$$

Using definitions (17)–(19), the values of ϵ_{x_0} and κ can be obtained as

$$\tilde{I} = \sum_{i=1}^{m} \int_{\frac{h}{m}(i-1)}^{\frac{h}{m}i} z^2 E_i b_i \, dz, \tag{17}$$
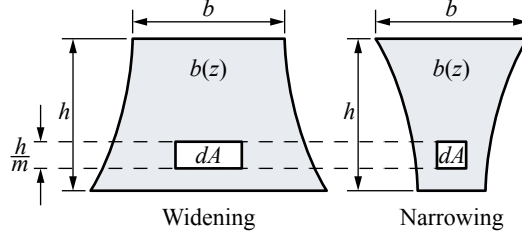
$$\tilde{A} = \sum_{i=1}^{m} \int_{\frac{h}{m}(i-1)}^{\frac{h}{m}i} E_i b_i \, dz, \tag{18}$$

$$\tilde{Q} = \sum_{i=1}^{m} \int_{\frac{h}{m}(i-1)}^{\frac{h}{m}i} z E_i b_i \, dz, \tag{19}$$

$$\epsilon_{x_0} = \frac{-\tilde{Q}M}{(-\tilde{Q}^2 + \tilde{A}\tilde{I})}, \tag{20}$$

$$\kappa = \frac{\tilde{A}M}{(-\tilde{Q}^2 + \tilde{A}\tilde{I})}. \tag{21}$$

Figure 3. Schematic of discretized graded beams.

Furthermore, one can see that the position of the neutral axis is located at

$$a = \frac{\tilde{Q}}{\tilde{A}}. \tag{22}$$

Then, substituting (20), (21) and (5) into (9), the depthwise axial stresses in a discretized graded beam subjected to pure bending can be obtained as

$$\sigma_x(x, z) = E(z)(\epsilon_{x_0} + z\kappa) = \frac{M(x)(z\tilde{A} - \tilde{Q})}{-\tilde{Q}^2 + \tilde{A}\tilde{I}} E(z). \tag{23}$$

Shear stress in the FGB can be easily obtained from the famous differential equation of equilibrium as

$$\tau_{xz}(x, z) = \int_0^z \frac{\partial \sigma_x(x, z)}{\partial x} \, dz. \tag{24}$$

Substituting (3) and (5) into (7) leads to

$$\kappa = \frac{M(x)}{D} = \frac{d^2 w}{dx^2}. \tag{25}$$

The bending rigidity D can be obtained as

$$D = E_h(\tilde{I} - \tilde{A}\tilde{z}^2), \tag{26}$$

where E_h is the Young's modulus of the surface with higher modulus. By integrating both sides of (25) with respect to x and applying the loads and boundary conditions, the deflections along the length of the FGB ($w(x)$) will be obtained. The boundary conditions for a simply supported beam are
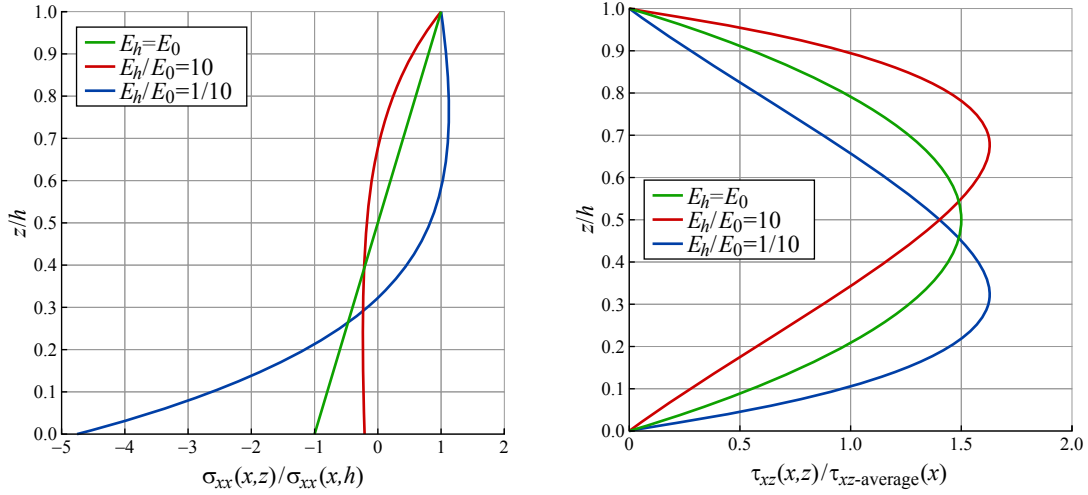
$$w(0) = 0, \quad w(L) = 0. \tag{27}$$

The boundary conditions for a cantilever beam are

$$w(0) = 0, \quad \frac{dw}{dx}(0) = 0. \tag{28}$$

3. Results and discussion

After validating the technique, numerical solutions are applied using the above equations for static analysis of FGBs with complex cross-section and material variation.

Figure 4. Left: distribution of depthwise normalized axial stresses σ_{xx} for the simply supported FGB under transverse distributed loads. Right: distribution of depthwise normalized shear stresses τ_{xz} for the simply supported FGB under transverse distributed loads.

3.1. *Validation.* To evaluate the accuracy of this method, the same beam problem solved analytically by Sankar [2001] was studied again using the presented technique ($m = 100$). Figure 4 shows the depthwise normalized axial and transverse shear stress distributions for a simply supported FGB subjected to transverse distributed loads. The Young's modulus of the beam was assumed to vary exponentially along the thickness from E_0 at the bottom to E_h at the topmost surface. The axial stresses were normalized by dividing by the corresponding stress on the top surface and the shear stresses were normalized with respect to the average shear stress at the same cross-section. Since the present solution and that of Sankar [2001] were based on the same assumptions, the results were obviously the same.

Furthermore, to find out the accuracy range of this method, the same cantilever FGB studied by Chakraborty et al. [2003] was solved again. An FGB with unit width and length of $L = 0.5$ m is subjected to a unit transverse load at the tip. Steel and alumina are considered as the topmost and bottom material of the FGB. Figure 5 shows the depthwise axial and shear stress distributions, using the presented technique, for an FGB with exponential and power-law gradation through the thickness. By comparing the results to the finite element solution based on first-order shear deformation theory developed by Chakraborty et al. [2003], it is found that for long, slender FGBs, the axial stress distributions were in excellent agreement. But since these two kinds of solutions were based on different theories, the shear stress distributions were obviously different.

The deflection of a cantilever FGB under a unit concentrated force at the tip was also studied using the present method. The results were compared with those available in the literature, as shown in Tables 1 and 2. Table 1 compares the maximum deflection obtained for various L/h to the finite element method (FEM) based on higher-order shear deformation theory (HSDT) [Kadoli et al. 2008]. From Table 1 it is found that the method for FGBs with bigger values of L/h is more valid, while for short beams it is not applicable. Table 2 gives the one-dimensional maximum deflection for different material gradations according to power-law modeling for $n = 0.5$, 1, and 2. Despite some differences between the present
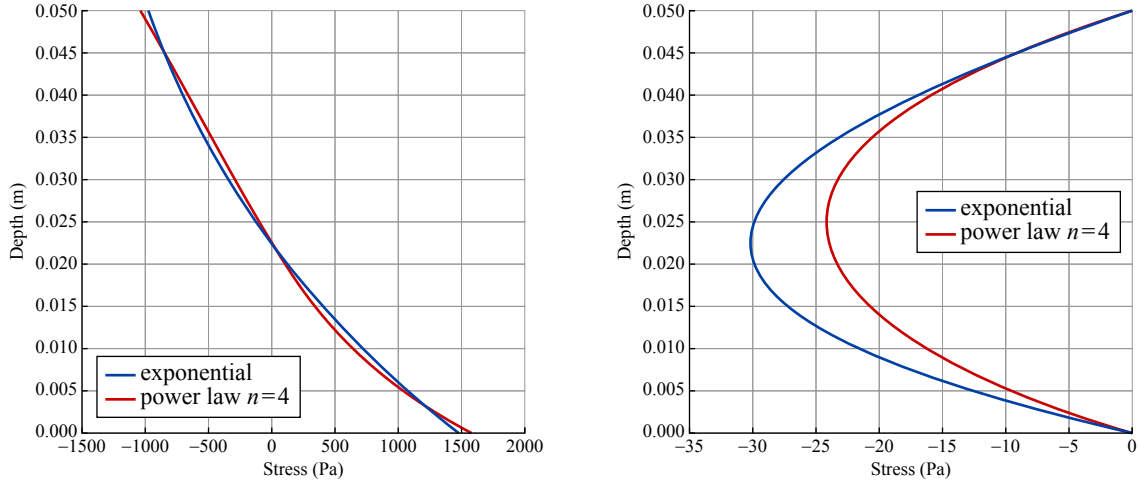
Figure 5. Left: depthwise axial stress distributions for the cantilever FGB subjected to unit transverse load at the tip. Right: depthwise shear stress distributions for the cantilever FGB subjected to unit transverse load at the tip.

method and the FEM [Kadoli et al. 2008], excellent agreement was found with the results from the analytical solution based on the Euler–Bernoulli beam theory discussed in [Yaghoobi and Feridoon 2010].

3.2. *Numerical experiments.* Numerical solutions to determine the deflections of FGBs composed of steel ($E = 210$ GPa) and alumina ($E = 390$ GPa) have been obtained. The distribution of the stresses

L	h	FEM-HSDT	Present Method	% Error
160	12	32.822	32.65	0.52
80	12	4.1567	4.081	1.82
12	12	0.239307	0.01377	94.24

Table 1. Comparison of maximum deflection obtained for various L/h. FEM-HSDT results from [Kadoli et al. 2008].

n	FEM-HSDT	Beam theory	Present method
Ceramic	2.436	2.576	2.576
0.5	2.785	2.960	2.962
1.0	2.942	3.176	3.179
2	3.067	3.323	3.326
Metal	3.605	4	4

Table 2. Nondimensional maximum deflections obtained for different material gradations. FEM-HSDT results from [Kadoli et al. 2008]; beam theory results from [Yaghoobi and Feridoon 2010].
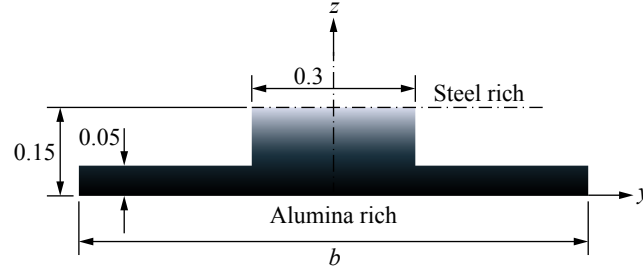
Figure 6. Cross-section of the FGB and quality of material gradation along the thickness.

when the Young's modulus of the beam varies according to the power-law or exponential law through the thickness or width has also been obtained.

3.2.1. *Depthwise varying FGB under a unit transverse distributed load.* Using the present technique, a static analysis of an alumina-steel FGB with length of $L = 5$ m under a unit transverse distributed load will now be carried out. Both exponential and power-law ($n = 1, 2, 3$) gradations of the material along the thickness will be studied. The geometry of the cross-section and the quality of the material gradation are shown in Figure 6.

The longitudinal deflection distributions for the cantilever and simply supported FGBs are shown in Figure 7. As may be seen, an increasing value of n results in an increased value of the deflection. This is due to the fact that a combination of a beam with a bigger value of n is closer to a combination of a homogeneous steel beam.

Figure 8 shows the depthwise axial stress distributions for a cantilever FGB at the fixed end. As may be seen, the variation of the material affects the neutral axis position, changing it from a centroid axis at
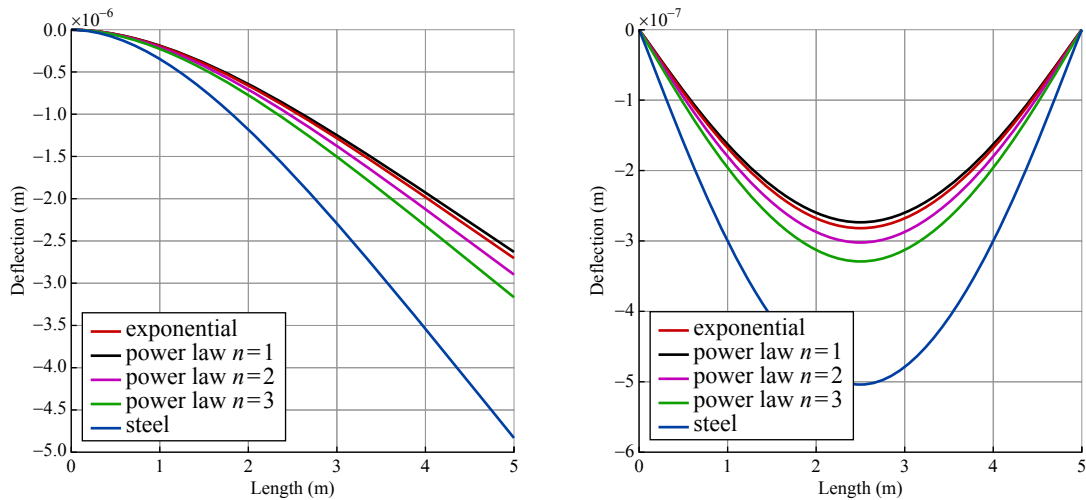
Figure 7. Left: deflection distributions of the cantilever FGB along the length axis. Right: deflection distributions of the simply supported FGB along the length axis.
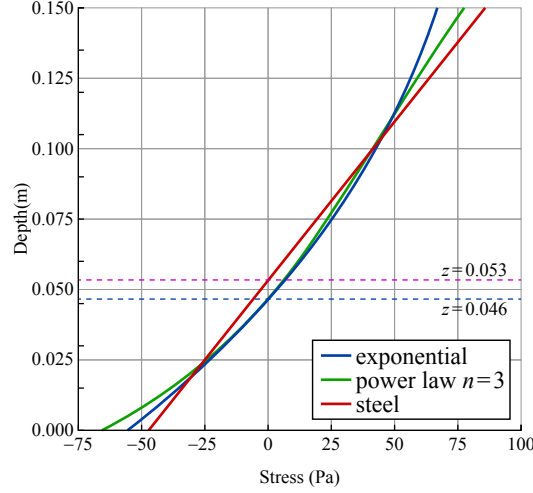
Figure 8. Depthwise axial stress distributions of the cantilever FG beam at the fixed end.

$z = 0.0531$ for the homogenous steel beam to $z = 0.0464$ and $z = 0.0468$ for exponential and power-law ($n = 3$) variations.

3.2.2. *Widthwise varying FGB under unit transverse distributed loads.* The distributions of the axial stresses and deflections are also obtained for an FGB with widthwise material variation, subjected to a unit transverse distributed load. The beam has length of $L = 5$ m, width of $b = 0.1$ m, and height of $h = 0.05$ m. Two kinds of variations of materials according to a power-law modeling for $n = 2$ are considered. Schematic views of the widthwise material gradation are shown in Figure 9. The widthwise distributions of Young's modulus for ceramic-metal-ceramic (CMC) and metal-ceramic-metal (MCM) gradations are also shown in Figures 10 and 11.

For the discretized FGBs with material gradation along the width, the axial force and bending moment resultants can be written as

$$N = \sum_{i=1}^{m} \int_{\frac{-h}{2}}^{\frac{h}{2}} \sigma_i \, dA, \tag{29}$$

$$M = \sum_{i=1}^{m} \int_{\frac{-h}{2}}^{\frac{h}{2}} z\sigma_i \, dA. \tag{30}$$
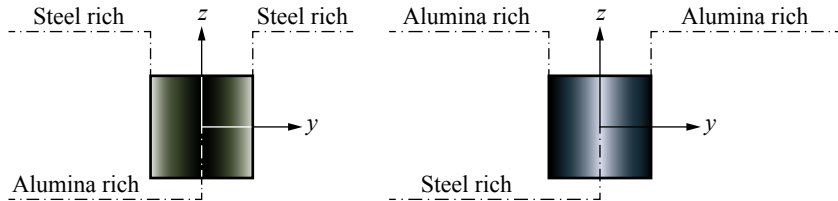
Figure 9. Schematic views for two kind of widthwise gradation of material.
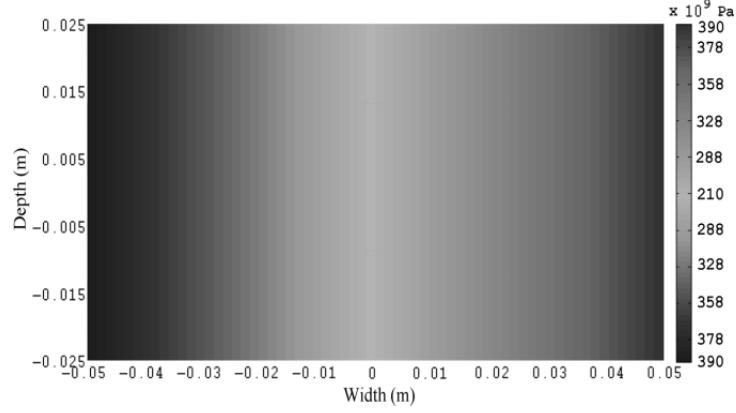
Figure 10. Widthwise Young's modulus distribution for ceramic-metal-ceramic gradation.

Therefore, the definitions (31)–(32) take the forms

$$\tilde{I} = \sum_{i=1}^{m} \int_{\frac{-h}{2}}^{\frac{h}{2}} z^2 E_i b_i \, dz, \tag{31}$$

$$\tilde{A} = \sum_{i=1}^{m} \int_{\frac{-h}{2}}^{\frac{h}{2}} E_i b_i \, dz, \tag{32}$$

$$\tilde{Q} = \sum_{i=1}^{m} \int_{\frac{-h}{2}}^{\frac{h}{2}} z E_i b_i \, dz. \tag{33}$$

Using definitions (31)–(33) and equations (20), (21) and (5) the distribution of axial stress at the cross-section of the FGB can be obtained as

$$\sigma_x(x, y, z) = E(y)(\epsilon_{x_0} + z\kappa) = \frac{M(x)(z\tilde{A} - \tilde{Q})}{-\tilde{Q}^2 + \tilde{A}\tilde{I}} E(y). \tag{34}$$
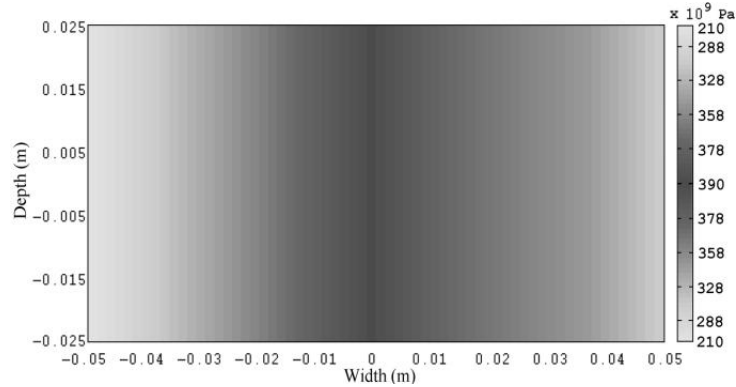
Figure 11. Widthwise Young's modulus distribution for metal-ceramic-metal gradation.
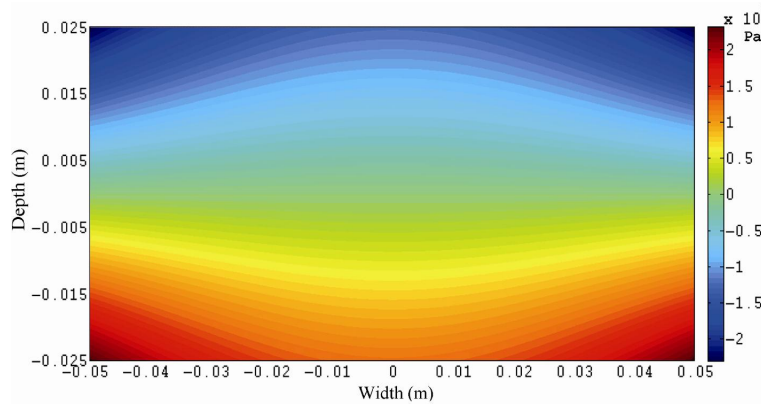
Figure 12. Depthwise axial stress distribution for the FGB with ceramic-metal-ceramic gradation.

The depthwise axial stress distribution at the fixed end of the cantilever FGB for the CMC and MCM gradations are shown in Figures 12 and 13. The figures reveal that the maximum stress occurs at the regions with the biggest values of Young's modulus and the maximum distance from the neutral axis.

Figures 14 and 15 show the distributions of the longitudinal deflection for a cantilever and a simply supported FGB with CMC and MCM gradations. From the figures it can be observed that the deflections for the MCM are more than those for the CMC. This is due to the fact that Young's modulus of alumina is higher than that of steel. Consequently, the bending rigidity of the beam with the CMC gradation is higher than that of MCM.

4. Conclusions

Stress and deflection analyses of functionally graded beams with complex cross-section and different material variations, subjected to transverse loads, were carried out using a simplified technique. The accuracy of the technique was evaluated. Numerical investigations were then performed. From the results it can be concluded that:
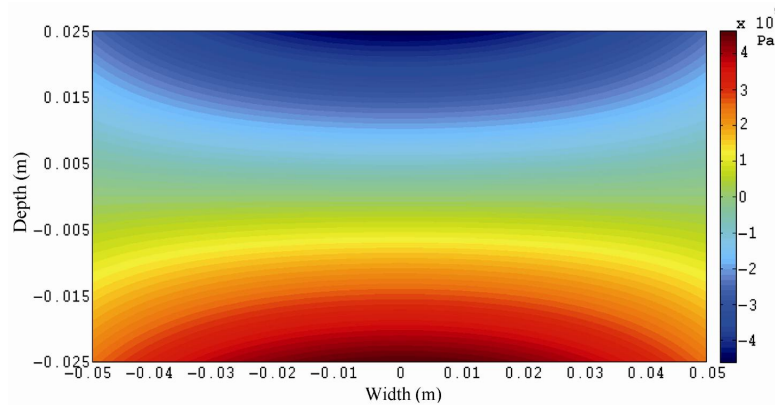
Figure 13. Depthwise axial stress distribution for the FGB with metal-ceramic-metal gradation.
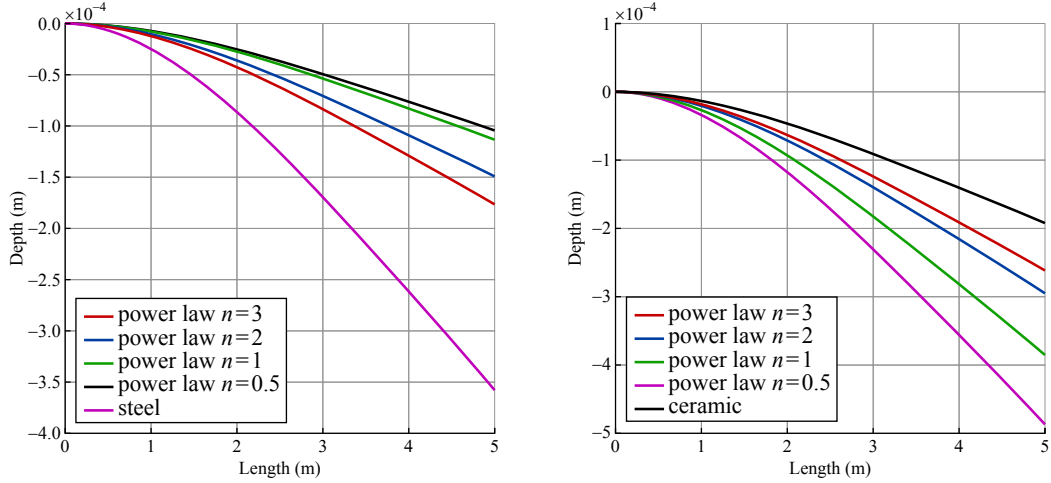
Figure 14. Longitudinal deflection distributions for a cantilever FGB. Left: ceramic-metal-ceramic gradation. Right: metal-ceramic-metal gradation.

(1) Quality of material gradation affects the deflection, stresses and neutral axis position significantly.

(2) The maximum axial stress occurs at the regions with the biggest values of Young's modulus and the maximum distance from the neutral axis (for ceramic-metal-ceramic gradation at vertices, and for metal-ceramic-metal at midpoints of top and bottom edges).

(3) The bending rigidity of FGBs with the ceramic-metal-ceramic gradation is higher than metal-ceramic-metal.

(4) The technique is useful for the static analysis of long, slender FGBs with complex cross-sections and various material gradations.
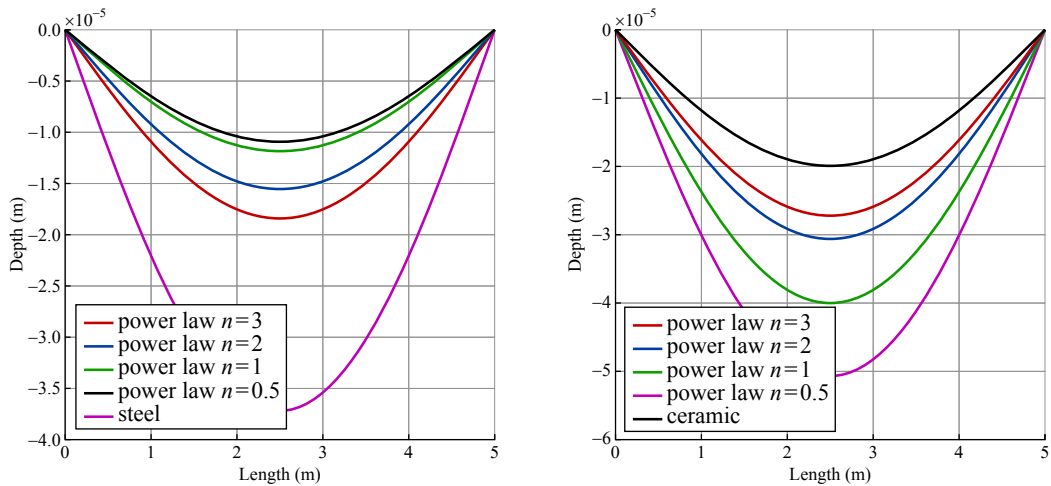
Figure 15. Longitudinal deflection distributions for a simply supported FGB. Left: ceramic-metal-ceramic gradation. Right: metal-ceramic-metal gradation.

5. Acknowledgements

References

[Apetre et al. 2008] N. A. Apetre, B. V. Sankar, and D. R. Ambur, "Analytical modeling of sandwich beams with functionally graded core", *J. Sandw. Struct. Mater.* **10**:1 (2008), 53–74.

[Aydogdu and Taskin 2007] M. Aydogdu and V. Taskin, "Free vibration analysis of functionally graded beams with simply supported edges", *Mater. Des.* **28**:5 (2007), 1651–1656.

[Bîrsan et al. 2012] M. Bîrsan, H. Altenbach, T. Sadowski, V. A. Eremeyev, and D. Pietras, "Deformation analysis of functionally graded beams by the direct approach", *Compos. B Eng.* **43**:3 (2012), 1315–1328.

[Chakraborty et al. 2003] A. Chakraborty, S. Gopalakrishnan, and J. N. Reddy, "A new beam finite element for the analysis of functionally graded materials", *Int. J. Mech. Sci.* **45**:3 (2003), 519–539.

[Ching and Yen 2005] H. K. Ching and S. C. Yen, "Meshless local Petrov–Galerkin analysis for 2D functionally graded elastic solids under mechanical and thermal loads", *Compos. B Eng.* **36**:3 (2005), 223–240.

[Ching and Yen 2006] H. K. Ching and S. C. Yen, "Transient thermoelastic deformations of 2-D functionally graded beams under nonuniformly convective heat supply", *Compos. Struct.* **73**:4 (2006), 381–393.

[Şimşek and Kocatürk 2009] M. Şimşek and T. Kocatürk, "Free and forced vibration of a functionally graded beam subjected to a concentrated moving harmonic load", *Compos. Struct.* **90**:4 (2009), 465–473.

[Ding et al. 2007] H. J. Ding, D. J. Huang, and W. Q. Chen, "Elasticity solutions for plane anisotropic functionally graded beams", *Int. J. Solids Struct.* **44**:1 (2007), 176–196.

[Farhatnia et al. 2009] F. Farhatnia, G.-A. Sharifi, and S. Rasouli, "Numerical and analytical approach of thermo-mechanical stresses in FGM beams", pp. 1707–1712 in *Proceedings of the World Congress on Engineering, II* (London, 2009), edited by S. I. Ao et al., Newswood Limited, Hong Kong, 2009.

[Hamed 2012] E. Hamed, "Bending and creep buckling response of viscoelastic functionally graded beam-columns", *Compos. Struct.* **94**:10 (2012), 3043–3051.

[Kadoli et al. 2008] R. Kadoli, K. Akhtar, and N. Ganesan, "Static analysis of functionally graded beams using higher order shear deformation theory", *Appl. Math. Model.* **32**:12 (2008), 2509–2525.

[Kang and Li 2009] Y.-A. Kang and X.-F. Li, "Bending of functionally graded cantilever beam with power-law non-linearity subjected to an end force", *Int. J. Non-Linear Mech.* **44**:6 (2009), 696–703.

[Kapuria et al. 2008] S. Kapuria, M. Bhattacharyya, and A. N. Kumar, "Bending and free vibration response of layered functionally graded beams: A theoretical model and its experimental validation", *Compos. Struct.* **82**:3 (2008), 390–402.

[Ke et al. 2009] L.-L. Ke, J. Yang, S. Kitipornchai, and Y. Xiang, "Flexural vibration and elastic buckling of a cracked Timoshenko beam made of functionally graded materials", *Mech. Adv. Mater. Struct.* **16**:6 (2009), 488–502.

[Li 2008] X.-F. Li, "A unified approach for analyzing static and dynamic behaviors of functionally graded Timoshenko and Euler–Bernoulli beams", *J. Sound Vib.* **318**:4–5 (2008), 1210–1229.

[Lü et al. 2006] C. Lü, W. Chen, and Z. Zhong, "Two-dimensional thermoelasticity solution for functionally graded thick beams", *Sci. China Ser. G* **49**:4 (2006), 451–460.

[Mahi et al. 2010] A. Mahi, E. A. A. Bedia, A. Tounsi, and I. Mechab, "An analytical method for temperature-dependent free vibration analysis of functionally graded beams with general boundary conditions", *Compos. Struct.* **92**:8 (2010), 1877–1887.

[Menaa et al. 2012] R. Menaa, A. Tounsi, F. Mouaici, I. Mechab, M. Zidi, and E. A. A. Bedia, "Analytical solutions for static shear correction factor of functionally graded rectangular beams", *Mech. Adv. Mater. Struct.* **19**:8 (2012), 641–652.

[Miyamoto et al. 1999] Y. Miyamoto, W. A. Kaysser, B. H. Rabin, A. Kawasaki, and R. G. Ford (editors), *Functionally graded materials: Design, processing and applications*, Materials Technology Series **5**, Kluwer, Boston, 1999.

[Piovan et al. 2012] M. T. Piovan, S. Domini, and J. M. Ramirez, "In-plane and out-of-plane dynamics and buckling of functionally graded circular curved beams", *Compos. Struct.* **94**:11 (2012), 3194–3206.

[Rahimi and Davoudinik 2010] G. H. Rahimi and A. R. Davoudinik, "Large deflection of functionally graded cantilever flexible beam with geometric non-linearity: Analytical and numerical approaches", *Sci. Iran. Trans. B* **17**:1 (2010), 25–40.

[Sankar 2001] B. V. Sankar, "An elasticity solution for functionally graded beams", *Compos. Sci. Technol.* **61**:5 (2001), 689–696.

[Sankar and Tzeng 2002] B. V. Sankar and J. T. Tzeng, "Thermal stresses in functionally graded beams", *AIAA J.* **40**:6 (2002), 1228–1232.

[Shahba and Rajasekaran 2012] A. Shahba and S. Rajasekaran, "Free vibration and stability of tapered Euler–Bernoulli beams made of axially functionally graded materials", *Appl. Math. Model.* **36**:7 (2012), 3094–3111.

[Shahba et al. 2013] A. Shahba, R. Attarnejad, and S. Hajilar, "A mechanical-based solution for axially functionally graded tapered Euler–Bernoulli beams", *Mech. Adv. Mater. Struct.* **20**:8 (2013), 696–707.

[Sharifishourabi et al. 2012] G. Sharifishourabi, R. Alebrahim, S. S. Teshnizi, and F. N. Ani, "Effects of material gradation on thermo-mechanical stresses in functionally graded beams", *APCBEE Procedia* **3** (2012), 194–199.

[Sharifishourabi et al. 2014a] G. Sharifishourabi, R. Alebrahim, S. Sharifi, A. Ayob, Z. Vrcelj, and M. Y. Yahya, "Mechanical properties of potentially-smart carbon/epoxy composites with asymmetrically embedded shape memory wires", *Mater. Des.* **59** (2014), 486–493.

[Sharifishourabi et al. 2014b] G. Sharifishourabi, S. Sharifi, A. Ayob, and M. Y. Yahya, "Tensile test machine for unsymmetrical materials", *Exp. Mech.* **54**:4 (2014), 689–694.

[Shooshtari and Rafiee 2011] A. Shooshtari and M. Rafiee, "Nonlinear forced vibration analysis of clamped functionally graded beams", *Acta Mech.* **221**:1-2 (2011), 23–38.

[Sina et al. 2009] S. A. Sina, H. M. Navazi, and H. Haddadpour, "An analytical method for free vibration analysis of functionally graded beams", *Mater. Des.* **30**:3 (2009), 741–747.

[Suresh and Mortensen 1998] S. Suresh and A. Mortensen, *Fundamentals of functionally graded materials: Processing and thermomechanical behaviour of graded metals and metal-ceramic composites*, Institute of Materials, London, 1998.

[Thai and Vo 2012] H.-T. Thai and T. P. Vo, "Bending and free vibration of functionally graded beams using various higher-order shear deformation beam theories", *Int. J. Mech. Sci.* **62**:1 (2012), 57–66.

[Venkataraman and Sankar 2003] S. Venkataraman and B. V. Sankar, "Elasticity solution for stresses in a sandwich beam with functionally graded core", *AIAA J.* **41**:12 (2003), 2501–2505.

[Wakashima et al. 1990] K. Wakashima, T. Hirano, and M. Niino, "Functionally gradient materials (FGM) architecture: A new type of ceramic/metal assemblage designed for hot structural components", pp. 97–102 in *Space applications of advanced structural materials* (Noordwijk, NL, 1990), ESA SP **303**, European Space Agency, Paris, 1990.

[Wattanasakulpong et al. 2012] N. Wattanasakulpong, B. G. Prusty, D. W. Kelly, and M. Hoffman, "Free vibration analysis of layered functionally graded beams with experimental validation", *Mater. Des.* **36** (2012), 182–190.

[Yaghoobi and Feridoon 2010] H. Yaghoobi and A. Feridoon, "Influence of neutral surface position on deflection of functionally graded beam under uniformly distributed load", *World Appl. Sci. J.* **3** (2010), 337–341.

[Ying et al. 2008] J. Ying, C. F. Lü, and W. Q. Chen, "Two-dimensional elasticity solutions for functionally graded beams resting on elastic foundations", *Compos. Struct.* **84**:3 (2008), 209–219.

[Yousefi and Rastgoo 2011] A. Yousefi and A. Rastgoo, "Free vibration of functionally graded spatial curved beams", *Compos. Struct.* **93**:11 (2011), 3048–3056.

[Zhong and Yu 2007] Z. Zhong and T. Yu, "Analytical solution of a cantilever functionally graded beam", *Compos. Sci. Technol.* **67**:3–4 (2007), 481–488.

GHOLAMALI SHARIFISHOURABI: `sharifi186@gmail.com`
Centre for Composites, Universiti Teknologi Malaysia, Skudai, 81310 Johor, Malaysia

AMRAN AYOB: `amran@fkm.utm.my`
Centre for Composites, Universiti Teknologi Malaysia, Skudai, 81310 Johor, Malaysia

SCOTT GOHERY: `scott.gohery@unimelb.edu.au`
College of Engineering and Science, Victoria University, Melbourne, VIC 8001, Australia

MOHD YAZID BIN YAHYA: `yazid@fkm.utm.my`
Centre for Composites, Universiti Teknologi Malaysia, Skudai, 81310 Johor, Malaysia

SHOKROLLAH SHARIFI: `sharifi.te@gmail.com`
Centre for Composites, Universiti Teknologi Malaysia, Skudai, 81310 Johor Bahru, Malaysia

ZORA VRCELJ: `zora.vrcelj@vu.edu.au`
College of Engineering and Science, Victoria University, Melbourne, VIC 8001, Australia

msp

RESPONSE OF SUBMERGED METALLIC SANDWICH STRUCTURES TO UNDERWATER IMPULSIVE LOADS

Siddharth Avachat and Min Zhou

The response of planar sandwich structures with metallic square-honeycomb cores under high-intensity water-based impulsive loading is analyzed through fully dynamic finite element simulations. The analyses concern overall structural response, damage and energy dissipation. The steel sandwich plates considered have different contact conditions with water — an air-backed configuration which simulates contact with water on only the load side and a water-backed configuration which simulates submerged conditions. The 3D finite element simulations account for the effects of fluid-structure interactions and the ductile failure of the sandwich structure material. Results show that the primary deformation mode is core-wall buckling in light-core structures and shear-rupture in face-sheets and core-webs in heavy-core structures. On a unit weight basis, sandwich structures with heavy cores perform poorly while those with light cores exhibit superior blast-resistance in terms of back-face deflection and total energy absorbed. Significant differences between the responses of air-backed and water-backed structures are observed. An analysis is carried out to develop structure-loading-performance relations to facilitate the design of structures tailored for specific loading conditions.

1. Introduction

Marine structures are designed to operate in hostile environments consisting of corrosive seawater, hot and cold temperature extremes, transient dynamic loads from hull-slamming and complex three-dimensional hydrostatic loads. Additionally, naval structures are required to withstand impact and blast loads resulting from surface and underwater explosions. The dynamic response of structures under such conditions is complicated because of many factors, including rate effects, complex failure modes, the superposition of dynamic and static pressures, load triaxiality and varying impulsive load intensities.

In recent years, sandwich structures have become a central structural component of many naval vessels which require blast protection. This emerging trend necessitates research that accounts for constituent material behavior, structural hierarchy, topological characteristics and complex loading involving fluid-structure interactions (FSI). Experiments focusing on different core topologies and specimen sizes have been carried out by Espinosa et al. [2006] and McShane et al. [2008] using gas gun-based impact loading to generate underwater pressure impulses, and by Dharmasena et al. [2008] using explosive sheets to generate planar pressure impulses. Constitutive relations have been developed for sandwich structures, accounting for the crush behavior of cores and plasticity in constituents [Deshpande and Fleck 2005; Xue and Hutchinson 2004b]. It has been demonstrated that finite element analyses are capable of accurately quantifying the dynamic response of metallic sandwich structures and tracking deformation mechanisms

---

such as face-stretching, core-buckling and rupture [Côté et al. 2009; Dharmasena et al. 2010; Hutchinson and Xue 2005; Liang et al. 2005; Radford et al. 2006; McShane et al. 2006; Rathbun et al. 2006; Spuskanyuk and McMeeking 2007; Vaziri and Xue 2007; Vaziri et al. 2007; Wadley et al. 2013; Wei et al. 2008; Xue and Hutchinson 2004a; Zok et al. 2005]. The major findings from these studies include:

(1) Metallic sandwich structures outperform monolithic plates when deformation is dominated by bending. In the stretching regime, monolithic plates show higher plastic dissipation than sandwich plates.

(2) The overall deflection experienced by sandwich plates is significantly less than that experienced by monolithic plates of equivalent mass. The forces and impulses transmitted by sandwich structures are also lower than those by monolithic structures.

(3) Core design greatly influences the dynamic response of sandwich structures. The dynamic strength of the core is an important factor in overall structural response. Stiff cores perform poorly while light cores lead to more efficient blast mitigation.

(4) Homogenized continuum core models cannot accurately capture the various damage modes associated with prismatic sandwich structures. Rupture and core buckling can only be evaluated using detailed finite element simulations with explicit account of structures.

(5) FSI effects need to be considered to accurately characterize impulsive loads and can be exploited to improve blast mitigation in marine structures. Sandwich structures subjected to exponentially decaying pressure pulses outperform those subjected to instantaneous loads.

While these findings provide significant insight, the relationship between performance in terms of failure resistance and energy dissipation and design parameters of sandwich structures has not been well quantified. Structural design of ships and submersibles is a complex undertaking, because the deformations experienced by naval vessels are a result of the combined effects of multiple loads acting simultaneously. Geometric and material nonlinearities create complicated loading conditions and often cause unpredictable failure through buckling and shear cracking. The effective design of naval structures requires an understanding of the failure characteristics of advanced materials and structures, and the capability to predict and determine their performance characteristics.

The objective of this analysis is to identify deformation mechanisms leading to ultimate failure and develop quantitative material-property-performance relations to aid the development of blast-resistant metallic sandwich structures. Simulations are carried out for a range of impulsive load intensities and two distinct loading configurations: (1) an air-backed configuration, with the structure in contact with water on the impulse side, and (2) a water-backed configuration, with the structure in contact with water on the impulse side as well as the backside. The structure-performance relations presented here focus on optimal core, front-face and back-face masses as fractions of total structural mass. The analysis yields the optimal values of these attributes, which in turn determine the core mass fraction $\overline{M}_{\mathrm{C}}$, the front face mass fraction $\overline{M}_{\mathrm{FF}}$, and back face mass fraction $\overline{M}_{\mathrm{BF}}$. The results are presented in normalized forms to gain insight into underlying trends that can be used to design more blast-resistant structures. The constitutive and damage behavior of steel is characterized by the Johnson–Cook model [1985], and the dynamic response of water is characterized by the Mie–Grüneisen equation of state. The insight gained here provides guidelines for the design of structures for which response to water-based impulsive loading is an important consideration. In order to facilitate comparison of dynamic response, all structures are
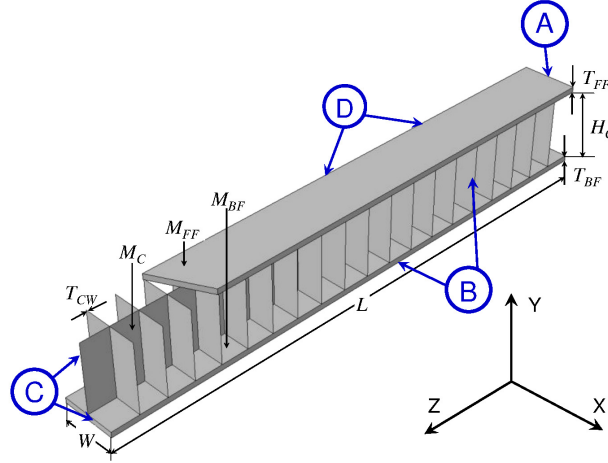
Figure 1. Schematic illustration of a sandwich beam with square honeycomb core.

designed to have the same total areal mass of $\sim 100\,\mathrm{kg/m^2}$. This necessitates a balance in core, front face and back face masses to maintain a constant areal mass. The structures are subjected to five loading intensities, each simulating different standoff distances of an underwater explosive source from the ship hull. The design space consists of three major aspects: (1) performance parameters (deflection, energy dissipation and impulse transmission), (2) structural attributes (core mass, front-face mass and back-face mass), and (3) loading intensity. These parameters and their effects are intimately interrelated. The structural composition of the sandwich structure is systematically varied over a wide range of structural attributes with simultaneous variations in loading rates to delineate the effects of each parameter on dynamic performance and blast resistance. This approach enables the contributions of different deformation mechanisms (front-face stretching and rupture, core-wall buckling, core crushing and back-face stretching) to be tracked and quantified. Additionally, this approach captures the interaction and coupling of the different design parameters at the structural level. The analyses also focus on the correlation between mass fractions of each structural component (front face, core and back face), deflection, energy dissipation and impulse transmission. The results of parametric studies are presented in a format wherein the response variables are functions of the loading (impulse magnitude) and structural attributes (mass fractions of each structural component).

2. Framework of analysis

2.1. *Structure specifications*. The square honeycomb sandwich plates considered are made of AISI 304 steel. Figure 1 shows the sandwich structure consisting of a core with periodic square-honeycomb unit-cells and face sheets. The core-height H_C is 100 mm and the length L of the beam is 1000 mm. The core-height to beam-length ratio H_C/L is 0.1. For the sandwich structure, face A is fixed (zero displacement and rotations in all directions), faces B and D have boundary conditions that forbid displacement in the x-direction, and face C has symmetry boundary conditions with the plane of symmetry normal to the z-direction. The boundary conditions and specified dimensions are sufficient to ensure beam bending
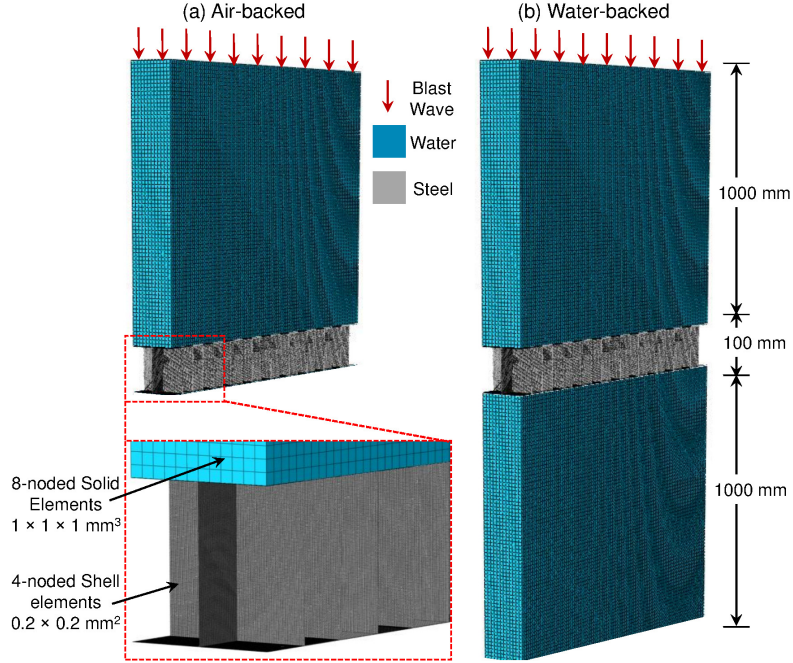
Figure 2. Sandwich structures with edge-supported boundaries and air-backed and water-backed loading configurations.

behavior [Wicks and Hutchinson 2001; Zok et al. 2003]. Figure 2 shows the air-backed and water-backed loading configurations with the direction of impulsive loading. The width W of the sandwich beam is 100 mm. The areal mass of the sandwich structure is calculated as

$$M_{\text{Total}} = M_{\text{FF}} + M_{\text{BF}} + M_{\text{C}} = \frac{\rho}{A}(T_{\text{FF}} \cdot A \cdot W + T_{\text{BF}} \cdot A \cdot W + N_{\text{CW}} \cdot T_{\text{CW}} \cdot H_{\text{C}} \cdot L), \tag{1}$$

where M_{FF} is the areal mass of the front face, M_{BF} is the areal mass of the back face, M_{C} is the areal mass of the core, ρ_{Steel} is the density of steel, N_{CW} is the number of unit cells in the square honeycomb, H_{C} is the height of the core, T_{CW} is the core wall thickness, A is the area under loading, W is the width of the structure, and L is the length of the structure. The total areal mass of the plate, M_{Total}, is kept constant at $100 \, \text{kg/m}^2$. The normalized core mass is

$$\overline{M}_{\text{C}} = \frac{M_{\text{C}}}{M_{\text{Total}}}, \tag{2}$$

the normalized front face mass is

$$\overline{M}_{\text{FF}} = \frac{M_{\text{FF}}}{M_{\text{Total}}}, \tag{3}$$

and the normalized back face mass is

$$\overline{M}_{\text{BF}} = \frac{M_{\text{BF}}}{M_{\text{Total}}}. \tag{4}$$

Specimen number	Front face thickness T_{FF} (mm)	Front face mass M_{FF} (kg/m^2)	Core wall thickness T_{CW} (mm)	Core areal mass M_C (kg/m^2)	Back face thickness T_{BF} (mm)	Back face mass M_{BF} (kg/m^2)	Areal mass M_{Total} (kg/m^2)
1	1.0	8	3.62	84	1.0	8	100
2	2.0	16	2.93	68	2.0	16	100
3	3.0	24	2.24	52	3.0	24	100
4	4.0	32	1.55	36	4.0	32	100
5	5.0	40	0.86	20	5.0	40	100
6	5.6	45	0.43	10	5.6	45	100

Table 1. Structural configurations analyzed for the optimization of core mass.

Specimen number	Front face thickness T_{FF} (mm)	Front face mass M_{FF} (kg/m^2)	Core wall thickness T_{CW} (mm)	Core areal mass M_C (kg/m^2)	Back face thickness T_{BF} (mm)	Back face mass M_{BF} (kg/m^2)	Areal mass M_{Total} (kg/m^2)
1	0.5	4	0.86	20	9.5	76	100
2	1.0	8	0.86	20	9.0	72	100
3	2.0	16	0.86	20	8.0	64	100
4	3.0	24	0.86	20	7.0	56	100
5	4.0	32	0.86	20	6.0	48	100
6	5.0	40	0.86	20	5.0	40	100

Table 2. Structural configurations analyzed for the optimization of face mass.

To evaluate the role of core strength in the deformation, $\overline{M}_C$ is varied from 0.10 to 0.84 by changing the core wall thicknesses. To keep the total mass constant, the changes in core mass are compensated by variations in the masses of the face sheets. Table 1 shows the structural parameters used in the core mass optimization. Structures with $0.10 < \overline{M}_C < 0.5$ are called *light core* structures, while those with $0.5 < \overline{M}_C < 1$ are called *heavy core* structures. For the optimized core mass fraction, the front and back face thicknesses are varied to evaluate the role of face strength in dynamic deformation. For this, the normalized front face mass $\overline{M}_{FF}$ is varied from 0.04 to 0.4 and the corresponding normalized back face mass $\overline{M}_{BF}$ is varied from 0.86 to 0.50. Table 2 shows the structural parameters used for the optimization of front and back face masses. These structures are subjected to a range of impulsive loads in both air-backed and water-backed conditions.

2.2. *Impulsive loading.* A number of approaches have been used to simulate the interactions of blast waves with structures, both in air and underwater. One approach is to simulate the fluid with Eulerian meshes and the solid structure with Lagrangian meshes. The behavior of the fluid in the Eulerian domain can be modeled using an equation of state. This technique is termed the "arbitrary Lagrangian–Eulerian" method and is often used to simulate the fluid structure interactions when large mesh distortions in the

fluid domain are a major concern [Battley and Allen 2012; Latourte et al. 2012]. The second approach is to prescribe an exponentially decaying pressure on one face of the structure [Dharmasena et al. 2011; Wadley et al. 2013] to account for the effect of the fluid. The incident impulse can be calculated using [ConWep 2005], a blast simulation code developed by the U.S. Army Corps of Engineers, which allows the impulse to be determined for given explosive charge and standoff distance between the charge and the target. A third approach is to simulate both the fluid and the structure with Lagrangian elements [Mori et al. 2007]. An appropriate equation of state is chosen to describe the response of the fluid. In this study, the third approach with a Lagrangian formulation for both the fluid and the structure is employed.

According to Taylor's analysis [1963] of one-dimensional blast waves for a plane wave impinging on a free-standing plate, the pressure in the fluid at a fixed position follows the relation

$$p(t) = p_0 \exp(-t/t_0), \tag{5}$$

where p_0 is the peak pressure, t is time and t_0 is the reference decay time. The area under this curve is the impulse I imparted by the wave:

$$I = \int_0^{t_0} p(t) \, dt. \tag{6}$$

A nondimensionalized impulse $\bar{I}$ can be expressed as

$$\bar{I} = \frac{I}{\rho_w c_w \sqrt{A}}, \tag{7}$$

where ρ_w is the density of water, c_w is the speed of sound in water and A is the area of loading. Impulsive waves due to underwater blasts have a characteristic decay time on the order of $\sim 10^{-4}$ seconds [Cole 1947; Kambouchev et al. 2007; Taylor 1963]. The numerical modeling simulates the effects of different standoff distances of an explosive source. For an underwater explosion, the peak pressure (in MPa) scales as

$$p_0 = 52.4 \left(\frac{M^{1/3}}{r} \right)^{1.13}, \tag{8}$$

where M is the mass of trinitrotoluene (TNT) in kilograms and r is the standoff distance in meters [Cole 1947; Kambouchev et al. 2007; Taylor 1963].

Figure 3 shows the pressure histories of impulsive loads considered in the finite element simulations. The reference decay time (t_0) is $\sim 250 \, \mu s$. The rise time of the pressure pulses is on the order of $25 \, \mu s$ and the time for the pressure to decrease to negligible levels is on the order of $800 \, \mu s$. The impulsive loads considered in this set of calculations have peak pressures of 450, 350, 250, 150 and 50 MPa, which approximately correspond to 100 kg of TNT exploding at distances of 0.7, 0.9, 1.15, 1.8 and 4.8 meters, respectively. The impulsive load is planar, the sandwich structure is in the form of a beam and a single repeating unit cell along the x-direction (shown in Figure 2) is analyzed.

A number of load conditions and service environments exist for sandwich structures in large naval structures, such as ships or submarines. For example, ship hulls and superstructures are in touch with water on the outer side (impulse side) and air or machinery on the inner side. On the other hand, keels, rudders, propeller blades and underwater pipelines consist of water on both the impulse side and the protected side. For the purpose of the current study, the former is called the air-backed configuration (Figure 2(a)) and the latter is called the water-backed configuration (Figure 2(b)). In both air-backed
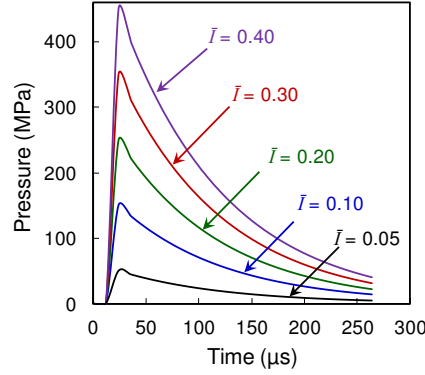
Figure 3. Pressure histories of incident impulsive waves incident on sandwich structures.

and water-backed configurations, the length of the impulse-side water column is 1000 mm. In the water-backed configuration, the length of the back-side water column is also 1000 mm. The length is sufficient to ensure that reflected waves do not interfere with deformations in the structure prior to 1000 μs.

3. Numerical calculations

The faces and core webs are meshed with 4-noded shell elements for finite strains to capture buckling and rupture. In the initial steps, nodes are adjusted with strain-free displacements to remove any surface interpenetration. A penalty contact algorithm is used at all interfaces to strongly discourage interpenetration by applying penalty forces. Specifically, an interface "spring" is inserted between the slave and master nodes and penalty forces at each instance of interpenetration are calculated by multiplying the spring stiffness with the penetration distance. The penalty contact framework seeks to resolve contact penetrations that exist at the beginning of each time increment. This ensures that surface interpenetrations are negligible and do not affect the deformation mechanisms in the different components of the sandwich structure. The response of the structures is partly quantified using the deflection at the center of the back face and the energy dissipated through plastic deformation and damage due to crack initiation and growth. These quantities depend on structural parameters, loading configuration and impulse magnitude. Damage in the forms of core crushing, core-web cracking and face-sheet rupture is tracked. The calculations are conducted using the ABAQUS/Explicit finite-element package [Hibbit et al. 2009].

3.1. *Constitutive and damage models for steel.* The sandwich plates studied here are made of AISI 304 steel, which has high yield strength, high strain hardening and high ductility. The Johnson–Cook model [Johnson and Cook 1985], which accounts for strain-hardening, thermal softening, and strain rate dependence is used to describe the material's response. Specifically,

$$\bar{\sigma}(\bar{\epsilon}^{\text{pl}}, \dot{\epsilon}^{\text{pl}}, \theta) = (A + B(\bar{\epsilon}^{\text{pl}})^n)\left(1 + C \ln \frac{\dot{\epsilon}^{\text{pl}}}{\dot{\epsilon}_0}\right)(1 - (\hat{\theta})^m), \tag{9}$$

where $\bar{\sigma}$ is the Mises equivalent stress, $\bar{\epsilon}^{\text{pl}}$ is the equivalent plastic strain, $\dot{\epsilon}^{\text{pl}}$ is the equivalent plastic strain rate, and A, B, C, m and n are material parameters measured at or below the transition temperature

$\theta_{\text{transition}}$, $\dot{\epsilon}_0$ is a reference strain rate, and $\hat{\theta}$ is the nondimensional temperature, defined as

$$\hat{\theta} \equiv \begin{cases} 0 & \text{for } \theta < \theta_{\text{transition}}, \\ (\theta - \theta_{\text{transition}})/(\theta_{\text{melt}} - \theta_{\text{transition}}) & \text{for } \theta_{\text{transition}} \leq \theta \leq \theta_{\text{melt}}, \\ 1 & \text{for } \theta > \theta_{\text{melt}}. \end{cases} \tag{10}$$

In these expressions, θ is the current temperature, θ_{melt} is the melting temperature and $\theta_{\text{transition}}$ is the transition temperature below which the yield stress is independent of the temperature. When the temperature exceeds the melting temperature, the material behaves like a fluid and has no shear resistance. The use of the Johnson–Cook constitutive model partly reflects the nature of the deformations analyzed and partly reflects the fact that extensive experimental data is available and has been used to calibrate this model for the conditions analyzed. Indeed, there are more "sophisticated" models than the Johnson–Cook model. These models use different parameters or internal state variables to deal with issues such as complicated loading paths, varying stress triaxiality, and deformation mechanisms. However, the key aspects of the loading conditions analyzed in this paper are dynamic, rate-dependent, monotonic (no unloading considered), and approximately proportional. Under such conditions, the constitutive response of the steels considered here can be well-characterized as dependent on strain, strain rate and temperature. Models using relations between stress and these quantities are effectively similar or equivalent, as long as enough parameters exist to allow a good fit to experimental data. For the conditions stated above, many more sophisticated models using, say, certain internal state variables essentially simplify to relations involving stress, strain, strain rate and temperature as independent variables.

The failure model is based on the value of equivalent plastic strain. The damage parameter ω is defined as

$$\omega = \sum \left(\frac{\Delta \bar{\epsilon}^{\text{pl}}}{\bar{\epsilon}_f^{\text{pl}}} \right), \tag{11}$$

where $\Delta \bar{\epsilon}^{\text{pl}}$ is an increment of the equivalent plastic strain, $\bar{\epsilon}_f^{\text{pl}}$ is the strain at failure, and the summation is performed over all increments up to the current state in the analysis. The strain at failure is assumed to be dependent on strain rate and temperature such that

$$3\bar{\epsilon}_f^{\text{pl}} = \left(D_1 + D_2 \exp(-D_3 p/\bar{\sigma}) \right) \left(1 + D_4 \ln \frac{\dot{\bar{\epsilon}}^{\text{pl}}}{\dot{\epsilon}_0} \right)(1 + D_5 \hat{\theta}), \tag{12}$$

where D_1, D_2, D_3, D_4, and D_5 are experimentally determined damage parameters, $p = -\sigma_{ii}/3$ is the hydrostatic pressure. The values for the parameters are obtained from [Johnson and Cook 1985] and [Nahshon et al. 2007] and are shown in Table 3.

3.2. *Mie–Grüneisen equation of state for water.* The response of water is modeled with the Mie–Grüneisen equation of state of the linear Hugoniot form:

$$p = \frac{\rho_0 c_0^2 \eta}{(1 - s\eta)^2} \left(1 - \frac{\Gamma_0 \eta}{2} \right) + \Gamma_0 \rho_0 E_m, \tag{13}$$

where p is pressure, c_0 is the speed of sound in bulk, ρ_0 is the initial density, η is the volumetric compressive strain, E_m is internal energy per unit mass, Γ_0 is Grüneisen's gamma at reference state,

Density of steel (ρ_{Steel})	7800 kg/m^3	A	310 MPa
Young's modulus (E)	193 GPa	B	1000 MPa
Poisson's ratio (ν)	0.3	n	0.65
Melting temperature (θ_{melt})	1800 °C	C	0.034
Reference temperature (θ)	25 °C	m	1.05
Density of water (ρ_{Water})	1000 kg/m^3	D_1	0.25
Speed of sound in water (c_0)	1500 m/s	D_2	4.38
Grüneisen's gamma for water (Γ_0)	0.1	D_3	2.68
		D_4	0.002
		D_5	0.61

**Table 3.** Parameters for constitutive and damage models.

$s = dU_s/dU_p$ is the linear Hugoniot slope coefficient, U_s is the shock wave velocity and U_p is particle velocity, which is related to U_s through

$$U_s = c_0 + s U_p. \qquad (14)$$

4. Results and discussion

4.1. *Parametric analysis and comparison with experiments.* A parametric study is carried out, focusing on the effects of (i) loading intensity, (ii) changes in core and face properties, and (iii) air-backed and water-backed configurations on dynamic response. The objective is to quantify the relationship between the response of the structures, loading intensities, material properties and structural attributes. The loading configuration is shown in Figure 2, and the sandwich plate studied is shown in Figure 1. Although five different impulsive load levels are considered, for brevity we focus on the deformation histories for the load intensity of $\bar{I} = 0.2$ in the following section.

The results of the finite element simulations are compared with experimental results in the literature. Figure 4 shows the deformed configurations of a light-core sandwich structure ($\overline{M}_C = 0.197$) with a prismatic core subjected to impulsive loading with $\bar{I} = 0.2$. Results are compared to simulations for the sandwich structure with $\overline{M}_C = 0.2$. Comparing the simulations with experimental measurements shows that the simulations capture a majority of the details of the deformation mechanisms quite realistically. These include core wall buckling, core shearing and stress concentrations near the clamped edges. The debonding due to core wall buckling is also represented in the simulations. In both the simulations and experiments, the face sheets undergo yielding but do not experience fracture and separation from the supports. The front face experiences tensile stretching while the back face is relatively undamaged. The experimental results are obtained by Dharmasena et al. [2008]. In experiments, different masses of TNT at a fixed standoff distance of 10 cm are used to create impulsive loads. In experiments, the core has a wall thickness of 0.76 mm and the face sheet thickness is 5 mm, such that $\overline{M}_C = 0.197$, compared to $\overline{M}_C = 0.2$ in simulations. The comparison between experiments and simulations shows good agreement in terms of damage mechanisms and structural deformation. Overall, experimentally observed deformation mechanisms are reasonably replicated in the simulations.
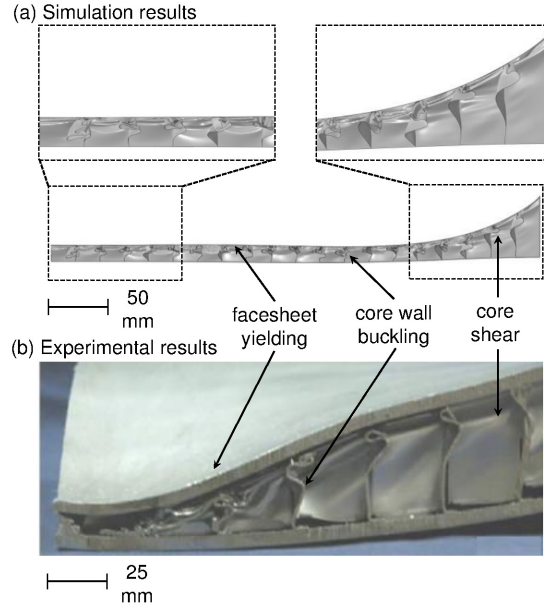
Figure 4. Comparison of computational and experimental deformation modes in a sandwich panel subjected to an impulsive load. Experimental results are obtained from [Dharmasena et al. 2008]. The sandwich core consists of a square honeycomb topology with $\overline{M}_C = 0.197$ for experiments and $\overline{M}_C = 0.20$ for the simulations.
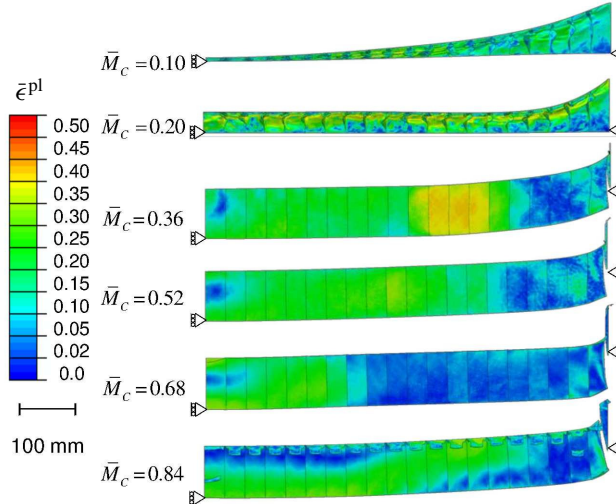
Figure 5. Distributions of equivalent plastic strain for *air-backed* structures with different $\overline{M}_C$ values and an impulse of $\overline{I} = 0.2$. The overall deflection increases as $\overline{M}_C$ increases. The structure with $\overline{M}_C = 0.10$ exhibits the most deformation through corewall buckling. Structures with $\overline{M}_C > 0.2$ experience core-stretching and shear rupture. The corresponding front- and back-face masses are given in Table 1.
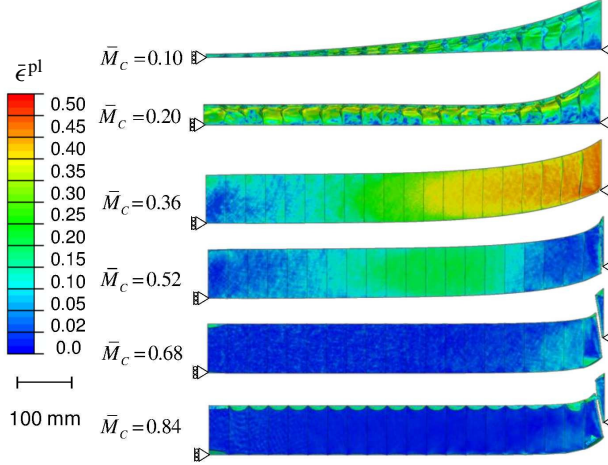
4.2. *Deformation mechanisms in air-backed structures.* Figure 5 shows the distributions of equivalent plastic strain for structures with different values of $\overline{M}_C$ for $\overline{I} = 0.2$ at $t = 1000\,\mu$s. This figure reveals the role of core stiffness. For $\overline{M}_C = 0.10$, the lightest core, the response is dominated by core wall buckling and front face stretching, with no rupture. For $\overline{M}_C = 0.20$, core wall buckling and stretching occur simultaneously, with the onset of rupture delayed due to higher core compliance. Structures with $\overline{M}_C = 0.10$ and $\overline{M}_C = 0.20$ are the only cases showing no rupture up to $t = 1000\,\mu$s. As $\overline{M}_C$ increases beyond 0.20, the failure mode changes from tensile stretching and core wall buckling to shear-dominated rupture. The configurations with $\overline{M}_C = 0.36$, 0.54 and 0.68 exhibit fracture and catastrophic failure due to localized deformation. Clearly, equitable distribution of mass between the front face, core and back face does not provide optimal blast mitigation. For $\overline{M}_C = 0.84$, the case with the heaviest core considered, the core-face junctions are locations of severe stress concentration and failure.

For all cases considered, two competing deformation mechanisms — core compression and overall beam bending — are observed. Light-core structures undergo severe core compression without significant bending. Light cores allow the structure to attain a common velocity after $\sim 600\,\mu$s for $\overline{M}_C = 0.20$ and $\sim 800\,\mu$s for $\overline{M}_C = 0.10$; these times are five times longer than those for heavy core structures. Structures with $0.04 < \overline{M}_C \leq 0.20$ do not undergo shear rupture. On the other hand, heavy cores minimize core crushing and lead to significant bending deformation, ultimately causing rupture. The structure acquires a common velocity after $\sim 250\,\mu$s for $\overline{M}_C = 0.84$ and $\sim 350\,\mu$s for $\overline{M}_C = 0.52$.

4.3. *Deformation mechanisms in water-backed structures.* A comparison of the results for air-backed and water-backed structures reveals significant differences in deformation and failure mechanisms. The presence of a dense medium (water) on both sides of the structure prevents large scale bending and leads to higher internal energy dissipation. The absence of bending leads to greater front face-core interactions and core compression but creates a cushioning effect for the back face. To quantify the differences between these two configurations, a comparative study is carried out.

Figure 6 shows the distributions of equivalent plastic strain for water-backed structures with different $\overline{M}_C$ values and $\overline{I} = 0.2$ at $t = 1000\,\mu$s. For $\overline{M}_C = 0.10$, the core has very low resistance to wall buckling and, consequently, core-crushing initiates upon the onset of loading. When the core collapses, the front face strikes the back face and the stress wave passes through the back face into the surrounding water. For $\overline{M}_C = 0.20$, structural deflection as well as core wall buckling are observed. For $\overline{M}_C = 0.34$, core crushing is negligible and core stretching is more intense than those for structures with $\overline{M}_C = 0.20$ and $\overline{M}_C = 0.10$. Due to the presence of the back-side water, the back-face displacement is very small and no rupture is observed near the support. However, for all structural configurations with $\overline{M}_C > 0.36$, rupture initiates near the support in the front face, core and back face. As core mass increases, the stress concentration near the support becomes more severe and causes fracture and separation. Clearly, heavy cores are detrimental to blast resistance in both air-backed and water-backed structures.

Although heavy core designs are undesirable under both air-backed and water-backed conditions, water-backed structures with heavy cores can sustain larger impulses because a large fraction of the incident impulse is transmitted through the back face into the surrounding water and structural deflection is constrained. A major distinction between air-backed and water-backed structures is that in air-backed structures, the impulse is transmitted to the supports while in water-backed structures, the impulse is transmitted to the surrounding water.

Figure 6. Distributions of equivalent plastic strain for *water-backed* structures with different $\overline{M}_C$ values and an impulse of $\overline{I} = 0.2$. The overall deflection is essentially the same for all values of $\overline{M}_C$. The structure with $\overline{M}_C = 0.10$ exhibits the most deformation through core-wall buckling. Structures with $\overline{M}_C > 0.36$ show shear rupture. The corresponding front- and back-face masses are given in Table 1.

4.4. *Deflection.* To evaluate and compare the responses, the deflections at the midpoints of the back faces at $600\,\mu s$ for six different sandwich structures and five different impulse magnitudes are measured and compared. The deflections are normalized by the length of the structure span. Figure 7 shows the normalized deflection Δ/L in the front face and back face as a function of normalized core mass $\overline{M}_C$ and normalized impulse $\overline{I}$ for air-backed and water-backed structures. As discussed previously, structures with low $\overline{M}_C$ exhibit higher core compression and, as $\overline{M}_C$ increases, core compression decreases. For $\overline{M}_C \leq 0.20$, the front face deflects much more than the back face due to high core compression. Conversely, for $\overline{M}_C > 0.20$, the front and back faces undergo essentially the same deflection due to negligible core compression. For $\overline{I} > 0.2$, the cases with $\overline{M}_C > 0.20$ undergo rupture near the support, leading to higher overall deflections, while the cases with $\overline{M}_C \leq 0.20$ experience core crushing but no rupture. This is reflected in the large jump in the deflection between $\overline{M}_C = 0.20$ and $\overline{M}_C = 0.36$ for $\overline{I} = 0.3$ and $\overline{I} = 0.4$. At high impulse magnitudes, $\overline{M}_C \leq 0.20$ provides superior blast resistance. The structure-performance relations useful for sandwich structure design have been presented using the form

$$z = A \cdot x^m \cdot y^n, \tag{15}$$

where z is a performance parameter (Δ/L, $\overline{U}$ or $\overline{I}_T$), x is a structural attribute ($\overline{M}_C$, $\overline{M}_{FF}$ or $\overline{M}_{BF}$), y is the load intensity and A, m and n are constants specific to each load configuration (air-backed, water-backed). More details about the structure-performance relations are provided in Section 4.9. The relationship between deflection in air-backed structures $(\Delta/L)_{AB}$, and incident impulse ($\overline{I}$) and normalized core mass ($\overline{M}_C$) can be quantified by

$$(\Delta/L)_{AB} = 1.58 \cdot (\overline{M}_C)^{0.24} \cdot \overline{I}^{0.86}. \tag{16}$$
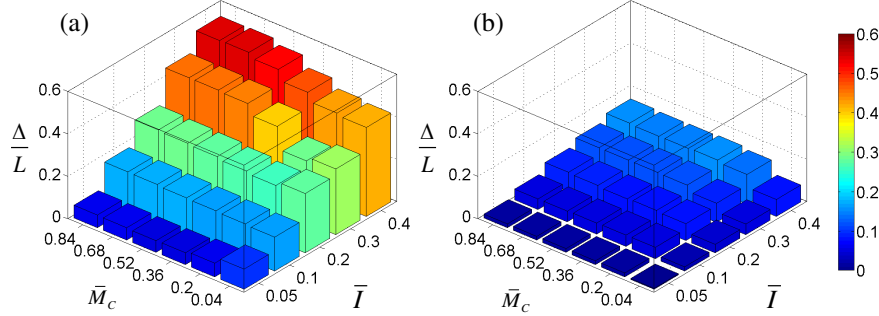
Figure 7. Normalized deflection Δ/L as a function of normalized core-mass $\overline{M}_{\mathrm{C}}$ and normalized impulse $\bar{I}$ for (a) air-backed and (b) water-backed structures. The corresponding front- and back-face masses are given in Table 1.

Figure 7(b) shows the deflection for water-backed structures as a function of normalized core mass $\overline{M}_{\mathrm{C}}$ and normalized impulse $\bar{I}$. Due to the presence of water on both sides of the structure, deflection is limited. As the load intensity increases from $\bar{I} = 0.05$ to $\bar{I} = 0.4$, the increase in the overall deflection is relatively minor. Compared with the defection in air-backed structures, the deflection for water-backed cases is $\sim 70\%$ lower for $\overline{M}_{\mathrm{C}} \leq 0.20$ and $\sim 40\%$ lower for $\overline{M}_{\mathrm{C}} > 0.20$ at high load magnitudes. For both air-backed and water-backed structures, the minimum value of Δ/L is seen for $\overline{M}_{\mathrm{C}} \leq 0.20$. Cores with wall buckling as the primary deformation mechanism show superior blast resistance than cores with core stretching as the primary deformation mechanism. The lower deflection values in water-backed cases have a significant influence on energy absorption. The relationship between deflection in water-backed structures $(\Delta/L)_{\mathrm{WB}}$, and incident impulse $(\bar{I})$ and normalized core mass $(\overline{M}_{\mathrm{C}})$ can be quantified by

$$(\Delta/L)_{\mathrm{WB}} = 0.43 \cdot (\overline{M}_{\mathrm{C}})^{0.22} \cdot \bar{I}^{0.85}. \tag{17}$$

4.5. *Energy absorption.* When an impulsive wave interacts with a structure, a number of energy dissipation mechanisms are activated. A significant fraction of the incident energy is dissipated through plastic deformation. The primary mechanisms of plastic dissipation include tensile stretching in the front face, core walls and back face, and core-wall buckling. A nondimensionalized dissipation measure is

$$\overline{U} = \frac{U}{L \cdot W \cdot \sigma_y \cdot (M_{\mathrm{Total}}/\rho_{\mathrm{Steel}})}, \tag{18}$$

where U is the total dissipation through plasticity; L, W and M_{Total} are the length, width and total areal mass of the sandwich structure, respectively; and σ_y and ρ_{Steel} are the yield stress and density of steel, respectively.

It is important to understand how the dissipation is distributed in the structures. In particular, the rate of dissipation as a function of time in different components of a structure can highlight regions that have the most influence on the total energy dissipation. Figure 8 shows the time histories of dissipation in different parts of a structure with $\overline{M}_{\mathrm{C}} = 0.10$ under $\bar{I} = 0.2$ for air-backed and water-backed conditions. In the air-backed case, energy absorption in the core and front face occurs simultaneously and at approximately the same rate. The motion of the front face causes core compression, plastic stretching in the front face
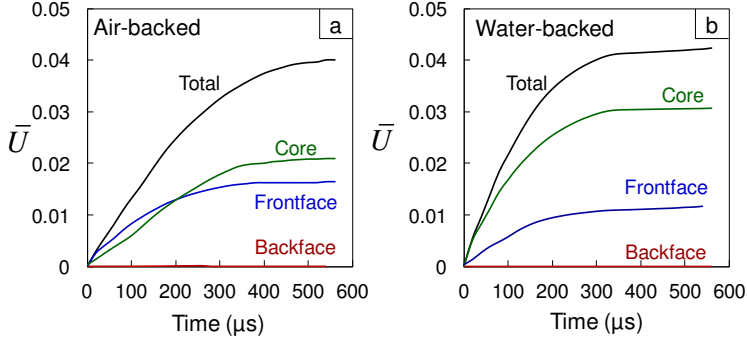
Figure 8. Plastic dissipation in (a) air-backed and (b) water-backed structures with $\overline{M}_C = 0.20$ subjected to an impulse $\overline{I} = 0.2$. The corresponding front- and back-face masses are given in Table 1.

and core-wall buckling. At $t = 200\,\mu s$, dissipation in the core surpasses that in the front face. The back face experiences negligible plastic deformation. In the water-backed structures, the low overall deflection limits the stretching of the front face and back face. Since the compressive strain in the core is much higher than that in the air-backed case, a much higher fraction of total energy absorption occurs in the core. Specifically, the core dissipates $\sim 40\%$ of the total energy in the air-backed case and $\sim 80\%$ of the total energy in the water-backed case. The time scales for the two cases are also different, with the dissipation reaching a maximum value at $\sim 500\,\mu s$ in the air-backed case and at $\sim 300\,\mu s$ in the water-backed case.

Figure 9 shows the normalized dissipation $\overline{U}$ in the entire structure as a function of core mass $\overline{M}_C$ and impulse $\overline{I}$ for air-backed and water-backed structures. Air-backed structures with $\overline{M}_C = 0.10$ experience low deflection and low core compression and hence absorb $\sim 20\%$ lesser energy than structures with $\overline{M}_C = 0.20$, which experience high levels of dissipation because the core webs are sufficiently thin to stretch under tensile loading induced by large deflections and sufficiently thick to prevent core-wall buckling. Structures with $\overline{M}_C > 0.20$ absorb less energy because of rupture due to localized plastic deformation and damage. Plastic dissipation ceases when the structures separate from the supports. The relationship between plastic dissipation in air-backed structures ($\overline{U}_{AB}$), and incident impulse ($\overline{I}$) and normalized core mass ($\overline{M}_C$) can be given by

$$\overline{U}_{AB} = 0.22 \cdot (\overline{M}_C)^{-0.20} \cdot \overline{I}^{1.07}. \tag{19}$$

In Figure 10, the energy absorption in water-backed structures as a function of normalized core mass $\overline{M}_C$ and impulse $\overline{I}$ follows a trend similar to that for air-backed structures, with the dissipation in the core accounting for the largest fraction of the total dissipation. The energy imparted to a sandwich structure during an underwater blast is partly converted to kinetic energy when the structure acquires velocity and deflects. In the air-backed cases, this kinetic energy is dissipated over a duration of $\sim 500\,\mu s$ through face-sheet stretching, core deformation and rupture. Since water-backed structures experience low deflections and attain lower velocities, the incident energy is partially dissipated in the structure through plastic deformation and partially transmitted to the back-side water. Water-backed structures absorb $\sim 20\%$ more energy than air-backed structures under the same incident impulse, primarily due
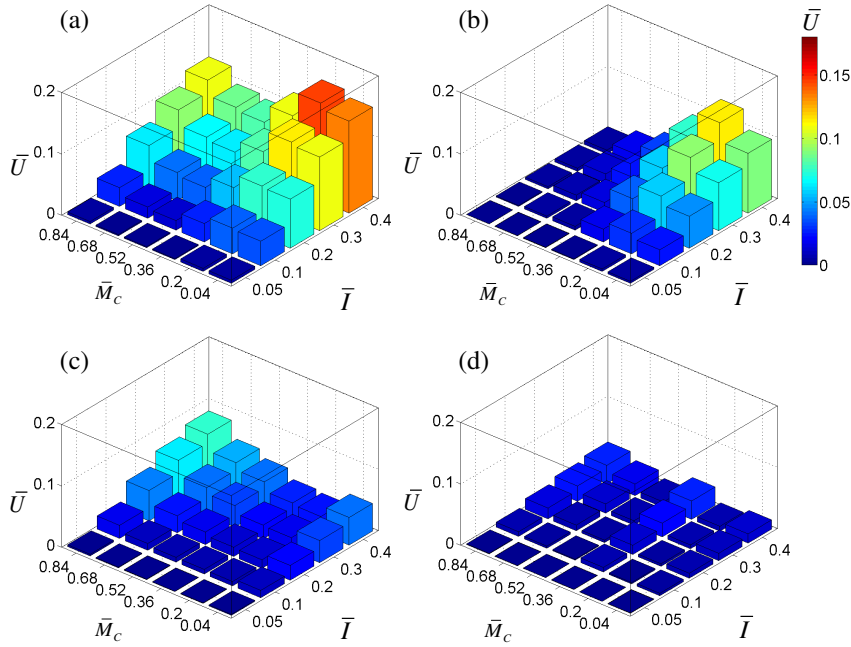
Figure 9. Normalized plastic dissipation $\overline{U}$ in air-backed structure as a function of normalized core-mass $\overline{M}_C$ and normalized impulse $\overline{I}$ for (a) entire structure, (b) core, (c) front face and (d) back face. The corresponding core, front-face and back-face masses are given in Table 1.

to more extensive core crushing. The differences in energy dissipation between air-backed and water-backed structures are negligible for $\overline{M}_C > 0.20$ under the loading conditions analyzed for the lack of plasticity. The relationship between plastic dissipation in air-backed structures ($\overline{U}_{WB}$), and incident impulse ($\overline{I}$) and normalized core mass ($\overline{M}_C$) can be stated as

$$\overline{U}_{WB} = 0.20 \cdot (\overline{M}_C)^{-0.21} \cdot \overline{I}^{0.69}. \tag{20}$$

4.6. *Transmitted pressure in water-backed cases.* The transmitted pressure in the back-side water is a useful parameter for quantifying the effectiveness of sandwich structures under water-backed conditions. It has significant implications for structures like cargo ships, oil tankers and pipelines. Figure 11(a) shows the histories of the downstream pressure for structures with $\overline{M}_C = 0.10$ to 0.84 under an impulse of $\overline{I} = 0.2$ which has a peak pressure of 80 MPa. For $\overline{M}_C = 0.52, 0.68$ and 0.84, the time delay for pressure transmission through the sandwich structure is $\sim 50\,\mu$s. The transmitted pressure shows an exponentially decaying profile with a peak value of 80 MPa and decay time of 600 μs. For $\overline{M}_C = 0.36$, the time delay for pressure transmission through the structure is $\sim 100\,\mu$s and the peak value and decay time of the transmitted pulse are 80 MPa and $\sim 600\,\mu$s, respectively. For $\overline{M}_C = 0.20$, the transmitted peak pressure is $\sim 30\%$ lower or approximately 55 MPa and the decay time is $\sim 400\,\mu$s. For structures with $0.20 < \overline{M}_C < 0.84$, cavitation occurs at the interface between the back face and water section. Structures with $\overline{M}_C = 0.10$ show considerably different response. Initially, cell wall buckling occurs as
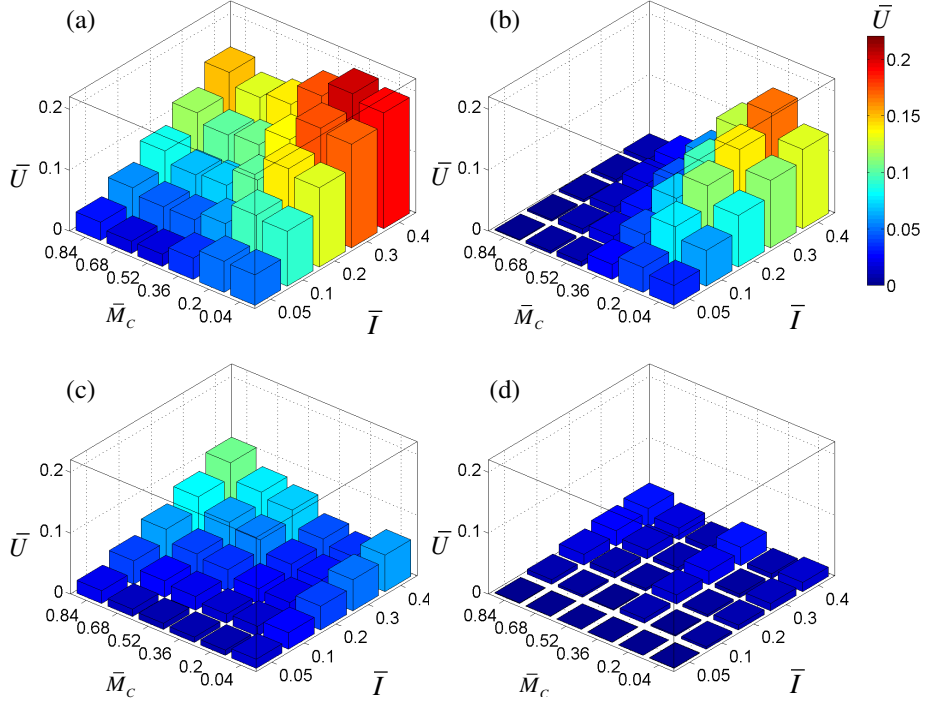
Figure 10. Normalized plastic dissipation $\overline{U}$ in water-backed structure as a function of normalized core-mass $\overline{M}_C$ and normalized impulse $\overline{I}$ for (a) entire structure, (b) core, (c) front face and (d) back face. The corresponding core, front-face and back-face masses are given in Table 1.
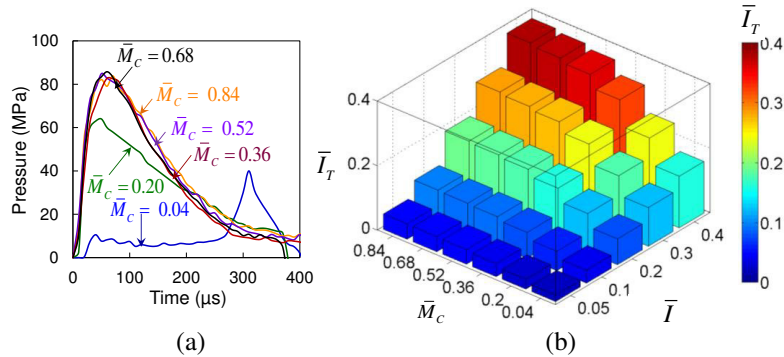

Figure 11. (a) Impulse transmission histories for $\overline{I} = 0.20$, and (b) transmitted impulse as a function of incident impulse $\overline{I}$ and normalized core mass $\overline{M}_C$, with $\overline{M}_C = 0.10$ to 0.84. For $\overline{M}_C = 0.20$, there is a reduction of $\sim 60\%$ in transmitted pressure relative to the incident pressure. The corresponding front- and back-face masses are given in Table 1.
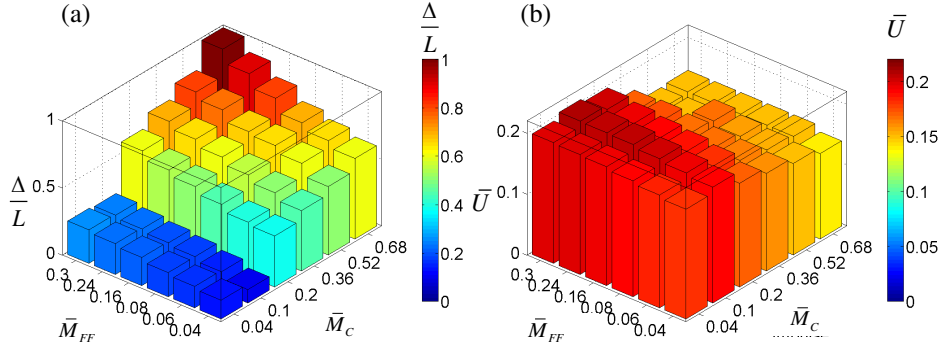
Figure 12. Normalized deflection Δ/L and plastic dissipation $\overline{U}$ in air-backed structures as functions of $\overline{M}_C$ and $\overline{M}_{FF}$. Minimum deflection is observed for $\overline{M}_C = 0.10$. The changes in $\overline{M}_C$ have a greater effect on deflections than changes in $\overline{M}_{FF}$. There is only a relatively minor variation of energy dissipation with $\overline{M}_C$ and $\overline{M}_{FF}$.

the stress wave passes through the core. The pressure transmitted through the structure is much lower, at only 10 MPa during core crushing and reaching 40 MPa upon the completion of core crush. This value is 50% of what is seen for the structure with $\overline{M}_C > 0.36$ and 90% of that for $\overline{M}_C = 0.20$. On the other hand, cavitation is negligible for $\overline{M}_C = 0.10$. Figure 11(b) shows the transmitted impulse as a function of normalized core mass $\overline{M}_C$ and incident impulse $\overline{I}$. The relationship between transmitted impulse ($\overline{I}_{T,\mathrm{WB}}$), and incident impulse ($\overline{I}$) and normalized core mass ($\overline{M}_C$) can be quantified by

$$\overline{I}_{T,\mathrm{WB}}/\overline{I} = 1.36 \cdot (\overline{M}_C)^{0.33}. \tag{21}$$

4.7. *Optimal core mass.* The previous section dealt with the role of load intensity and core mass on the dynamic response of the structures. The structure-property relations developed indicate that optimal core mass lies between 4% and 20% of the total sandwich structure mass. To further refine the analysis, a set of simulations is carried out by varying the core and front face masses while the total areal mass is held constant. Specifically, the core mass is varied from 4% to 68% of the total mass, while the front face mass is varied from 4% to 30% of the total mass. In each case, the back face mass is given by (1).

Figure 12(a) shows the normalized deflection as a function of $\overline{M}_C$ and $\overline{M}_{FF}$ for $\overline{I} = 0.5$. The results indicate that $\overline{M}_C$ has a higher influence on deflection than $\overline{M}_{FF}$ and confirm that heavy cores are detrimental to blast resistance. As the front face mass increases, the momentum transferred to the core increases, causing higher core compression and overall deflection. The highest deflection is observed for structures with maximum core and front face masses ($\overline{M}_C = 0.68$ and $\overline{M}_{FF} = 0.3$). Although core wall buckling is an essential deformation mechanism for improved blast resistance, extremely thin core walls ($\overline{M}_C = 0.04$) can be detrimental to blast resistance, indicating that there exists a lower limit for core mass fraction. It can be concluded that the upper limit of core mass fraction is 20% while the lower limit of core mass fraction is 4% of total structural mass. Results show that structures with $\overline{M}_C = 0.20$ undergo the least deflections due to the fact that the thickness of the core webs is sufficiently low to enable buckling and load spreading and sufficiently high to prevent complete core collapse.
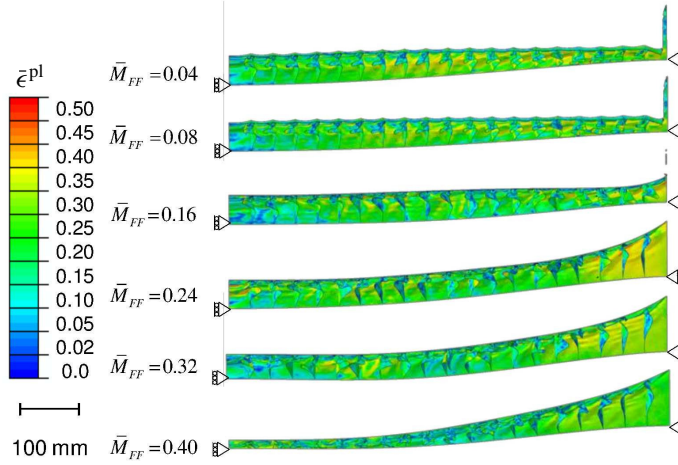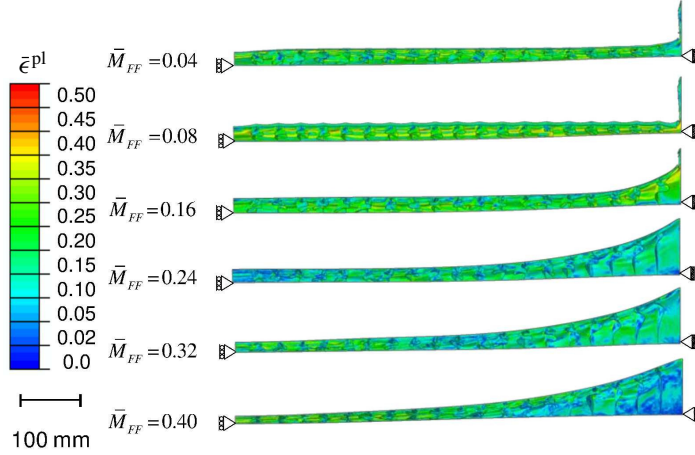
Figure 13. Distributions of equivalent plastic strain for *air-backed* structures with varying $\overline{M}_{FF}$ and $\overline{M}_C = 0.20$ subjected to an impulse of $\overline{I} = 0.2$. As $\overline{M}_{FF}$ increases, the susceptibility to rupture decreases. However, heavy front faces allow lead to more severe core compression and higher deflections.

Figure 12(b) shows plastic dissipation as a function of $\overline{M}_C$ and $\overline{M}_{FF}$ for the highest impulsive load intensity ($\overline{I} = 0.5$). There are relatively minor variations in energy dissipation over the entire tested range of core and front face masses. The general trend observed in core optimization is also evident in this analysis, i.e., structures with heavy cores experience large-scale rupture and bending and show lower energy dissipation than light cores. The front face mass has a significant influence on both deflection and energy dissipation.

4.8. *Optimization of front-face mass.* Evaluations of the response of sandwich structures with different core strengths reveal that structures with $\overline{M}_C \leq 0.20$ provide the best blast mitigation for the conditions analyzed. Specifically, results show that $\overline{M}_C = 0.20$ provides high blast resistance. Furthermore, the results indicate that the front and back faces influence the deflection and energy dissipation in the entire structure. To quantify this influence, the front-face and back-face thicknesses are varied as shown in Table 2 while the core mass is maintained at $\overline{M}_C = 0.20$. Thus, the core constitutes 20% of the total mass and core-wall buckling is the preferred deformation mechanism. The front-face mass ($\overline{M}_{FF}$) is varied from 0.04 to 0.40 and the back-face mass ($\overline{M}_{BF}$) is varied from 0.76 to 0.40, as shown in Table 2.

Figure 13 shows the contour plots of equivalent plastic strain at $1000\,\mu s$ in air-backed structures with varying $\overline{M}_{FF}$ subjected to $\overline{I} = 0.2$. Since the core mass is only 10% of the total mass, the response of the core is primarily in the form of core wall buckling. For structures with $\overline{M}_{FF} = 0.04$ and $\overline{M}_{FF} = 0.08$, the front face is very light and ruptures due to shear stress concentrations near the supports, followed by core-wall buckling and core compression. For structures with $\overline{M}_{FF} = 0.16$, the front face ruptures due to tensile necking near the supports, followed by core wall buckling and core compression. For structures with $\overline{M}_{FF} = 0.24$, the front face has sufficient strength to avoid shear or tensile failure. However, since the front face is heavier, the overall deflection is higher than those for structures with $\overline{M}_{FF} < 0.24$. As $\overline{M}_{FF}$ increases from 0.24 to 0.40, the front face becomes less susceptible to tensile necking and

Figure 14. Distributions of equivalent plastic strain for *water-backed* structures with varying $\overline{M}_{\text{FF}}$ and $\overline{M}_{\text{C}} = 0.20$ subjected to an impulse of $\overline{I} = 0.2$. Heavy front faces cause progressively higher core compression as the overall deflection remains constant due to the downstream water.

rupture. However, as the front-face mass increases, more severe core compression and higher overall deflection are observed. For impulses up to $\overline{I} = 0.3$, air-backed structures with $\overline{M}_{\text{FF}} \sim 0.25$, $\overline{M}_{\text{C}} \sim 0.20$ and $\overline{M}_{\text{BF}} \sim 0.65$ show superior blast mitigation capability. Although configurations with $\overline{M}_{\text{FF}} < 0.24$ experience front-face rupture, none experience complete failure. This reinforces the fact that dynamic response is highly influenced by core mass and it is relatively less sensitive to front face mass.

Figure 14 shows the contour plots of equivalent plastic strain at $1000\,\mu\text{s}$ in water-backed sandwich structures with varying $\overline{M}_{\text{FF}}$ subjected to $\overline{I} = 0.2$. The failure mode for structures with $\overline{M}_{\text{FF}} = 0.04, 0.08$ and 0.16 is front-face rupture near the supports followed by rapid core compression. Since the back face is constrained by back-side water, core compressive strains are much higher than those in air-backed structures. To prevent complete core collapse in the water-backed cases, it is necessary to keep $\overline{M}_{\text{FF}}$ above a minimum value ($\overline{M}_{\text{FF}} = 0.24$). For impulses up to $\overline{I} = 0.3$, structures with $\overline{M}_{\text{FF}} \sim 0.25$, $\overline{M}_{\text{C}} \sim 0.10$ and $\overline{M}_{\text{BF}} \sim 0.65$ perform the best.

Figure 15 shows the normalized deflection Δ/L as a function of normalized front-face mass $\overline{M}_{\text{FF}}$ and normalized impulse magnitude $\overline{I}$ in air-backed and water-backed structures. As $\overline{M}_{\text{FF}}$ increases from 0.04 to 0.40, the deflection in air-backed structures increases. Structures with $\overline{M}_{\text{FF}} = 0.04$ experience the smallest deflection, while those with $\overline{M}_{\text{FF}} = 0.24$ and 0.40 experience deflections two and four times those for structures with $\overline{M}_{\text{FF}} = 0.04$, respectively. For water-backed structures, as $\overline{M}_{\text{FF}}$ increases, the overall deflection remains essentially constant due to the presence of downstream water. However, contour plots in Figures 15 and 16 show that structures with $\overline{M}_{\text{FF}} < 0.24$ are susceptible to front-face rupture. Consequently, the lowest acceptable value of $\overline{M}_{\text{FF}}$ is 0.24 for both air-backed and water-backed structures. The relationship between deflection $(\Delta/L)_{\text{WB}}$, incident impulse $\overline{I}$ and normalized core mass $\overline{M}_{\text{C}}$ in air-backed structures can be stated as

$$(\Delta/L)_{\text{AB}} = 0.23 \cdot (\overline{M}_{\text{FF}})^{0.27} \cdot \overline{I}^{0.62}, \tag{22}$$
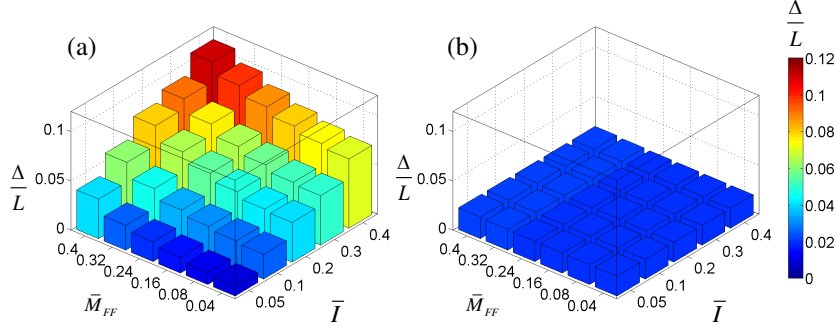
Figure 15. Deflection in (a) air-backed and (b) water-backed structures as functions of incident impulse $\bar{I}$ and normalized front-face mass $\overline{M}_{\text{FF}}$ ($\overline{M}_{\text{C}} = 0.20$).
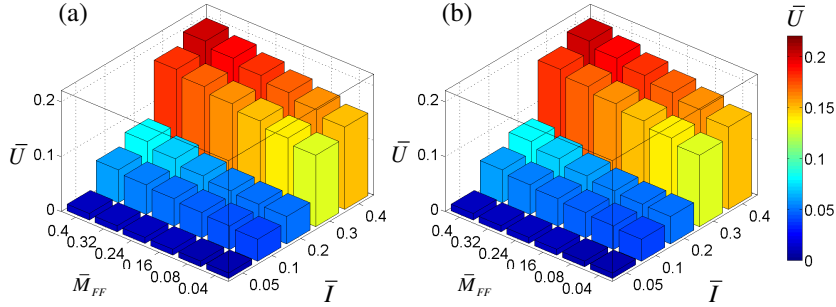
Figure 16. Energy dissipated due to plastic deformation in (a) air-backed and (b) water-backed structures as functions of incident impulse $\bar{I}$ and normalized front-face mass $\overline{M}_{\text{FF}}$ ($\overline{M}_{\text{C}} = 0.20$).

while that for water-backed structures can be stated as

$$(\Delta/L)_{\text{WB}} = 0.02 \cdot (\overline{M}_{\text{FF}})^{0.03} \cdot \bar{I}. \tag{23}$$

Figure 16 show normalized plastic dissipation $\bar{U}$ as a function of normalized front-face mass $\overline{M}_{\text{FF}}$ and impulse magnitude $\bar{I}$ in air-backed and water-backed sandwich structures. For thin front faces ($\overline{M}_{\text{FF}} <$ 0.24), the stress wave is transmitted through the front face and into the core after the onset of loading. Tensile necking near the supports leads to rupture in the front face. Consequently, for structures with $\overline{M}_{\text{FF}} < 0.24$, plastic dissipation in the core exceeds that in the front face. As $\overline{M}_{\text{FF}}$ increases and the front face becomes thicker, the amount of plastic deformation in the front face increases and, as a result, the front face becomes less susceptible to rupture. Hence, the contribution of the front face to total plastic dissipation increases and that of the core decreases. For $\overline{M}_{\text{FF}} = 0.4$, plastic dissipation in the front face is higher than that in the core. As discussed previously, for the same incident impulse, water-backed structures (Figure 15(b)) absorb a larger fraction of incident energy than air-backed structures. This occurs primarily through higher core-compressive strains and front-face shearing. However, the front-face plastic dissipation surpasses plastic dissipation in the core only for thick front faces with $\overline{M}_{\text{FF}} = 0.4$. The relationship between plastic dissipation $\bar{U}$ in both air-backed and water-backed structures, incident
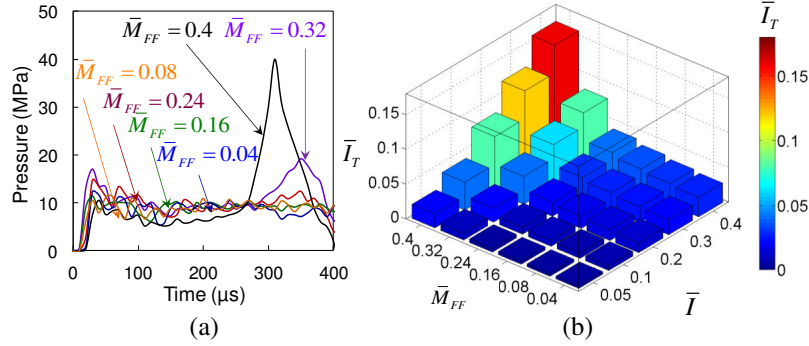
Figure 17. (a) Impulse transmission histories for $\bar{I} = 0.20$, and (b) transmitted impulse as a function of incident impulse $\bar{I}$ and normalized front-face mass $\overline{M}_{FF}$ in water-backed structures ($\overline{M}_C = 0.20$).

impulse $\bar{I}$ and normalized core mass $\overline{M}_C$ for both air-backed and water-backed structures is

$$\overline{U} = 0.67 \cdot (\overline{M}_{FF})^{0.13} \cdot \bar{I}^{1.14}. \tag{24}$$

Figure 17(a) shows the histories of transmitted pressure for water-backed structures with $\overline{M}_C = 0.20$ and varying $\overline{M}_{FF}$. The values are measured in the middle of the downstream water section. The transmitted pressure remains constant during core compression. When the core fails completely and the front face and the back face move together, a secondary pressure pulse is transmitted into the downstream water. The secondary pressure pulses for structures with $\overline{M}_{FF} = 0.24$, 0.32 and 0.40 are higher in magnitude than those for structures with $\overline{M}_{FF} = 0.08$, 0.16 and 0.24, due to the greater momentum acquired by the heavier front faces. As demonstrated previously, structures with $\overline{M}_{FF} \leq 0.16$ undergo front-face rupture followed by core crushing and tearing near the supports. A combination of front-face mass of $\overline{M}_{FF} \leq 0.24$, core mass of $\overline{M}_C = 0.10$ and back-face mass $\overline{M}_{BF} = 0.65$ provides the highest blast mitigation for air-backed as well as water-backed structures. The relationship between the transmitted impulse $\bar{I}_{T,WB}$, the incident impulse $\bar{I}$ and normalized core mass $\overline{M}_C$ (Figure 17(b)) can be given by

$$\bar{I}_{T,WB}/\bar{I} = 2.82 \cdot (\overline{M}_{FF})^{2.19}. \tag{25}$$

4.9. Structure-performance relationships. The preceding discussions have focused on the deformation, deflection, energy dissipation and impulse transmission in metallic sandwich structures subjected to underwater impulsive loads. In particular, the results of parametric studies have been presented in a format wherein the response variables are functions of the loading $\bar{I}$ and structural attributes ($\overline{M}_C$, $\overline{M}_{FF}$ or $\overline{M}_{BF}$). Analyses show that such contact conditions play an important role in the response of sandwich structures to underwater blasts. Structural design must satisfy prescribed performance objectives through identification of proper structural attributes that fulfill the requirements. Here, deflection, impulse transmission, and energy dissipation are taken as the performance metrics. These metrics may pose competing requirements on structure attributes. In both air-backed and water-backed structures, the energy dissipated in the entire structure follows a similar trend. Deflection is a relatively less useful metric in water-backed structures due to the fact that the presence of downstream water keeps deflection small. In such cases,

Figure	Contact condition	Acceptance metric	Structure-performance relations
Figure 7(a)	Air-backed	Deflection	$(\Delta/L)_{\mathrm{AB}} = 1.58\,(\overline{M}_{\mathrm{C}})^{0.24}\,\bar{I}^{0.86}$
Figure 9(a)		Energy dissipation	$\overline{U}_{\mathrm{AB}} = 0.22\,(\overline{M}_{\mathrm{C}})^{-0.20}\,\bar{I}^{1.07}$
Figure 7(b)	Water-backed	Deflection	$(\Delta/L)_{\mathrm{WB}} = 0.43\,(\overline{M}_{\mathrm{C}})^{0.22}\,\bar{I}^{0.85}$
Figure 9(b)		Energy dissipation	$\overline{U}_{\mathrm{WB}} = 0.20\,(\overline{M}_{\mathrm{C}})^{-0.21}\,\bar{I}^{0.69}$
Figure 11(b)		Impulse transmission	$\bar{I}_{T,\mathrm{WB}}/\bar{I} = 1.36\,(\overline{M}_{\mathrm{C}})^{0.33}$

Table 4. Summary of material-structure-property relationships for core optimization.

Figure	Contact condition	Acceptance metric	Structure-performance relations
Figure 15(a)	Air-backed	Deflection	$(\Delta/L)_{\mathrm{AB}} = 0.23\,(\overline{M}_{\mathrm{FF}})^{0.27}\,\bar{I}^{0.62}$
Figure 15(b)		Energy dissipation	$\overline{U}_{\mathrm{AB}} = 0.67\,(\overline{M}_{\mathrm{FF}})^{0.13}\,\bar{I}^{1.14}$
Figure 15(c)	Water-backed	Deflection	$(\Delta/L)_{\mathrm{WB}} = 0.02\,(\overline{M}_{\mathrm{FF}})^{0.03}\,\bar{I}$
Figure 15(d)		Energy dissipation	$\overline{U}_{\mathrm{WB}} = 0.67\,(\overline{M}_{\mathrm{FF}})^{0.13}\,\bar{I}^{1.14}$
Figure 17(b)		Impulse transmission	$\bar{I}_{T,\mathrm{WB}}/\bar{I} = 2.82\,(\overline{M}_{\mathrm{FF}})^{2.19}$

Table 5. Summary of material-structure-property relationships for front-face optimization.

the transmitted impulse (measured in the back-side water section) may be a more relevant and useful quantity. The structure-performance relations are summarized in Table 4 and Table 5.

An optimal sandwich structure design needs to balance low deflection and high energy dissipation. This balance is application-specific and may not be universal. The relations developed in this study allow the identification of optimal structural designs for given combination of deflection, energy dissipation and impulse transmission requirements. For a given level of deflection or energy dissipation, the optimum value of core or face masses for a specific impulsive load can be achieved by varying the component thicknesses. The focus of this analysis is on the development of quantitative relations which can be used by structural designers. As discussed previously, core mass is the most critical structural attribute of a sandwich structure. Although (16) gives a simple relationship between core mass, impulse magnitude and deflection, it must be noted that $\overline{M}_{\mathrm{C}} = 0.04$ is the *lower* limit of core mass. The material-structure-performance relations can be used to inform structural design with the precaution that they should only be used for the material, structural parameter ranges and loading conditions considered.

5. Concluding remarks

To be resilient to impulsive loading, structures must balance rigidity, load-carrying capacity and an ability to dissipate energy. Sandwich composites, with a combination of stiff face sheets and compliant cores, can provide high shear and bending resistances, as well as an ability to absorb energy. In an effort to provide quantitative relations for structural design, we have evaluated the performance in terms of deflection and energy-dissipation of metal sandwich structures under high-intensity impulsive loading over a range of structural attributes and loading. In particular, the conditions analyzed involve impulsive loads with peak pressures up to 450 MPa and impulses up to 41 kPa·s. This range of load profiles is

indicative of the effects at different standoff distances of $100\,\mathrm{kg}$ of TNT detonating underwater. The present work has focused on the damage and deformation occurring in blast-loaded metallic sandwich plates in the early stages of deformation and the role of loading intensity and structural attributes on dynamic performance. The constitutive and damage models used in the analysis are capable of capturing the effects of different inelastic deformation and failure mechanisms in the face sheets and sandwich cores. The calculations have yielded the following findings.

There is a close relationship between structural parameters, loading rates and dynamic performance. The performance of metallic sandwich structures is significantly influenced by core mass and core wall thickness. For cores with $\overline{M}_\mathrm{C} > 0.20$, deformation is dominated by bending and core-stretching. For cores with $\overline{M}_\mathrm{C} \leq 0.20$, deformation is dominated by core-wall buckling and front-face stretching. Although light core structures provide significantly higher blast mitigation compared to heavy core structures on a per-unit weight basis, there exists a lower limit of core mass below which the structural benefits of light cores are lost due to core collapse. This lower limit is approximately $\overline{M}_\mathrm{C} = 0.10$. Below this limit, deformation is dominated by core-wall buckling and crushing and the front face strikes the back face due to core failure. A combination of core-wall buckling and load-spreading provides the highest blast mitigation. This combination is achieved when the core mass is $\sim 20\%$ of the total structural mass, as measured by $\overline{M}_\mathrm{C}$ and $\overline{M}_\mathrm{FF}$ in the analysis.

Deformation and energy dissipation are relatively less sensitive to front-face mass, as compared to core mass. However, an optimal design requires a balance between core and face sheet masses ($\overline{M}_\mathrm{C} = 0.20$, $\overline{M}_\mathrm{FF} > 0.20$). The back-face mass has negligible effect on overall blast resistance in the initial stages of deformation. However, thick back faces are significantly less susceptible to rupture and exhibit improved blast resistance. For impulses up to $\overline{I} = 0.5$, sandwich structures with $\overline{M}_\mathrm{FF} \sim 0.25$, $\overline{M}_\mathrm{C} \sim 0.20$ and $\overline{M}_\mathrm{BF} \sim 0.55$ provide the highest bending resistance. The results suggest that the role of support conditions is very important in designing sandwich plates resistant to underwater blasts. In particular, for heavy core structures, clamped boundary conditions lead to shear-dominated rupture which is highly dependent on support conditions.

The responses of structures under air-backed and water-backed conditions are significantly different. Deflections under water-backed conditions are $\sim 30\%$ of the deflections under air-backed conditions for $\overline{M}_\mathrm{C} < 0.20$ and $\sim 60\%$ for $\overline{M}_\mathrm{C} > 0.20$ at high impulse magnitudes. However, for both air-backed and water-backed conditions, structures with $\overline{M}_\mathrm{C} = 0.10$ show the lowest deflection, and, therefore, the highest bending resistance. Under the same loading conditions, the dissipation in water-backed structures is $\sim 20\%$ higher than the dissipation in air-backed structures.

The calculations have yielded quantitative structure-performance relations in terms of deflection, energy dissipation, and load transmission. These relations allow optimal or desirable structure attributes to be identified for prescribed loading conditions or performance targets. These relations can provide guidance for the design of blast-resistant metallic structures. Finally, it should be noted that the relations described in this paper are applicable only for the structural attributes and loading conditions considered.

6. Acknowledgement

References

[Battley and Allen 2012] M. Battley and T. Allen, "Servo-hydraulic system for controlled velocity water impact of marine sandwich panels", *Exp. Mech.* **52**:1 (2012), 95–106.

[Cole 1947] R. H. Cole, "Spherical shock waves from underwater explosions", *Phys. Rev.* **72**:2 (1947), 177.

[ConWep 2005] ConWep, "ConWep blast simulation software", 2005, https://pdc.usace.army.mil/software/conwep/.

[Côté et al. 2009] F. Côté, B. P. Russell, V. S. Deshpande, and N. A. Fleck, "The through-thickness compressive strength of a composite sandwich panel with a hierarchical square honeycomb sandwich core", *J. Appl. Mech.* (*ASME*) **76**:6 (2009), 061004.

[Deshpande and Fleck 2005] V. S. Deshpande and N. A. Fleck, "One-dimensional response of sandwich plates to underwater shock loading", *J. Mech. Phys. Solids* **53**:11 (2005), 2347–2383.

[Dharmasena et al. 2008] K. P. Dharmasena, H. N. G. Wadley, Z. Xue, and J. W. Hutchinson, "Mechanical response of metallic honeycomb sandwich panel structures to high-intensity dynamic loading", *Int. J. Impact Eng.* **35**:9 (2008), 1063–1074.

[Dharmasena et al. 2010] K. P. Dharmasena, D. T. Queheillalt, H. N. G. Wadley, P. Dudt, Y. Chen, D. Knight, A. G. Evans, and V. S. Deshpande, "Dynamic compression of metallic sandwich structures during planar impulsive loading in water", *Eur. J. Mech. A Solids* **29**:1 (2010), 56–67.

[Dharmasena et al. 2011] K. P. Dharmasena, H. N. G. Wadley, K. Williams, Z. Xue, and J. W. Hutchinson, "Response of metallic pyramidal lattice core sandwich panels to high intensity impulsive loading in air", *Int. J. Impact Eng.* **38**:5 (2011), 275–289.

[Espinosa et al. 2006] H. D. Espinosa, S. Lee, and N. Moldovan, "A novel fluid structure interaction experiment to investigate deformation of structural elements subjected to impulsive loading", *Exp. Mech.* **46**:6 (2006), 805–824.

[Hibbit et al. 2009] D. Hibbit, B. Karlsson, and P. Sorensen, *Abaqus/Explicit user's manual, version 6.9*, ABAQUS, Cambridge, 2009, http://abaqusdoc.ucalgary.ca/v6.9/.

[Hutchinson and Xue 2005] J. W. Hutchinson and Z. Xue, "Metal sandwich plates optimized for pressure impulses", *Int. J. Mech. Sci.* **47**:4–5 (2005), 545–569.

[Johnson and Cook 1985] G. R. Johnson and W. H. Cook, "Fracture characteristics of three metals subjected to various strains, strain rates, temperatures and pressures", *Eng. Fract. Mech.* **21**:1 (1985), 31–48.

[Kambouchev et al. 2007] N. Kambouchev, L. Noels, and R. Radovitzky, "Numerical simulation of the fluid–structure interaction between air blast waves and free-standing plates", *Comput. Struct.* **85**:11–14 (2007), 923–931.

[Latourte et al. 2012] F. Latourte, X. Wei, Z. D. Feinberg, A. de Vaucorbeil, P. Tran, G. B. Olson, and H. D. Espinosa, "Design and identification of high performance steel alloys for structures subjected to underwater impulsive loading", *Int. J. Solids Struct.* **49**:13 (2012), 1573–1587.

[Liang et al. 2005] Y. Liang, A. V. Spuskanyuk, S. E. Flores, D. R. Hayhurst, J. W. Hutchinson, R. M. McMeeking, and A. G. Evans, "The response of metallic sandwich panels to water blast", *J. Appl. Mech.* (*ASME*) **74**:1 (2005), 81–99.

[McShane et al. 2006] G. J. McShane, V. S. Deshpande, and N. A. Fleck, "The underwater blast resistance of metallic sandwich beams with prismatic lattice cores", *J. Appl. Mech.* (*ASME*) **74**:2 (2006), 352–364.

[McShane et al. 2008] G. J. McShane, C. Stewart, M. T. Aronson, H. N. G. Wadley, N. A. Fleck, and V. S. Deshpande, "Dynamic rupture of polymer–metal bilayer plates", *Int. J. Solids Struct.* **45**:16 (2008), 4407–4426.

[Mori et al. 2007] L. F. Mori, S. Lee, Z. Y. Xue, A. Vaziri, D. T. Queheillalt, K. P. Dharmasena, H. N. G. Wadley, J. W. Hutchinson, and H. D. Espinosa, "Deformation and fracture modes of sandwich structures subjected to underwater impulsive loads", *J. Mech. Mater. Struct.* **2**:10 (2007), 1981–2006.

[Nahshon et al. 2007] K. Nahshon, M. G. Pontin, A. G. Evans, J. W. Hutchinson, and F. W. Zok, "Dynamic shear rupture of steel plates", *J. Mech. Mater. Struct.* **2**:10 (2007), 2049–2066.

[Radford et al. 2006] D. D. Radford, G. J. McShane, V. S. Deshpande, and N. A. Fleck, "Dynamic compressive response of stainless-steel square honeycombs", *J. Appl. Mech. (ASME)* **74**:4 (2006), 658–667.

[Rathbun et al. 2006] H. J. Rathbun, D. D. Radford, Z. Xue, M. Y. He, J. Yang, V. Deshpande, N. A. Fleck, J. W. Hutchinson, F. W. Zok, and A. G. Evans, "Performance of metallic honeycomb-core sandwich beams under shock loading", *Int. J. Solids Struct.* **43**:6 (2006), 1746–1763.

[Spuskanyuk and McMeeking 2007] A. V. Spuskanyuk and R. M. McMeeking, "Sandwich panels for blast protection in water: Simulations", *Int. J. Mater. Res.* **98**:12 (2007), 1250–1255.

[Taylor 1963] G. I. Taylor, *Scientific papers, III: Aerodynamics and the mechanics of projectiles and explosions*, edited by G. K. Batchelor, Cambridge University Press, 1963.

[Vaziri and Xue 2007] A. Vaziri and Z. Xue, "Mechanical behavior and constitutive modeling of metal cores", *J. Mech. Mater. Struct.* **2**:9 (2007), 1743–1760.

[Vaziri et al. 2007] A. Vaziri, Z. Xue, and J. W. Hutchinson, "Performance and failure of metal sandwich plates subjected to shock loading", *J. Mech. Mater. Struct.* **2**:10 (2007), 1947–1963.

[Wadley et al. 2013] H. N. G. Wadley, T. Børvik, L. Olovsson, J. J. Wetzel, K. P. Dharmasena, O. S. Hopperstad, V. S. Deshpande, and J. W. Hutchinson, "Deformation and fracture of impulsively loaded sandwich panels", *J. Mech. Phys. Solids* **61**:2 (2013), 674–699.

[Wei et al. 2008] Z. Wei, V. S. Deshpande, A. G. Evans, K. P. Dharmasena, D. T. Queheillalt, H. N. G. Wadley, Y. V. Murty, R. K. Elzey, P. Dudt, Y. Chen, D. Knight, and K. Kiddy, "The resistance of metallic plates to localized impulse", *J. Mech. Phys. Solids* **56**:5 (2008), 2074–2091.

[Wicks and Hutchinson 2001] N. Wicks and J. W. Hutchinson, "Optimal truss plates", *Int. J. Solids Struct.* **38**:30–31 (2001), 5165–5183.

[Xue and Hutchinson 2004a] Z. Xue and J. W. Hutchinson, "A comparative study of impulse-resistant metal sandwich plates", *Int. J. Impact Eng.* **30**:10 (2004), 1283–1305.

[Xue and Hutchinson 2004b] Z. Xue and J. W. Hutchinson, "Constitutive model for quasi-static deformation of metallic sandwich cores", *Int. J. Numer. Methods Eng.* **61**:13 (2004), 2205–2238.

[Zok et al. 2003] F. W. Zok, H. J. Rathbun, Z. Wei, and A. G. Evans, "Design of metallic textile core sandwich panels", *Int. J. Solids Struct.* **40**:21 (2003), 5707–5722.

[Zok et al. 2005] F. W. Zok, H. Rathbun, M. He, E. Ferri, C. Mercer, R. M. McMeeking, and A. G. Evans, "Structural performance of metallic sandwich panels with square honeycomb cores", *Philos. Mag.* **85**:26–27 (2005), 3207–3234.

SIDDHARTH AVACHAT: sidavachat@gmail.com
The George W. Woodruff School of Mechanical Engineering, The School of Materials Science and Engineering, Georgia Institute of Technology, Atlanta, GA 30332-0405, United States

MIN ZHOU: min.zhou@gatech.edu
The George W. Woodruff School of Mechanical Engineering, The School of Materials Science and Engineering, Georgia Institute of Technology, Atlanta, GA 30332-0405, United States

■msp

■msp

THERMAL AND MAGNETIC EFFECTS ON THE VIBRATION
OF A CRACKED NANOBEAM EMBEDDED IN AN ELASTIC MEDIUM

DANILO KARLIČIĆ, DRAGAN JOVANOVIĆ, PREDRAG KOZIĆ AND MILAN CAJIĆ

In this study, we develop a model to describe the free vibration behavior of a cracked nanobeam embedded in an elastic medium by considering the effects of longitudinal magnetic field and temperature change. In order to take into account the small-scale and thermal effects, the Euler–Bernoulli beam theory based on the nonlocal elasticity constitutive relation is reformulated for one-dimensional nanoscale systems. In addition, the effect of a longitudinal magnetic field is introduced by considering the Lorenz magnetic force obtained from the classical Maxwell equation. To develop a model of a cracked nanobeam, we suppose that a nanobeam consists of two segments connected by a rotational spring that is located in the position of the cracked section. The surrounding elastic medium is represented by the Winkler-type elastic foundation. Influences of the nonlocal parameter, stiffness of rotational spring, temperature change and magnetic field on the system frequencies are investigated for two types of boundary conditions. Also, the first four mode shape functions for the considered boundary conditions are shown for various values of the crack position.

1. Introduction

Recently, there has been a growing interest among scientists to study the influence of various multiphysics phenomena on the vibration behavior of nanostructures such as nanorods [Murmu et al. 2014; Alper and Hamad-Schifferli 2010; Martín et al. 2012], nanobeams [Kiani 2012; Youssef and Elsibai 2011; Firouz-Abadi and Hosseinian 2012], nanoplates [Murmu et al. 2013; Arani et al. 2013; Kiani 2014a; A. Haghshenas and Arani 2013], etc. Often, such studies are related to the application of nanostructures in nanoelectromechanical systems (NEMS) [Batra et al. 2007; Popov et al. 2007]. Understanding the dynamic behavior of such systems is of prime importance in design procedures and the practical application of NEMS devices. Materials such as carbon, zinc-oxide, gold, silver and boron-nitride nanotubes [Xie et al. 2000; 2004; Wu et al. 2005; Yum and Yu 2006] and also graphene sheets [Gómez-Navarro et al. 2008; Schniepp et al. 2006; Niyogi et al. 2006] have superior mechanical, physical and thermal properties, which have lately become very important in nanoengineering practice. For the analysis of nanostructures, there are three basic approaches: experimental analysis [Meyer et al. 2007; Jensen 1999], molecular dynamic simulation [Park et al. 2005; Bershtein et al. 2002] and the continuum mechanics approach [Eringen 1972; 1983; Reddy and Pang 2008; Ansari et al. 2012; Jam et al. 2012]. Experimental studies of nanostructures are very important for determining their physical properties. However, direct measurement of properties is difficult due to very small dimensions of structures and weak control of

experimental parameters, which makes this approach very expensive. On the other hand, molecular dynamics is a highly developed method to simulate the dynamic behavior of nanostructures. However, this approach is applicable only to nanostructures with a small number of atoms and molecules whereas for large-sized nanoscale systems, such as nanocomposites and multiple nanostructure systems, it is time-consuming and computationally prohibitive. All this leads to the conclusion that continuum-based theories need to be considered. Since the mechanical behavior of nanostructures strongly depends on the size effects when the system is very small compared to the molecular distances, classical continuum theories need to be modified in order to consider small-scale effects. In the nonlocal theory of Eringen, small-scale effects are introduced into a constitutive equation via a single material parameter. The main assumption of this theory is that the stress at a point is a function of strains at all other points in the continuum body. According to Eringen [1972; 1983], the excellent approximation can be provided for a large class of multiphysics phenomena with internal length scale ranging from the atomistic to the macroscopic scale. Thus, using the classical continuum theory and ignoring the small-scale effects and atomic forces when analyzing the nanostructures may lead to inaccurate results and hence erroneous designs.

In recent years, a large number of researchers have investigated the influence of different physical effects on the dynamic behavior of one-dimensional nanostructures. Murmu and Pradhan [2009] investigated the influence of thermal and nonlocal effects on the free vibration of a single-walled carbon nanotube (CNT) embedded in an elastic medium. In [Murmu and Pradhan 2010], they also examined the stability of CNT in an elastic medium under the influence of temperature change. In both cases, they used nonlocal Euler–Bernoulli beam theory. Benzair et al. [2008] reformulated the classical Timoshenko beam theory by using the nonlocal elasticity. In addition, they introduced thermal effects through the constitutive relation for vibration analysis of CNT. In [Ke and Wang 2012], governing equations of motion were derived by using the Hamilton principle and nonlocal elasticity for thermoelectromechanical vibration of the piezoelectric nanobeams with various boundary conditions. In addition, they investigated the influence of the nonlocal parameter, temperature change, external electric voltage and axial force on the thermoelectromechanical vibration characteristics of the piezoelectric nanobeams. Hosseini-Hashemi et al. [2014] considered surface effects on the free vibration of piezoelectric functionally graded nanobeams by using the nonlocal elasticity theory. Further, they investigated the influences of the surface and nonlocal effects on the piezoelectric field and the static and dynamic behavior of the nanobeam. Kiani [2014b] investigated the influence of a three-dimensional magnetic field on the vibration and instability of a single-walled CNT. The equations of motion were obtained from the nonlocal Rayleigh beam theory and Maxwell equations. In addition, the author derived an expression for a critical transverse magnetic field associated with the lateral buckling of the single-walled CNT. Li et al. [2011] obtained coupled dynamic equations of multiwalled CNTs subjected to a transverse magnetic field by considering the Lorentz magnetic forces. In addition, they showed the influence of van der Waals force on the dynamic characteristics of multiwalled CNTs. Further, they examined the effects of the van der Waals forces on vibration characteristics of a multiwalled CNT under a transverse magnetic field, where the CNT was represented by a cylindrical shell. Wei and Wang [2004] investigated the wave propagation in a single-wall carbon nanotube for two different propagating modes, i.e., the transverse electric and transverse magnetic modes. Recently, Karličić et al. [2014] studied the influence of an axial magnetic field on vibration of multiple coupled viscoelastic CNTs embedded in a viscoelastic medium. The authors

determined complex and critical values of natural frequencies of the system and performed a detailed parametric study.

The study of the vibration behavior of cracked CNTs is of great theoretical and practical interest for better understanding of the mechanical response of nanostructures. Based on a growing number of experimental studies, it was found that the CNT is not a perfect nanostructure as it seems at the beginning of investigations. Different types of defects cause a local change in stiffness of CNTs that may have significant influence on natural frequencies and mode shapes. Moreover, researchers have considered two types of initial defects in carbon nanostructures. In *the first group are topological defects* related to bonds between atoms in an atomic network. This includes Stone–Wales defects [Zhou and Shi 2003; Charlier 2002] causing irregularities in the hexagonal network of carbon-carbon bonds in CNTs, which leads to a disturbance in local stiffness. In *the second group are point defects* related to creating single and multiple vacancies [Charlier 2002; Sammalkorpi et al. 2004; Belytschko et al. 2002] in the atomic network, which leads to degradation of mechanical characteristics of the crystal lattice. In this case, local change in stiffness of CNTs also occurs. From the standpoint of continuum mechanics, this change of local stiffness of CNT can be modeled as a change in the strain energy of a nanobeam. The flexural vibration behavior of a cracked nanobeam based on the nonlocal elasticity theory was investigated by Loya et al. [2009]. They proposed the model of a cracked nanobeam consisting of two segments connected by a rotational spring located at the cracked section. In addition, the authors showed the influence of crack severity, the nonlocal parameter and boundary conditions on natural frequencies of the cracked nanobeam. Torabi and Dastgerdi [2012] investigated the free vibration of a cracked nanobeam modeled via nonlocal elasticity and Timoshenko beam theory, where the cracked nanobeam is represented by two segments connected by a rotational spring. They analyzed the effects of crack position, ratio and the nonlocal parameter on the vibration mode and frequency parameter. The bending vibrations of a cracked nanobeam with surface effects were studied in [Hasheminejad et al. 2011]. In [Yang and Chen 2008], the free vibration and stability of the beam made of functionally graded materials containing an open crack were investigated by using Euler–Bernoulli beam theory and the rotational spring model at the cracked section. Roostai and Haghpanahi [2014] discussed the vibration behavior of a nanobeam with multiple cracks for various boundary conditions. They showed the influence of changing the number of cracks on dimensionless frequencies for change in boundary conditions.

As stated in [Yang and Chen 2008], models of cracked nanobeams can be divided into two groups: "continuous" models and "lumped flexibility" models. In this paper, we use the technique that belongs to the method of "lumped flexibility" models, whose main characteristic is that the presence of a crack is modeled via change of the stiffness of beams at the position of the crack, which is equivalent to the stiffness of an inserted spring. The main objective of this paper is to present an analytical model and analyze the vibrational behavior of a cracked nanobeam embedded in an elastic medium by taking into account the magnetic field and thermal effects. In addition, different boundary conditions of the cracked nanobeam are also considered. The governing equation of motion is derived by using the Euler–Bernoulli beam theory, nonlocal thermoelastic constitutive relation and Maxwell relation. The frequency equation is derived and numerically solved for different boundary conditions, and the obtained results are compared to the corresponding ones in the literature. In the parametric study, the effects of various physical parameters on natural frequencies and mode shape functions are also investigated.

2. Problem formulation

2.1. *Nonlocal constitutive relation.* In this subsection, we will provide the fundamental constitutive relation of the nonlocal elasticity and thermoelasticity theory. The basic form of the nonlocal elastic relation for a three-dimensional linear, homogeneous isotropic body is given as

$$\sigma_{ij}(x) = \int \alpha(|x - x'|, \tau) C_{ijkl} \epsilon_{kl}(x') \, dV(x') \quad \text{for all } x \in V, \tag{1a}$$

$$\sigma_{ij,j} = 0, \tag{1b}$$

$$\epsilon_{ij} = \tfrac{1}{2}(u_{i,j} + u_{j,i}), \tag{1c}$$

where C_{ijkl} is the elastic modulus tensor for classical isotropic elasticity; σ_{ij} and ϵ_{ij} are the stress and the strain tensors, respectively, and u_i is the displacement vector. With $\alpha(|x - x'|, \tau)$, we denote the nonlocal modulus or attenuation function, which incorporates nonlocal effects into the constitutive equation at a reference point x produced by the local strain at a source x'. The above absolute value of the difference $|x - x'|$ denotes the Euclidean metric. The parameter $\tau = (e_0 a)/l$, where l is the external characteristic length (crack length and wave length), a describes the internal characteristic length (lattice parameter, granular size and distance between C-C bonds) and e_0 is a constant appropriate to each material that can be identified from atomistic simulations or by using the dispersive curve of the Born–von Kármán model of lattice dynamics. Since it is difficult to use constitutive relations in the integral form for solving practical problems, simplified constitutive relations in the differential form were developed. Based [Eringen 1972; 1983], constitutive relations in the differential form for the one-dimensional case are

$$\sigma_{xx} - \mu \frac{d^2 \sigma_{xx}}{dx^2} = E \epsilon_{xx}, \tag{2a}$$

$$\sigma_{xz} - \mu \frac{d^2 \sigma_{xz}}{dx^2} = G \gamma_{xz}, \tag{2b}$$

where E and G are the elastic modulus and the shear modulus of the beam, respectively; $\mu = (e_0 a)^2$ is the nonlocal parameter (length scales); σ_{xx} and σ_{xz} are the normal and the shear nonlocal stresses, respectively, and $\epsilon_{xx} = u - z \frac{\partial^2 w}{\partial x^2}$ is the axial deformation. Nanomaterials such as CNTs, ZnO nanotubes and other one-dimensional structures are modeled as nanobeams and nanorods by using the nonlocal theory, where internal characteristic lengths $(e_0 a)$ are often assumed to be in the range 0–2 nm. When $e_0 a = 0$, the nonlocal constitutive relation is reduced to the classical constitutive relation of the elastic body. The nonlocal thermoelastic constitutive relation model proposed by Zhang et al. [2008] and Murmu and Pradhan [2009; 2010] is a combination of nonlocal elasticity and classical thermoelasticity theory. Therefore, for one-dimensional nonlocal viscoelastic solids, constitutive relations are given by

$$\sigma_{xx} - \mu \frac{d^2 \sigma_{xx}}{dx^2} = E \left(\epsilon_{xx} - \frac{\alpha_x \theta}{1 - 2\nu} \right), \tag{3}$$

where α_x is the coefficient of thermal expansion in the direction of the x axis, ν is the Poisson ratio and θ denotes the change in temperature. If $\theta = 0$, i.e., there is no influence of change in temperature, we then return to the constitutive relation for nonlocal elasticity. It should be noted that Young's modulus of some types of nanomaterials, for example CNT, is insensitive to temperature changes in the tube at

temperatures less than nearly $1100\,\mathrm{K}$, but it decreases at higher temperatures [Hsieh et al. 2006]. In what follows, we will use the constitutive relation for nonlocal thermoelasticity to derive governing equations of motion.

2.2. *Maxwell's relation.* According to the classical electromagnetic theory [Narendar et al. 2012], the Maxwell equations in differential form are given as

$$J = \nabla \times h, \qquad \nabla \times e = -\eta \frac{\partial h}{\partial t}, \qquad \nabla \cdot h = 0, \tag{4}$$

where J is the current density, h is the distributing vector of the magnetic field, e is the strength vector of the electric fields and η is the magnetic field permeability. In addition, we define the vectors for distributing magnetic field h and electric field e as

$$h = \nabla \times (U \times H), \qquad e = -\eta \left(\frac{\partial U}{\partial t} \times H \right), \tag{5}$$

in which $\nabla = \frac{\partial}{\partial x} i + \frac{\partial}{\partial y} j + \frac{\partial}{\partial z} k$ is the Hamilton operator, $U = (x, y, z)$ is the displacement vector and $H = (H_x, 0, 0)$ is the vector of the longitudinal magnetic field, and (i, j, k) are unit vectors. In the present study, we assume that the longitudinal magnetic field acts on the cracked nanobeam in the axial direction. Now, we can write the vector of the distributing magnetic field in the form

$$h = -H_x \left(\frac{\partial v}{\partial y} + \frac{\partial w}{\partial z} \right) i + H_x \frac{\partial v}{\partial x} j + H_x \frac{\partial w}{\partial x} k. \tag{6}$$

Then, we introduce (6) into the first expressions of (4):

$$J = \nabla \times h = H_x \left(-\frac{\partial^2 v}{\partial x\, \partial z} + \frac{\partial^2 w}{\partial x\, \partial y} \right) i - H_x \left(\frac{\partial^2 v}{\partial y\, \partial z} + \frac{\partial^2 w}{\partial x^2} + \frac{\partial^2 w}{\partial z^2} \right) j + H_x \left(\frac{\partial^2 v}{\partial x^2} + \frac{\partial^2 v}{\partial y^2} + \frac{\partial^2 w}{\partial z\, \partial y} \right) k. \tag{7}$$

Substituting (7) into the expressions for the Lorentz forces induced by the longitudinal magnetic field yields

$$f(f_x, f_y, f_z) = \eta(J \times H) = \eta \left[0i + H_x^2 \left(\frac{\partial^2 v}{\partial x^2} + \frac{\partial^2 v}{\partial y^2} + \frac{\partial^2 w}{\partial z\, \partial y} \right) j + H_x^2 \left(\frac{\partial^2 w}{\partial x^2} + \frac{\partial^2 w}{\partial y^2} + \frac{\partial^2 v}{\partial z\, \partial y} \right) k \right], \tag{8}$$

where f_x, f_y and f_z express the Lorentz force along the x, y and z directions as

$$f_x = 0, \tag{9a}$$

$$f_y = \eta H_x^2 \left(\frac{\partial^2 v}{\partial x^2} + \frac{\partial^2 v}{\partial y^2} + \frac{\partial^2 w}{\partial z\, \partial y} \right), \tag{9b}$$

$$f_z = \eta H_x^2 \left(\frac{\partial^2 w}{\partial x^2} + \frac{\partial^2 w}{\partial y^2} + \frac{\partial^2 v}{\partial z\, \partial y} \right). \tag{9c}$$

In this study, we assume that the displacement of nanobeam $w(x, t)$ and the Lorentz force act only in the z direction, which can be written as

$$f_z = \eta H_x^2 \frac{\partial^2 w}{\partial x^2}. \tag{10}$$

Finally, it is possible to obtain force per unit length of the nanobeam in the form

$$\tilde{q}(x,t) = \int_A f_z \, dA = \eta A H_x^2 \frac{\partial^2 w}{\partial x^2}. \tag{11}$$

2.3. *Mathematical model of a cracked nanobeam.* Zhang et al. [2005] have introduced one type of vacancy defect in CNTs known as a slit defect. Under certain assumptions, the slit defect, resulting from removing C-C atom pairs in the circumferential direction of the regular lattice of CNTs, can be observed as cracks (Figure 1a). Thus, we consider SWCNT with a slit defect, which is embedded in an elastic medium, as a cracked nanobeam by using the nonlocal continuum model with two types of boundary conditions as shown in Figure 1b–d. The cracked nanobeam is represented by two beam segments connected with a rotational spring of stiffness c, where the left segment is before the crack section and the right segment is after the crack section. Both nanobeam segments have the same material properties: Young's modulus E, mass density ρ, cross-section area A, moment of inertia I and the nonlocal parameter μ. Moreover, the nanobeam is under the influence of Lorentz magnetic force induced by the longitudinal magnetic field. These parameters are assumed to be constant along the nanobeam. The nanobeam is considered to be of length L with crack-position L^*. The transversal displacements over the two defined segments of the nanobeam are denoted by $w_1(x,t)$ and $w_2(x,t)$, i.e., the left segment and the right segment, respectively. The nanobeam model is described by using the nonlocal Euler–Bernoulli beam theory, where the effect of the temperature change is introduced through the constitutive relation. The elastic medium is modeled by a Winkler-type elastic foundation, which is represented by
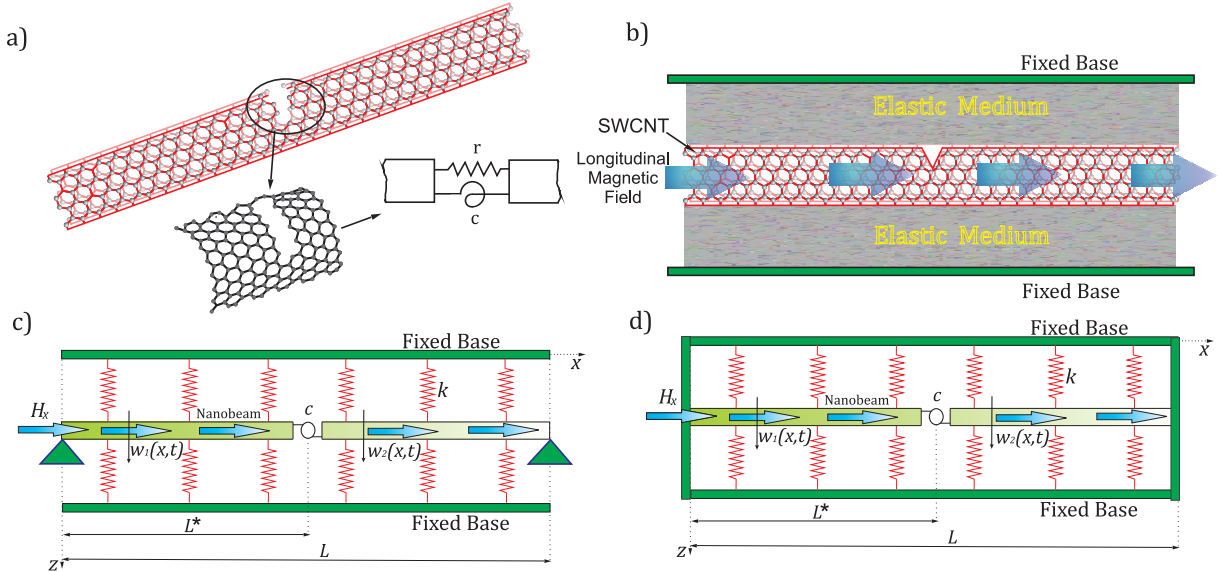
Figure 1. (a) SWCNT with defects. (b) Axial magnetic field exerted on the cracked SWCNT embedded in an elastic medium, physical model; equivalent nonlocal mechanical model of the cracked nanobeam coupled with the Winkler elastic foundation in the axial magnetic field for various boundary conditions. (c) Simply supported. (d) Clamped-clamped.

continuously distributed springs of stiffness k. In the present study, two types of boundary conditions are considered: simply supported (Figure 1c) and clamped-clamped (Figure 1d).

According to Newton's second law, the equilibrium equations for the differential element of the nanobeam can be expressed in the similar manner as in [Kozić et al. 2014], which gives

$$\frac{\partial F_T}{\partial x} - kw + \tilde{q} + N\frac{\partial^2 w}{\partial x^2} = \rho A\frac{\partial^2 w}{\partial t^2}, \tag{12a}$$

$$\frac{\partial N}{\partial x} = \rho A\frac{\partial^2 u}{\partial t^2}, \tag{12b}$$

$$F_T = \frac{\partial M_f}{\partial x}, \tag{12c}$$

where u is the axial displacement and M_f and N are the moment and axial force stress resultants, respectively, defined as

$$M_f = \int_0^A z\sigma_{xx}\, dA, \tag{13a}$$

$$N = \int_0^A \sigma_{xx}\, dA, \tag{13b}$$

where $\tilde{q}$ is the magnetic force per unit length defined in (11).

By using the nonlocal constitutive relation from (3) with expressions (12) and (13) and assuming that the axial displacement u is zero, we can get the equations

$$M_f = \mu\left[kw - \tilde{q} - N\frac{\partial^2 w}{\partial x^2} + \rho A\frac{\partial^2 w}{\partial t^2}\right] - EI\frac{\partial^2 w}{\partial x^2}, \quad i = 1, 2, \tag{14a}$$

$$N = -EA\frac{\alpha_x\theta}{1 - 2\nu}. \tag{14b}$$

The equation of motion of the nanobeam in terms of transversal displacements $w(x, t)$ is obtained by introducing (14a), (14b) and (12c) into (12a) in the form

$$\rho A\frac{\partial^2 w}{\partial t^2} + kw - \eta AH_x^2\frac{\partial^2 w}{\partial x^2} + EA\frac{\alpha_x\theta}{1 - 2\nu}\frac{\partial^2 w}{\partial x^2} + EI\frac{\partial^4 w}{\partial x^4}$$
$$= \mu\frac{\partial^2}{\partial x^2}\left[\rho A\frac{\partial^2 w}{\partial t^2} + kw - \eta AH_x^2\frac{\partial^2 w}{\partial x^2} + EA\frac{\alpha_x\theta}{1 - 2\nu}\frac{\partial^2 w}{\partial x^2}\right] \tag{15}$$

or in the dimensionless form

$$\frac{\partial^2\overline{w}}{\partial\tau^2} + K\overline{w} + (\overline{N}_\theta - \mathrm{MP})\frac{\partial^2\overline{w}}{\partial\xi^2} + \frac{\partial^4\overline{w}}{\partial\xi^4} = \nu^2\frac{\partial^2}{\partial\xi^2}\left[\frac{\partial^2\overline{w}}{\partial\tau^2} + K\overline{w} + (\overline{N}_\theta - \mathrm{MP})\frac{\partial^2\overline{w}}{\partial\xi^2}\right], \tag{16a}$$

where

$$\overline{w} = \frac{w}{L}, \qquad \xi = \frac{x}{L}, \qquad K = k\frac{L^4}{EI}, \qquad \mathrm{MP} = \frac{\eta AH_x^2}{EI}L^2,$$
$$\nu^2 = \frac{\mu}{L^2}, \qquad \tau = \frac{t}{L^2}\sqrt{\frac{EI}{\rho A}}, \qquad \overline{N}_\theta = EA\frac{\alpha_x\theta}{1 - 2\nu}\frac{L^2}{EI}. \tag{16b}$$

K, MP, $\bar{N}_\theta$ and ν are the dimensionless spring coefficient, magnetic parameter, thermal axial force and nonlocal parameter, respectively.

Now, we can solve the equation of motion (16a) by assuming the solution is in the form

$$\overline{w}(\xi, \tau) = \sum_{n=1}^{\infty} W_n(\xi) e^{i\Omega_n \tau}, \quad n = 1, 2, 3, \ldots, \tag{17}$$

where $i = \sqrt{-1}$, W_n are the mode functions and Ω_n are the dimensionless natural frequencies for n vibration modes. Introducing the assumed solutions (17) into (16a), we obtain the ordinary differential equation

$$W_n^{\mathrm{IV}}(\xi) + \tilde{b} W_n^{\mathrm{II}}(\xi) - \tilde{c} W_n(\xi) = 0, \tag{18}$$

where $(\cdot)^{\mathrm{I}}$ represents the derivative with respect to ξ and $\tilde{a}$, $\tilde{b}$ and $\tilde{c}$ are constants defined by

$$\tilde{a} = 1 - \nu^2(\bar{N}_\theta - \mathrm{MP}), \tag{19a}$$

$$\tilde{b} = \frac{\bar{N}_\theta - \mathrm{MP}}{\tilde{a}} + \nu^2\left(\lambda_n^4 - \frac{K}{\tilde{a}}\right), \tag{19b}$$

$$\tilde{c} = \left(\lambda_n^4 - \frac{K}{\tilde{a}}\right), \tag{19c}$$

$$\lambda_n^4 = \frac{\Omega_n^2}{\tilde{a}}. \tag{19d}$$

Introducing the assumed solutions $W_n(\xi) = \boldsymbol{D} e^{s\xi}$ into (18), we obtain a characteristic equation

$$s^4 + \tilde{b} s^2 - \tilde{c} = 0, \tag{20}$$

where the solutions are given as

$$s_{n1/2} = \pm\sqrt{\frac{-\tilde{b} + \sqrt{\tilde{b}^2 + 4\tilde{c}}}{2}} = \pm\alpha_n, \tag{21a}$$

$$s_{n3/4} = \pm\sqrt{\frac{-\tilde{b} - \sqrt{\tilde{b}^2 + 4\tilde{c}}}{2}} = \pm i\beta_n. \tag{21b}$$

Finally, the general solution of spatial differential equation (18) is written as

$$W_n(\xi) = D_{n1} \sinh(\alpha_n \xi) + D_{n2} \cosh(\alpha_n \xi) + D_{n3} \sin(\beta_n \xi) + D_{n4} \cos(\beta_n \xi), \tag{22}$$

where D_{ni}, $i = 1, 2, 3, 4$, are the unknown constants that are determined from the boundary conditions of the nanobeam.

Now, we consider the case of the nanobeam with a crack, which is located at the distance L^* from the left support, where the term $b = L^*/L$ denotes the dimensionless variable (Figure 1c–d). According to the methodology developed in [Loya et al. 2009; 2006; Fernández-Sáez et al. 1999; Fernández-Sáez and Navarro 2002; Torabi and Dastgerdi 2012], we modeled a cracked nanobeam with two beam segments connected by one linear and one rotational spring positioned at the site of a crack. In this model, we assume that both springs provide additional strain energy in the system caused by the presence of a crack.

Therefore, we obtain total strain energy as the sum of deformation energy of the nanobeam and additional strain energy from the springs in the form

$$U = \frac{1}{2} \int_V (\sigma_{xx} \cdot \epsilon_{xx}) \, dV + \Delta U_c|_{x=L^*}, \tag{23}$$

where σ_{xx} is the stress given by the expression (3), ϵ_{xx} is the axial deformation and ΔU_c is the increment of strain energy. The total strain energy (23) can be written in the expansion form by using (13) as

$$U = \frac{1}{2} \int_V \left(N \frac{\partial u}{\partial x} - M_f \frac{\partial^2 w}{\partial x^2} \right) dV + \left(\tfrac{1}{2} N \Delta u + \tfrac{1}{2} M_f \Delta \theta \right)\big|_{x=L^*}, \tag{24}$$

in which the term $(\tfrac{1}{2} N \Delta u)|_{x=L^*}$ represents the strain energy from a linear spring and $(\tfrac{1}{2} M_f \Delta \theta)|_{x=L^*}$ represents the strain energy from a rotational spring. The relative axial displacement Δu of a linear spring and rotation angle $\Delta \theta$ of the rotational spring, i.e., horizontal displacement and rotation of the edge crack section, are defined as

$$\Delta u = r \frac{\partial u}{\partial x} + k_{NM} \frac{\partial^2 w}{\partial x^2}, \tag{25a}$$

$$\Delta \theta = c \frac{\partial^2 w}{\partial x^2} + k_{MN} \frac{\partial u}{\partial x}, \tag{25b}$$

where r, c, k_{NM} and k_{MN} are the flexibility constants. It should be noted that the constants k_{NM} and k_{MN} represent coupling effects between the axial force and bending moment. In this paper, we analyzed only the free transversal vibrations where the axial displacement is neglected ($u(x, t) = 0$). Because of that, the flexibility constants k_{NM} and k_{MN} are assumed to be small compared to constants c and they are neglected as well [Torabi and Dastgerdi 2012]. Introducing these assumptions into the expression (25), we obtain the axial displacement Δu, angle of rotation $\Delta \theta$ (slope) and increment of the strain energy as

$$\Delta u = 0, \qquad \Delta \theta = c \frac{\partial^2 w}{\partial x^2} = C \frac{\partial^2 \overline{w}}{\partial \xi^2}, \qquad \Delta U_c|_{x=L^*} = \left(\tfrac{1}{2} M_f \Delta \theta \right)\big|_{x=L^*}, \tag{26}$$

where $C = c/L$ is the crack severity or dimensionless flexibility constant [Loya et al. 2009; Torabi and Dastgerdi 2012; Hasheminejad et al. 2011]. In general, flexibility constant C is the function of crack depth and geometry of the cracked section and nanobeam. However, in this analysis, we consider the flexibility constant C as a dimensionless parameter, but its value needs to be determined from the molecular dynamics model [Torabi and Dastgerdi 2012; Kisa and Gurel 2006; Loya et al. 2014]. In addition, it should be emphasized that increment of the strain energy ΔU_c in a cracked nanobeam or other nanostructure could be also determined by using the molecular dynamics model. In this study, values of crack severity are adopted based on the works found in the literature and the main attention is devoted to the investigation of their influence on dynamical behavior of a cracked nanobeam model subjected to the longitudinal magnetic field and temperature change.

Since the cracked nanobeam is modeled as a system of two nanobeams connected in series by a rotational spring, from (16) and (18), we can write the equations for each part of the nanobeam as

$$W_{n1}^{\mathrm{IV}}(\xi) + \tilde{b} W_{n1}^{\mathrm{II}}(\xi) - \tilde{c} W_{n1}(\xi) = 0, \quad 0 \le \xi \le b, \tag{27a}$$

$$W_{n2}^{\mathrm{IV}}(\xi) + \tilde{b} W_{n2}^{\mathrm{II}}(\xi) - \tilde{c} W_{n2}(\xi) = 0, \quad b \le \xi \le 1, \tag{27b}$$

where the influence of the crack is given via internal boundary conditions of the system. For such a system of equations, we can write the solution in the form

$$W_{n1}(\xi) = D_{n1} \sinh(\alpha_n \xi) + D_{n2} \cosh(\alpha_n \xi) + D_{n3} \sin(\beta_n \xi) + D_{n4} \cos(\beta_n \xi), \tag{28a}$$

$$W_{n2}(\xi) = D_{n5} \sinh(\alpha_n \xi) + D_{n6} \cosh(\alpha_n \xi) + D_{n7} \sin(\beta_n \xi) + D_{n8} \cos(\beta_n \xi), \tag{28b}$$

where unknown constants D_{ni}, $i = 1, 2, \ldots, 8$, are determined from boundary conditions of the system of nanobeams. In this paper, we consider two types of boundary conditions as shown in Figure 1c–d. They can be mathematically expressed as:

(a) for simply supported boundary conditions (Figure 1c), at $\xi = 0$,

$$\overline{w}_1(0, \tau) = 0 \implies W_{1n}(0) = 0, \tag{29a}$$

$$\overline{M}_{1f}|_{\xi=0} = \left[-\nu^2 \left(\lambda_n^4 - \frac{K}{\tilde{a}} \right) \tilde{a} W_{1n} - \tilde{a} W_{1n}^{\mathrm{II}} \right]_{\xi=0} = 0 \tag{29b}$$

and, at $\xi = 1$,

$$\overline{w}_2(1, \tau) = 0 \implies W_{2n}(1) = 0, \tag{30a}$$

$$\overline{M}_{2f}|_{\xi=1} = \left[-\nu^2 \left(\lambda_n^4 - \frac{K}{\tilde{a}} \right) \tilde{a} W_{2n} - \tilde{a} W_{2n}^{\mathrm{II}} \right]_{\xi=1} = 0, \tag{30b}$$

(b) for clamped-clamped boundary conditions (Figure 1d), at $\xi = 0$,

$$\overline{w}_1(0, \tau) = 0 \implies W_{1n}(0) = 0, \tag{31a}$$

$$\frac{\partial \overline{w}_1(0, \tau)}{\partial \xi} = 0 \implies W_{1n}^{\mathrm{I}}(0) = 0 \tag{31b}$$

and, at $\xi = 1$,

$$\overline{w}_2(1, \tau) = 0 \implies W_{2n}(1) = 0, \tag{32a}$$

$$\frac{\partial \overline{w}_2(1, \tau)}{\partial \xi} = 0 \implies W_{2n}^{\mathrm{I}}(1) = 0. \tag{32b}$$

For the crack section ($\xi = b$), we have compatibility conditions that are expressed as

- transversal displacement

$$\overline{w}_2(b, \tau) = \overline{w}_1(b, \tau) \implies W_{2n}(b) = W_{1n}(b), \tag{33a}$$

- bending slope

$$\frac{\partial \overline{w}_2(b, \tau)}{\partial \xi} - \frac{\partial \overline{w}_1(b, \tau)}{\partial \xi} = \Delta\theta \implies W_{2n}^{\mathrm{I}}(b) - W_{1n}^{\mathrm{I}}(b) = C W_{1n}^{\mathrm{II}}(b), \tag{33b}$$

- bending moment

$$\overline{M}_{1f}|_{\xi=b} = \overline{M}_{2f}|_{\xi=b}$$

$$\Rightarrow \left[-v^2 \left(\lambda_n^4 - \frac{K}{\tilde{a}} \right) \tilde{a} W_{2n} - \tilde{a} W_{2n}^{II} \right]_{\xi=b} = \left[-v^2 \left(\lambda_n^4 - \frac{K}{\tilde{a}} \right) \tilde{a} W_{1n} - \tilde{a} W_{1n}^{II} \right]_{\xi=b}, \quad (34a)$$

- transversal force

$$\overline{F}_{1T}|_{\xi=b} = \overline{F}_{2T}|_{\xi=b}$$

$$\Rightarrow \left[-v^2 \left(\lambda_n^4 - \frac{K}{\tilde{a}} \right) \tilde{a} W_{2n}^{I} - \tilde{a} W_{2n}^{III} \right]_{\xi=b} = \left[-v^2 \left(\lambda_n^4 - \frac{K}{\tilde{a}} \right) \tilde{a} W_{1n}^{I} - \tilde{a} W_{1n}^{III} \right]_{\xi=b}, \quad (34b)$$

where $C = c/L$ denotes the dimensionless stiffness parameter of rotational springs.

Introducing (28) into (29)–(30) and (33)–(34), we obtain a matrix equation consisting of eight homogeneous algebraic equations for simply supported boundary conditions in the form

$$[G(\lambda_n)]\{\psi\} = \{0\}, \quad (35)$$

where $[G(\lambda_n)]$ is the matrix of natural frequency parameters λ_n and the term $\{\psi\}$ is the vector composed of eight unknown constants D_{ni}, $i = 1, 2, \ldots, 8$. The nontrivial solution of the system (35) is obtained when the determinant of the system is equal to zero:

$$\det[G(\lambda_n)] = |G(\lambda_n)| = 0. \quad (36)$$

Solving these transcendent equations, we get the value of natural frequency and mode shape functions of the system for simply supported boundary conditions. Using the same methodology as in the previous case, substituting (28) into (31)–(32) and (33)–(34), we can obtain the frequency determinate for clamped-clamped boundary conditions in the form

$$|H(\lambda_n)| = 0. \quad (37)$$

The frequency determinants of the embedded nanotube for simply supported $|G(\lambda_n)|$ and clamped-clamped $|H(\lambda_n)|$ boundary conditions are given in the Appendix.

3. Numerical results and discussion

In order to perform a parametric study, we consider the following ranges of the dimensionless parameters: crack position $b = 0.25$–0.5, nonlocal parameter $v = 0$–0.6, crack severity $C = 0$–2 and stiffness of surrounding medium $K = 0$–1. These material and geometric parameters are adopted from [Loya et al. 2009]. In Tables 1 and 2, values of dimensionless natural frequencies of the cracked nanobeam are given for changes of nonlocal parameter v, crack severity C and stiffness of surrounding medium K for various values of crack position b. Results for the simply supported boundary conditions are given in Table 1 while those for the clamped-clamped boundary conditions are shown in Table 2. By comparing the results obtained in this study with the results found in [Loya et al. 2009], it can be noticed that an excellent agreement is achieved for both cases of boundary conditions. Further, the influence of crack position on mode shape functions is presented in Figure 2. In addition, the effects of a longitudinal magnetic field and change in temperature on natural frequencies are shown in Figures 3 and 4.

		$b = 0.5$				$b = 0.25$			
K	v	$C = 0$	$C = 0.5$	$C = 1$	$C = 2$	$C = 0$	$C = 0.5$	$C = 1$	$C = 2$
0	0	3.14159	2.63931	2.38319	2.09598	3.14159	2.82690	2.61743	2.34925
	0.2	2.89083	2.41902	2.17779	1.90983	2.89083	2.58446	2.37535	2.11337
	0.4	2.47903	2.06456	1.85242	1.61949	2.47903	2.19762	2.00246	1.76604
	0.6	2.15067	1.78664	1.60037	1.39708	2.15067	1.89756	1.72163	1.51254
0.5	0	3.14562	2.64609	2.39237	2.10943	3.14562	2.83242	2.62438	2.35883
	0.2	2.89599	2.42780	2.18979	1.92753	2.89599	2.59167	2.38463	2.12649
	0.4	2.48719	2.07862	1.87178	1.64815	2.48719	2.20930	2.01785	1.78830
	0.6	2.16313	1.80817	1.63003	1.44082	2.16313	1.91560	1.74562	1.54743
1	0	3.14962	2.65281	2.40145	2.12262	3.14962	2.83790	2.63127	2.36830
	0.2	2.90113	2.43649	2.20160	1.94475	2.90113	2.59882	2.39379	2.13937
	0.4	2.49528	2.09240	1.89055	1.67539	2.49528	2.22080	2.03289	1.80977
	0.6	2.17537	1.82895	1.65816	1.48091	2.17537	1.93314	1.76866	1.58012

Table 1. Values of the dimensionless natural frequency λ_n for the simply supported cracked nanobeam with different nonlocal parameter v, crack severity C, stiffness of surrounding medium K and crack position b. (Compare to [Loya et al. 2009] especially for $K = 0$.)

From Table 1, it can be noticed that an increase in crack severity decreases the natural frequency parameter of the cracked nanobeam. Moreover, it can be observed that an increase in the nonlocal parameter causes a decrease in the natural frequency as expected. This implies that the small-scale effect reduces the rigidity of the system so that the nanobeam becomes "softer". An increase in the stiffness coefficients has very weak influence on natural frequency of the system, and it causes a slight increase

		$b = 0.5$				$b = 0.25$			
K	v	$C = 0$	$C = 0.5$	$C = 1$	$C = 2$	$C = 0$	$C = 0.5$	$C = 1$	$C = 2$
0	0	4.73004	4.27235	4.10790	3.97023	4.73004	4.71675	4.71144	4.70681
	0.2	4.27661	3.79523	3.62032	3.47640	4.27661	4.26860	4.26418	4.25949
	0.4	3.59232	3.12694	2.96127	2.82852	3.59232	3.58948	3.58662	3.58104
	0.6	3.08370	2.66026	2.51211	2.39485	3.08370	3.08271	3.08094	3.06902
0.5	0	4.73122	4.27395	4.10970	3.97222	4.73122	4.71794	4.71263	4.70801
	0.2	4.27821	3.79751	3.62295	3.47937	4.27821	4.27021	4.26580	4.26110
	0.4	3.59501	3.13102	2.96607	2.83403	3.59501	3.59218	3.58932	3.58376
	0.6	3.08795	2.66688	2.51995	2.40390	3.08795	3.08697	3.08521	3.07334
1	0	4.73240	4.27555	4.11150	3.97422	4.73240	4.71913	4.71383	4.70920
	0.2	4.27981	3.79979	3.62558	3.48233	4.27981	4.27181	4.26740	4.26272
	0.4	3.59770	3.13509	2.97085	2.83950	3.5977	3.59488	3.59202	3.58647
	0.6	3.09219	2.67344	2.52773	2.41285	3.09219	3.09121	3.08946	3.07764

Table 2. Values of the dimensionless natural frequency λ_n for the clamped-clamped cracked nanobeam with different nonlocal parameter v, crack severity C, stiffness of surrounding medium K and crack position b. (Compare to [Loya et al. 2009] especially for $K = 0$.)
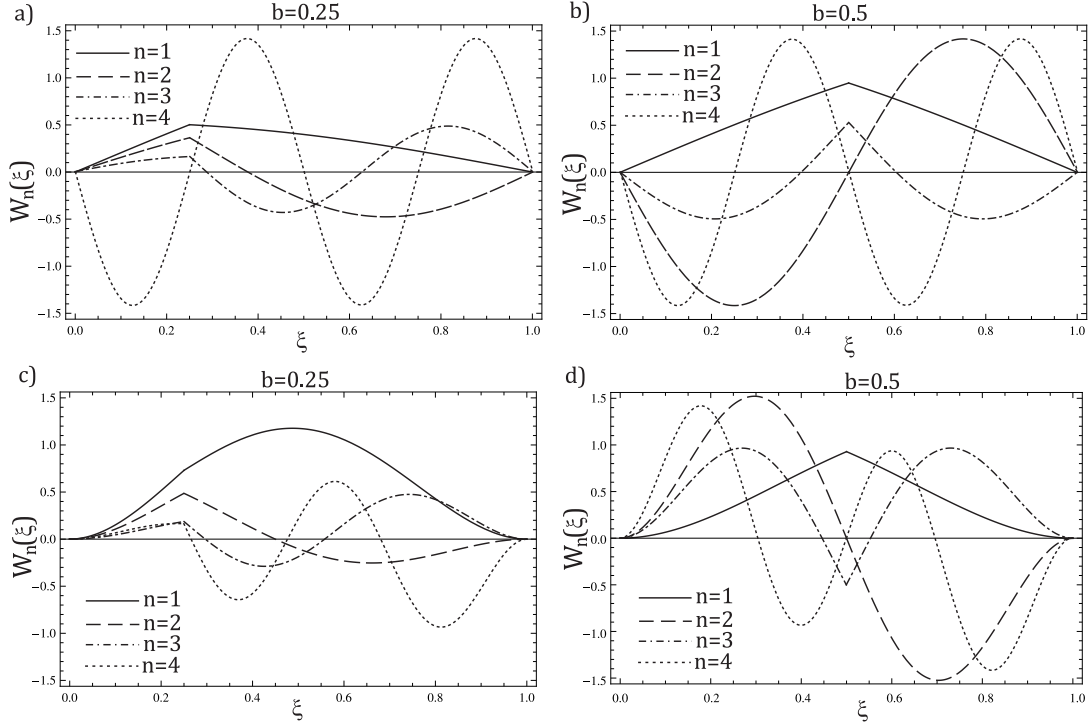
Figure 2. First four mode shapes of the simply supported nanobeam with (a) $b = 0.25$ and (b) $b = 0.5$ and of the clamped-clamped nanobeam with (c) $b = 0.25$ and (d) $b = 0.5$.

in the frequency as shown in Table 1. Also, it should be noted that when the crack severity is equal to zero we obtain natural frequencies of the embedded nanobeam without a crack. Comparing the natural frequencies from Table 1 for different crack positions, we can observe that, for a movement of crack position from the symmetric position at the middle of the nanobeam towards the boundaries, the natural frequency of the system decreases. This implies that the crack position has small influence on natural frequency when the crack is closer to the nanobeam boundaries.

In the case of clamped-clamped boundary conditions, we obtained higher values of natural frequencies due to the "stronger" constraints as shown in Table 2. Here, effects similar to those for the previous boundary conditions can be observed. An increase in crack severity as well as an increase in the nonlocal parameter causes a decrease in natural frequency while an increase in the medium's stiffness causes a slight increase in natural frequency. The $C = 0$ columns in Table 2 show natural frequencies of the clamped-clamped nanobeam without a crack. Considering the different crack positions in Table 2, we find that the natural frequency is higher for the case when the crack is closer to the boundaries while it decreases as the crack moves to the middle of the nanobeam.

It should be noted that the values of natural frequencies in this case reduce towards the values obtained in [Loya et al. 2009] when the longitudinal magnetic field, temperature change and stiffness of the elastic medium are equal to zero.

Mode shape functions of the cracked nanobeam for the first four vibration modes and two different boundary conditions and crack positions $b = 0.5$ and $b = 0.25$ are shown in Figure 2. For a simply
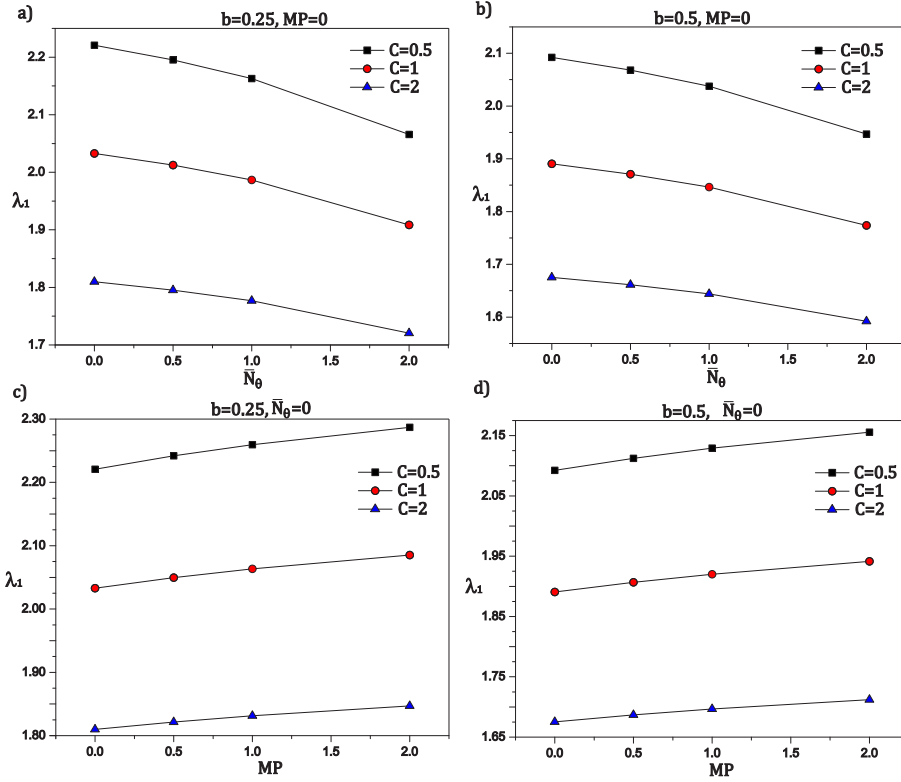
Figure 3. The first-mode natural frequency for a simply supported nanobeam with two crack positions.

supported nanobeam, in Figure 2a–b, we can observe that the differences of mode shape curves are localized near the crack position. When the crack is located at the middle of the nanobeam, we can notice the difference between symmetric and antisymmetric modes; i.e., differences of mode shape curves are visible only in the first and the third vibration mode and not for the second and the fourth mode. This is the case because the crack is located at the vibrational node, which is dependent on the mode number. It can be concluded that the crack does not affect the mode shape curve of the fourth vibration mode when the crack is located at a quarter of the length of the nanobeam (Figure 2a) and the second and fourth vibration modes when the crack is at the middle of the nanobeam (Figure 2b). In the next case, we analyze the clamped-clamped nanobeam in which a crack is located at $b = 0.25$ as shown in Figure 2c and at $b = 0.5$ in Figure 2d. As in the previous case, the crack causes changes in the mode shape functions. Also, it can be observed that deviations of mode shape curves allow us to detect surface defects in nanobeams and their control in the propagation.

Further, we examine the influence of thermal and magnetic field effects on the dimensionless natural frequency parameter of the cracked nanobeam embedded in an elastic medium. The following ranges of the dimensionless material and geometrical parameters of the cracked nanobeam are adopted: crack position $b = 0.25$–0.5, nonlocal parameter $\nu = 0.4$, crack severity $C = 0.5$–2, stiffness of surrounding medium $K = 1$, magnetic field parameter MP $= 0$–2 and thermal parameter $\overline{N}_\theta = 0$–2. In Figure 3, we
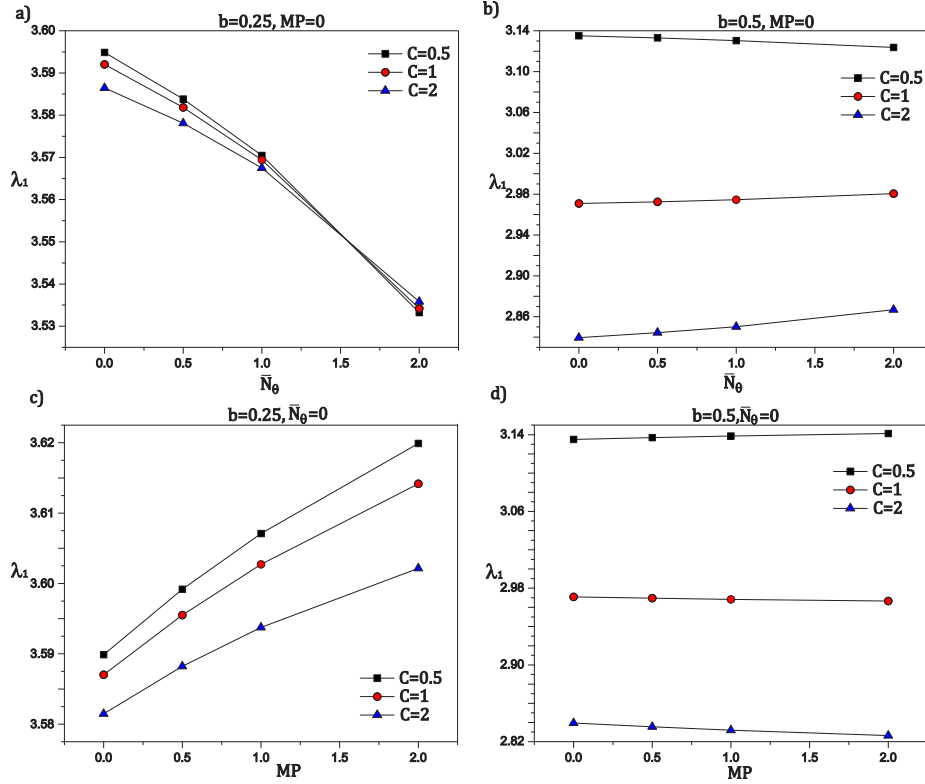
Figure 4. First natural frequency parameter for a clamped-clamped nanobeam with two crack positions.

plot the changes in the natural frequency parameter for different crack positions and simply supported boundary condition for two cases. In the first case, we consider the influence of thermal effect on the natural frequency parameter for MP = 0 (Figure 3a–b). Here, we can observe that an increase in the thermal coefficient causes a decrease in the natural frequency parameter for all values of crack severity and positions. This implies that the influence of thermal effect reduces the stiffness of the embedded nanobeam. From a physical point of view, the thermal parameter has damping effects on the vibration behavior of the cracked nanobeam. In the second case, we consider only the effect of the longitudinal magnetic field parameter on natural frequency as shown in Figure 3c–d. We can notice that an increase in the magnetic field parameter causes an increase in natural frequency for both cases of crack position in the nanobeam. Since an increase in the magnetic field parameter increases the rigidity of the system, it consequently increases the natural frequency parameter as well.

For further analysis of nonlocal vibration behavior of the cracked nanobeam embedded in an elastic medium, we will consider the systems with different crack positions and clamped-clamped boundary conditions. In addition, we adopt the same geometric and material parameters for the cracked nanobeam as in the previous case. Figure 4 shows changes in the natural frequency parameter for the clamped-clamped boundary condition case. It can be observed that for the crack position $b = 0.25$ there is no significant difference between natural frequencies with different crack severities. Further, it can be

noticed that an increase in the thermal coefficient causes a decrease in natural frequency for all cases. However, it can be noticed that the influence of crack stiffness is much smaller than in the case of the simply supported nanobeam. In addition, Figure 4b shows that for $b = 0.5$ the natural frequency slightly decreases for an increase in the thermal coefficient at the lowest value of crack severity but it slightly increases for an increase in the thermal coefficient when crack severities are higher. Figure 4c shows that for the crack position $b = 0.25$ natural frequencies are increasing for an increase in the magnetic field parameter in all cases. However, this is not the case when $b = 0.5$ as shown in Figure 4d. Here, it can be observed that the natural frequency slightly decreases for an increase of the magnetic field parameter at the lowest value of crack severity. However, it does not change for $C = 1$, and it slightly decreases for an increase in magnetic field parameter when $C = 2$. Finally, it should be noted that the system has a behavior similar to that of the case of the simply supported nanobeam for increased crack severity.

Analyzing the influence of external field parameters on the dynamic behavior of the cracked nanobeam structure, the following conclusion can be drawn. In the proposed model, the possibility of changing the natural frequency by variation of only external field parameters such as thermal and longitudinal magnetic field has a practical importance in design of NEMS devices. Choosing the proper magnitude of the external magnetic field in a certain range, it is possible to avoid the resonance state and increase the vibration amplitude at a given temperature. Moreover, this possibility allows us to control the crack propagation in a dynamic state of a nanostructure by controlling the total stiffness of a system. This study can be used as a starting point for the future investigation of vibration behavior of coupled nanobeams with cracks or in design procedures of nanodevices under the influence of various physical effects.

Conclusion

The main objective of this paper was to examine the influences of a magnetic field and thermal effects on the free vibration behavior of a cracked nanobeam. It can be concluded that natural frequency parameters of nanobeams are strongly influenced by the crack existence in the nanostructure. Various positions of the crack, different crack severities and different boundary conditions can change the values of natural frequencies or mode shape curves significantly. The influences of the two most commonly used boundary conditions in nanoengineering practice on the dynamic behavior of the embedded nanobeam were considered. It was found that the nanobeam with clamped-clamped boundary conditions has larger natural frequencies, and it is less sensitive to a change of parameters of the external magnetic field and temperature change. Thermal and longitudinal magnetic field effects on natural frequencies of cracked nanobeams were also investigated. Their influences are not negligible and can essentially change the vibration properties of nanobeams. This implies that the natural frequencies can be varied by a change in longitudinal magnetic field or temperature parameters without the necessity of changing the material and geometrical parameters of the nanosystem. These possibilities have great practical importance in the design of NEMS devices. A numerical parametric study was performed, and influences of various system parameters, such as the crack severities and position, nonlocality, longitudinal magnetic field, change in temperatures and stiffness of the elastic medium, on the natural frequency were investigated. It was found that the nonlocal parameter and crack severities have dampening effects on the natural frequency for both boundary conditions. Moreover, it can be seen that an increase in stiffness of the elastic medium leads to an increase in natural frequency, which implies an increase in the total stiffness of the system. In

addition, it is indicated that the influence of the crack position on the vibration mode is very important and significant for studying. The presented theoretical study can be very useful as a starting point in future analysis of dynamic and stability behaviors of more complex nanostructure systems with defects.

Appendix A

Let

$$X = v^2\left(\lambda_n^4 - \frac{K}{\tilde{a}}\right).$$

The frequency determinant in vibration analysis of the cracked nanobeam embedded in an elastic medium with simply supported boundary conditions is

$$|G(\lambda_n)| = \begin{vmatrix}
0 & 1 & 0 & 1 \\
0 & X+\alpha_n^2 & 0 & X-\beta_n^2 \\
\sinh(\alpha_n b) & \cosh(\alpha_n b) & \sin(\beta_n b) & \cos(\beta_n b) \\
C\alpha_n^2\sinh(\alpha_n b)+\alpha_n\cosh(\alpha_n b) & C\alpha_n^2\cosh(\alpha_n b)+\alpha_n\sinh(\alpha_n b) & -C\beta_n^2\sin(\beta_n b)+\beta_n\cos(\beta_n b) & -C\beta_n^2\cos(\beta_n b)-\beta_n\sin(\beta_n b) \\
(X+\alpha_n^2)\sinh(\alpha_n b) & (X+\alpha_n^2)\cosh(\alpha_n b) & (X-\beta_n^2)\sin(\beta_n b) & (X-\beta_n^2)\cos(\beta_n b) \\
(X\alpha_n+\alpha_n^3)\cosh(\alpha_n b) & (X\alpha_n+\alpha_n^3)\sinh(\alpha_n b) & (X\beta_n-\beta_n^3)\cos(\beta_n b) & -(X\beta_n+\beta_n^3)\sin(\beta_n b) \\
0 & 0 & 0 & 0 \\
0 & 0 & 0 & 0
\end{vmatrix}$$

$$\begin{vmatrix}
0 & 0 & 0 & 0 \\
0 & 0 & 0 & 0 \\
-\sinh(\alpha_n b) & -\cosh(\alpha_n b) & -\sin(\beta_n b) & -\cos(\beta_n b) \\
-\alpha_n\cosh(\alpha_n b) & -\alpha_n\sinh(\alpha_n b) & -\beta_n\cos(\beta_n b) & \beta_n\sin(\beta_n b) \\
-(X+\alpha_n^2)\sinh(\alpha_n b) & -(X+\alpha_n^2)\cosh(\alpha_n b) & -(X-\beta_n^2)\sin(\beta_n b) & -(X-\beta_n^2)\cos(\beta_n b) \\
-(X\alpha_n+\alpha_n^3)\cosh(\alpha_n b) & -(X\alpha_n+\alpha_n^3)\sinh(\alpha_n b) & -(X\beta_n-\beta_n^3)\cos(\beta_n b) & (X\beta_n+\beta_n^3)\sin(\beta_n b) \\
\sinh(\alpha_n) & \cosh(\alpha_n) & \sin(\beta_n) & \cos(\beta_n) \\
(X+\alpha_n^2)\sinh(\alpha_n) & (X+\alpha_n^2)\cosh(\alpha_n) & (X-\beta_n^2)\sin(\beta_n) & (X-\beta_n^2)\cos(\beta_n)
\end{vmatrix}.$$

The frequency determinant in vibration analysis of the cracked nanobeam embedded in an elastic medium with clamped-clamped boundary conditions is

$$|H(\lambda_n)| = \begin{vmatrix}
0 & 1 & 0 & 1 \\
\alpha_n & 0 & \beta_n & 0 \\
\sinh(\alpha_n b) & \cosh(\alpha_n b) & \sin(\beta_n b) & \cos(\beta_n b) \\
C\alpha_n^2\sinh(\alpha_n b)+\alpha_n\cosh(\alpha_n b) & C\alpha_n^2\cosh(\alpha_n b)+\alpha_n\sinh(\alpha_n b) & -C\beta_n^2\sin(\beta_n b)+\beta_n\cos(\beta_n b) & -C\beta_n^2\cos(\beta_n b)-\beta_n\sin(\beta_n b) \\
(X+\alpha_n^2)\sinh(\alpha_n b) & (X+\alpha_n^2)\cosh(\alpha_n b) & (X-\beta_n^2)\sin(\beta_n b) & (X-\beta_n^2)\cos(\beta_n b) \\
(X\alpha_n+\alpha_n^3)\cosh(\alpha_n b) & (X\alpha_n+\alpha_n^3)\sinh(\alpha_n b) & (X\beta_n-\beta_n^3)\cos(\beta_n b) & -(X\beta_n+\beta_n^3)\sin(\beta_n b) \\
0 & 0 & 0 & 0 \\
0 & 0 & 0 & 0
\end{vmatrix}$$

$$\begin{vmatrix}
0 & 0 & 0 & 0 \\
0 & 0 & 0 & 0 \\
-\sinh(\alpha_n b) & -\cosh(\alpha_n b) & -\sin(\beta_n b) & -\cos(\beta_n b) \\
-\alpha_n\cosh(\alpha_n b) & -\alpha_n\sinh(\alpha_n b) & -\beta_n\cos(\beta_n b) & \beta_n\sin(\beta_n b) \\
-(X+\alpha_n^2)\sinh(\alpha_n b) & -(X+\alpha_n^2)\cosh(\alpha_n b) & -(X-\beta_n^2)\sin(\beta_n b) & -(X-\beta_n^2)\cos(\beta_n b) \\
-(X\alpha_n+\alpha_n^3)\cosh(\alpha_n b) & -(X\alpha_n+\alpha_n^3)\sinh(\alpha_n b) & -(X\beta_n-\beta_n^3)\cos(\beta_n b) & (X\beta_n+\beta_n^3)\sin(\beta_n b) \\
\sinh(\alpha_n) & \cosh(\alpha_n) & \sin(\beta_n) & \cos(\beta_n) \\
\alpha_n\cosh(\alpha_n) & \alpha_n\sinh(\alpha_n) & \beta_n\cos(\beta_n) & -\beta_n\sin(\beta_n)
\end{vmatrix}.$$

The vector $\{\psi\}$ is composed of eight unknown constants D_{ni}, $i = 1, 2, \ldots, 8$, defined as

$$\{\psi\}^T = \{D_{n1}, D_{n2}, D_{n3}, D_{n4}, D_{n5}, D_{n6}, D_{n7}, D_{n8}\}^T.$$

References

[A. Haghshenas and Arani 2013] A. A. Haghshenas and A. G. Arani, "Nonlocal vibration of a piezoelectric polymeric nanoplate carrying nanoparticle via Mindlin plate theory", *Proc. Inst. Mech. Eng. C, J. Mech. Eng. Sci.* **228**:5 (2013), 907–920.

[Alper and Hamad-Schifferli 2010] J. Alper and K. Hamad-Schifferli, "Effect of ligands on thermal dissipation from gold nanorods", *Langmuir* **26**:6 (2010), 3786–3789.

[Ansari et al. 2012] R. Ansari, R. Gholami, and M. A. Darabi, "A nonlinear Timoshenko beam formulation based on strain gradient theory", *J. Mech. Mater. Struct.* **7**:2 (2012), 195–211.

[Arani et al. 2013] A. H. G. Arani, M. J. Maboudi, A. G. Arani, and S. Amir, "2D-Magnetic field and biaxiall in-plane pre-load effects on the vibration of double bonded orthotropic graphene sheets", *J. Solid Mech.* **5**:2 (2013), 193–205.

[Batra et al. 2007] R. C. Batra, M. Porfiri, and D. Spinello, "Review of modeling electrostatically actuated microelectromechanical systems", *Smart Mater. Struct.* **16**:6 (2007), R23.

[Belytschko et al. 2002] T. Belytschko, S. P. Xiao, G. C. Schatz, and R. S. Ruoff, "Atomistic simulations of nanotube fracture", *Phys. Rev. B* **65**:23 (2002), 235430.

[Benzair et al. 2008] A. Benzair, A. Tounsi, A. Besseghier, H. Heireche, N. Moulay, and L. Boumia, "The thermal effect on vibration of single-walled carbon nanotubes using nonlocal Timoshenko beam theory", *J. Phys. D Appl. Phys.* **41**:22 (2008), 225404.

[Bershtein et al. 2002] V. A. Bershtein, L. M. Egorova, P. N. Yakushev, P. Pissis, P. Sysel, and L. Brozova, "Molecular dynamics in nanostructured polyimide–silica hybrid materials and their thermal stability", *J. Polym. Sci. B Polym. Phys.* **40**:10 (2002), 1056–1069.

[Charlier 2002] J.-C. Charlier, "Defects in carbon nanotubes", *Acc. Chem. Res.* **35**:12 (2002), 1063–1069.

[Eringen 1972] A. C. Eringen, "Linear theory of nonlocal elasticity and dispersion of plane waves", *Int. J. Eng. Sci.* **10**:5 (1972), 425–435.

[Eringen 1983] A. C. Eringen, "On differential equations of nonlocal elasticity and solutions of screw dislocation and surface waves", *J. Appl. Phys.* **54**:9 (1983), 4703–4710.

[Fernández-Sáez and Navarro 2002] J. Fernández-Sáez and C. Navarro, "Fundamental frequency of cracked beams in bending vibrations: An analytical approach", *J. Sound Vib.* **256**:1 (2002), 17–31.

[Fernández-Sáez et al. 1999] J. Fernández-Sáez, L. Rubio, and C. Navarro, "Approximate calculation of the fundamental frequency for bending vibrations of cracked beams", *J. Sound Vib.* **225**:2 (1999), 345–352.

[Firouz-Abadi and Hosseinian 2012] R. D. Firouz-Abadi and A. R. Hosseinian, "Resonance frequencies and stability of a current-carrying suspended nanobeam in a longitudinal magnetic field", *Theor. Appl. Mech. Lett.* **2**:3 (2012), 031012.

[Gómez-Navarro et al. 2008] C. Gómez-Navarro, M. Burghard, and K. Kern, "Elastic properties of chemically derived single graphene sheets", *Nano Lett.* **8**:7 (2008), 2045–2049.

[Hasheminejad et al. 2011] B. S. M. Hasheminejad, B. Gheshlaghi, Y. Mirzaei, and S. Abbasion, "Free transverse vibrations of cracked nanobeams with surface effects", *Thin Solid Films* **519**:8 (2011), 2477–2482.

[Hosseini-Hashemi et al. 2014] S. Hosseini-Hashemi, I. Nahas, M. Fakher, and R. Nazemnezhad, "Surface effects on free vibration of piezoelectric functionally graded nanobeams using nonlocal elasticity", *Acta Mech.* **225**:6 (2014), 1555–1564.

[Hsieh et al. 2006] J.-Y. Hsieh, J.-M. Lu, M.-Y. Huang, and C.-C. Hwang, "Theoretical variations in the Young's modulus of single-walled carbon nanotubes with tube radius and temperature: A molecular dynamics study", *Nanotechnology* **17**:15 (2006), 3920.

[Jam et al. 2012] J. E. Jam, Y. Mirzaei, B. Gheshlaghi, and R. Avazmohammadi, "Size-dependent free vibration analysis of infinite nanotubes using elasticity theory", *J. Mech. Mater. Struct.* **7**:2 (2012), 137–144.

[Jensen 1999] P. Jensen, "Growth of nanostructures by cluster deposition: Experiments and simple models", *Rev. Mod. Phys.* **71**:5 (1999), 1695–1735.

[Karličić et al. 2014] D. Karličić, T. Murmu, M. Cajić, P. Kozić, and S. Adhikari, "Dynamics of multiple viscoelastic carbon nanotube based nanocomposites with axial magnetic field", *J. Appl. Phys.* **115**:23 (2014), 234303.

[Ke and Wang 2012] L.-L. Ke and Y.-S. Wang, "Thermoelectric-mechanical vibration of piezoelectric nanobeams based on the nonlocal theory", *Smart Mater. Struct.* **21**:2 (2012), 025018.

[Kiani 2012] K. Kiani, "Magneto–thermo–elastic fields caused by an unsteady longitudinal magnetic field in a conducting nanowire accounting for eddy-current loss", *Mater. Chem. Phys.* **136**:2–3 (2012), 589–598.

[Kiani 2014a] K. Kiani, "Free vibration of conducting nanoplates exposed to unidirectional in-plane magnetic fields using nonlocal shear deformable plate theories", *Physica E* **57** (2014), 179–192.

[Kiani 2014b] K. Kiani, "Vibration and instability of a single-walled carbon nanotube in a three-dimensional magnetic field", *J. Phys. Chem. Solids* **75**:1 (2014), 15–22.

[Kisa and Gurel 2006] M. Kisa and M. A. Gurel, "Modal analysis of multi-cracked beams with circular cross section", *Eng. Fract. Mech.* **73**:8 (2006), 963–977.

[Kozić et al. 2014] P. Kozić, R. Pavlović, and D. Karličić, "The flexural vibration and buckling of the elastically connected parallel-beams with a Kerr-type layer in between", *Mech. Res. Commun.* **56** (2014), 83–89.

[Li et al. 2011] S. Li, H. J. Xie, and X. Wang, "Dynamic characteristics of multi-walled carbon nanotubes under a transverse magnetic field", *Bull. Mater. Sci.* **34**:1 (2011), 45–52.

[Loya et al. 2006] J. A. Loya, L. Rubio, and J. Fernández-Sáez, "Natural frequencies for bending vibrations of Timoshenko cracked beams", *J. Sound Vib.* **290**:3–5 (2006), 640–653.

[Loya et al. 2009] J. Loya, J. López-Puente, R. Zaera, and J. Fernández-Sáez, "Free transverse vibrations of cracked nanobeams using a nonlocal elasticity model", *J. Appl. Phys.* **105**:4 (2009), 044309.

[Loya et al. 2014] J. A. Loya, J. Aranda-Ruiz, and J. Fernández-Sáez, "Torsion of cracked nanorods using a nonlocal elasticity model", *J. Phys. D Appl. Phys.* **47**:11 (2014), 115304.

[Martín et al. 2012] J. Martín, M. Hernández-Vélez, O. de Abril, C. Luna, A. Munoz-Martin, M. Vázquez, and C. Mijangos, "Fabrication and characterization of polymer-based magnetic composite nanotubes and nanorods", *Eur. Polym. J.* **48**:4 (2012), 712–719.

[Meyer et al. 2007] J. C. Meyer, A. K. Geim, M. I. Katsnelson, K. S. Novoselov, T. J. Booth, and S. Roth, "The structure of suspended graphene sheets", *Nature* **446**:7131 (2007), 60–63.

[Murmu and Pradhan 2009] T. Murmu and S. C. Pradhan, "Thermo-mechanical vibration of a single-walled carbon nanotube embedded in an elastic medium based on nonlocal elasticity theory", *Comput. Mater. Sci.* **46**:4 (2009), 854–859.

[Murmu and Pradhan 2010] T. Murmu and S. C. Pradhan, "Thermal effects on the stability of embedded carbon nanotubes", *Comput. Mater. Sci.* **47**:3 (2010), 721–726.

[Murmu et al. 2013] T. Murmu, M. A. McCarthy, and S. Adhikari, "In-plane magnetic field affected transverse vibration of embedded single-layer graphene sheets using equivalent nonlocal elasticity approach", *Compos. Struct.* **96** (2013), 57–63.

[Murmu et al. 2014] T. Murmu, S. Adhikari, and M. A. McCarthy, "Axial vibration of embedded nanorods under transverse magnetic field effects via nonlocal elastic continuum theory", *J. Comput. Theor. Nanosci.* **11**:5 (2014), 1230–1236.

[Narendar et al. 2012] S. Narendar, S. S. Gupta, and S. Gopalakrishnan, "Wave propagation in single-walled carbon nanotube under longitudinal magnetic field using nonlocal Euler–Bernoulli beam theory", *Appl. Math. Model.* **36**:9 (2012), 4529–4538.

[Niyogi et al. 2006] S. Niyogi, E. Bekyarova, M. E. Itkis, J. L. McWilliams, M. A. Hamon, and R. C. Haddon, "Solution properties of graphite and graphene", *J. Amer. Chem. Soc.* **128**:24 (2006), 7720–7721.

[Park et al. 2005] S. H. Park, J. S. Kim, J. H. Park, J. S. Lee, Y. K. Choi, and O. M. Kwon, "Molecular dynamics study on size-dependent elastic properties of silicon nanocantilevers", *Thin Solid Films* **492**:1–2 (2005), 285–289.

[Popov et al. 2007] A. M. Popov, E. Bichoutskaia, Y. E. Lozovik, and A. S. Kulish, "Nanoelectromechanical systems based on multi-walled nanotubes: Nanothermometer, nanorelay, and nanoactuator", *Phys. Status Solidi A* **204**:6 (2007), 1911–1917.

[Reddy and Pang 2008] J. N. Reddy and S. D. Pang, "Nonlocal continuum theories of beams for the analysis of carbon nanotubes", *J. Appl. Phys.* **103**:2 (2008), 023511.

[Roostai and Haghpanahi 2014] H. Roostai and M. Haghpanahi, "Vibration of nanobeams of different boundary conditions with multiple cracks based on nonlocal elasticity theory", *Appl. Math. Model.* **38**:3 (2014), 1159–1169.

[Sammalkorpi et al. 2004] M. Sammalkorpi, A. Krasheninnikov, A. Kuronen, K. Nordlund, and K. Kaski, "Mechanical properties of carbon nanotubes with vacancies and related defects", *Phys. Rev. B* **70**:24 (2004), 245416.

[Schniepp et al. 2006] H. C. Schniepp, J.-L. Li, M. J. McAllister, H. Sai, M. Herrera-Alonso, D. H. Adamson, R. K. Prud'homme, R. Car, D. A. Saville, and I. A. Aksay, "Functionalized single graphene sheets derived from splitting graphite oxide", *J. Phys. Chem. B* **110**:17 (2006), 8535–8539.

[Torabi and Dastgerdi 2012] K. Torabi and J. N. Dastgerdi, "An analytical method for free vibration analysis of Timoshenko beam theory applied to cracked nanobeams using a nonlocal elasticity model", *Thin Solid Films* **520**:21 (2012), 6595–6602.

[Wei and Wang 2004] L. Wei and Y.-N. Wang, "Electromagnetic wave propagation in single-wall carbon nanotubes", *Phys. Lett. A* **333**:3–4 (2004), 303–309.

[Wu et al. 2005] B. Wu, A. Heidelberg, and J. J. Boland, "Mechanical properties of ultrahigh-strength gold nanowires", *Nat. Mater.* **4**:7 (2005), 525–529.

[Xie et al. 2000] S. Xie, W. Li, Z. Pan, B. Chang, and L. Sun, "Mechanical and physical properties on carbon nanotube", *J. Phys. Chem. Solids* **61**:7 (2000), 1153–1158.

[Xing et al. 2004] Y. J. Xing, Z. H. Xi, X. D. Zhang, J. H. Song, R. M. Wang, J. Xu, Z. Q. Xue, and D. P. Yu, "Nanotubular structures of zinc oxide", *Solid State Comm.* **129**:10 (2004), 671–675.

[Yang and Chen 2008] J. Yang and Y. Chen, "Free vibration and buckling analyses of functionally graded beams with edge cracks", *Compos. Struct.* **83**:1 (2008), 48–60.

[Youssef and Elsibai 2011] H. M. Youssef and K. A. Elsibai, "Vibration of gold nanobeam induced by different types of thermal loading—a state-space approach", *Nanoscale Microscale Thermophys. Eng.* **15**:1 (2011), 48–69.

[Yum and Yu 2006] K. Yum and M.-F. Yu, "Measurement of wetting properties of individual boron nitride nanotubes with the Wilhelmy method using a nanotube-based force sensor", *Nano Lett.* **6**:2 (2006), 329–333.

[Zhang et al. 2005] S. Zhang, S. L. Mielke, R. Khare, D. Troya, R. S. Ruoff, G. C. Schatz, and T. Belytschko, "Mechanics of defects in carbon nanotubes: Atomistic and multiscale simulations", *Phys. Rev. B* **71**:11 (2005), 115403.

[Zhang et al. 2008] Y. Q. Zhang, X. Liu, and J. H. Zhao, "Influence of temperature change on column buckling of multiwalled carbon nanotubes", *Phys. Lett. A* **372**:10 (2008), 1676–1681.

[Zhou and Shi 2003] L. G. Zhou and S.-Q. Shi, "Formation energy of Stone–Wales defects in carbon nanotubes", *Appl. Phys. Lett.* **83**:6 (2003), 1222–1224.

DANILO KARLIČIĆ: danilo.karlicic@masfak.ni.ac.rs
Faculty of Mechanical Engineering, University of Niš, Aleksandra Medvedeva 14, 18000 Niš, Serbia

DRAGAN JOVANOVIĆ: jdragan@masfak.ni.ac.rs
Faculty of Mechanical Engineering, University of Niš, Aleksandra Medvedeva 14, 18000 Niš, Serbia

PREDRAG KOZIĆ: kozicp@yahoo.com
Faculty of Mechanical Engineering, University of Niš, Aleksandra Medvedeva 14, 18000 Niš, Serbia

MILAN CAJIĆ: caja84@gmail.com
Mathematical Institute of the Serbian Academy of Sciences and Arts, Kneza Mihaila 36, 11001 Belgrade, Serbia

msp

CONTOURS FOR PLANAR CRACKS GROWING IN THREE DIMENSIONS

LOUIS MILTON BROCK

A three-dimensional dynamic steady state analysis for extension of a semi-infinite plane crack is considered. Fracture is brittle and driven by loads applied to the crack surfaces. An analytical solution is obtained, and examined in light of two criteria: energy release (rate) and strain energy density. Introduction of a quasipolar coordinate system allows, for each criterion, generation of a nonlinear first-order differential equation for the distance from the origin to any point on the crack edge. These in turn give insight into the crack contour generated by the crack edge. In particular, for loading by compressive point forces, the equation generated by the energy release (rate) criterion is solved exactly. Calculations depict a crack edge contour that tends to the rectilinear, but deviates markedly from that near the point forces.

Introduction

The author considers sliding contact in the 3D dynamic steady state by rigid dies in [Brock 2012; 2014a; 2014b; 2015]. Basic die shapes — sphere, ellipsoid, cone — are treated [Brock 2012; 2014a], but also more complicated shapes [Brock 2014a; 2014b; 2015] that preclude simple connectivity of the contact zone [Brock 2014b] or a single contact zone [Brock 2015]. These 3D studies demonstrate the sensitivity of contact zone contour to sliding speed, and show that contact zone shape does not necessarily replicate the projection of the die profile onto the half-space.

An analogous goal in fracture mechanics is to determine crack edge location. In 2D dynamic fracture, this requires an equation of motion for the crack tip [Freund 1990]. In a 3D study, such an equation must describe the crack contour defined by crack edge location. The paper, therefore, considers semi-infinite crack growth in an unbounded solid. For simplicity, the crack is assumed to (a) remain in its original plane, (b) be driven by crack surface loads that translate at constant subcritical speed in a fixed direction and (c) achieve a dynamic steady state.

While analogous, the study does not enjoy some features of [Brock 2012; 2014a; 2014b; 2015]: (a) die/half-space conformation is paramount in defining the solution, (b) the (valid) assumption of a "small" contact zone often allows conformation to be expressed in terms of polynomials and (c) solution of the conformation equation itself can be simplified under the same assumption, e.g. [Brock 2014a]. Prescribed geometrical properties do not in general define fracture criteria. Indeed, geometrical features (crack edge location, crack contour) are outputs. Therefore, approximations for the equation of crack edge location may be unrealistic.

The 3D analysis begins by considering the unmixed boundary value problem for a displacement discontinuity imposed over a semi-infinite plane area A_C contained in an unbounded solid. The discontinuity vanishes along area boundary C, vanishes at infinite distances from it, and translates with A_C at constant subcritical speed V in a fixed direction. A dynamic steady state ensues and allows use of a translating

Cartesian basis. The transform solution is generated, but a quasipolar coordinate system is introduced in the inversion process. Expressions for traction on the plane of A_C lead to classical singular integral equations for the displacement discontinuity produced were A_C a crack subject to prescribed surface loads. Two fracture criteria are considered, and each leads to a nonlinear first-order differential equation for the distance from a fixed point in A_C to any point on (now) crack edge C.

Displacement discontinuity growth — governing equations

Consider an unbounded, isotropic and linearly elastic solid. In terms of Cartesian basis $\boldsymbol{x} = \boldsymbol{x}(x_k)$, semi-infinite planar region ($x_3 = 0$, $x_1 < 0$) A_C is subject to discontinuity

$$[\boldsymbol{u}(u_k)] = \boldsymbol{U}(U_k). \tag{1}$$

Here $k = (1, 2, 3)$, [ ] signifies a jump as travel from $x_3 = 0-$ to $x_3 = 0+$ occurs, $\boldsymbol{u}$ is the displacement field and $U_k = U_k(x_1, x_2)$ discontinuity components. Region extension then occurs in the positive x_1-direction with constant subcritical speed V. A dynamic steady state is achieved such that $\boldsymbol{U}$ does not change, and region boundary C assumes a fixed, albeit no longer rectilinear, profile. Displacement $\boldsymbol{u}(u_k)$ and traction $\boldsymbol{T}(\sigma_{ik})$ are invariant in the moving frame of A_C. Basis $\boldsymbol{x}$ is therefore translated with A_C so that $u_k = u_k(\boldsymbol{x})$, $U_k = U_k(x_1, x_2)$, $\sigma_{ik} = \sigma_{ik}(\boldsymbol{x})$ and the time derivative can be written as $-V\partial_1$. Here ∂_k signifies x_k-differentiation. For convenience $\boldsymbol{x} = 0$ is located in the dislocation region, so that function $\Im(x_1, x_2) = 0$, $\sqrt{x_1^2 + x_2^2} \neq 0$ defines contour C and the region can be defined as $(x_1, x_2) \in A_C$. Both $\Im$ and its gradient $\nabla\Im$ are continuous, and any line passing through $\boldsymbol{x} = 0$ in the $x_1 x_2$-plane can cross C only once. For $x_3 \neq 0$, governing equations for $\boldsymbol{u}(x_k)$ can be written as [Brock 2012]

$$\boldsymbol{u} = \boldsymbol{u}_D + \boldsymbol{u}_S, \tag{2a}$$

$$(\nabla^2 - c^2 \partial_1^2)\boldsymbol{u}_S = 0, \quad \nabla \cdot \boldsymbol{u}_S = 0, \tag{2b}$$

$$(c_D^2 \nabla^2 - c^2 \partial_1^2)\boldsymbol{u}_D = 0, \quad \nabla \times \boldsymbol{u}_D = 0. \tag{2c}$$

In (2) ∇^2 is the Laplacian, and traction $\boldsymbol{T}$ is defined by

$$\frac{1}{\mu}\boldsymbol{T} = [(c_D^2 - 2)\nabla \cdot \boldsymbol{u}_D]\boldsymbol{1} + 2(\nabla\boldsymbol{u} + \boldsymbol{u}\nabla). \tag{3}$$

Term $\boldsymbol{1}$ is the identity tensor, and (c, c_D) are dimensionless ratios

$$c = \frac{V}{V_S}, \quad c_D = \frac{V_D}{V_S}. \tag{4}$$

Here (V, V_S, V_D) are, respectively, translation speed, shear wave speed, and dilatational wave speed, where

$$c_D = \sqrt{2\frac{1 - v}{1 - 2v}}, \quad V_S = \sqrt{\frac{\mu}{\rho}}. \tag{5}$$

In (2)–(5), (v, μ, ρ) are Poisson's ratio, shear modulus and mass density, and $1 < c_D$. In light of (1),

conditions for $x_3 = 0$ are

$$[u_k] = U_k (x_1, x_2) \in A_C, \quad [u_k] = 0 \, (x_1, x_2) \notin A_C, \tag{6a}$$

$$[\sigma_{3k}] = 0. \tag{6b}$$

Components U_k are not specified, but must be finite and continuous for $(x_1, x_2) \in A_C$. Therefore $U_k = 0$ for $\Im(x_1, x_2) = 0$, and $(\boldsymbol{u}, \boldsymbol{T})$ should remain finite for $|\boldsymbol{x}| \to \infty$, $x_3 \neq 0$.

General transform solution

A double bilateral transform [Sneddon 1972] can be defined as

$$\hat{F} = \iint F(x_1, x_2) \exp(-p_1 x_1 - p_2 x_2) \, dx_1 \, dx_2. \tag{7}$$

Integration is along the entire $\mathrm{Re}(x_1)$ and $\mathrm{Re}(x_2)$-axes. Application of (7) to (2) gives

$$\hat{\boldsymbol{u}}_S = \boldsymbol{V} \exp(-B|x_3|), \quad \hat{\boldsymbol{u}}_D = \boldsymbol{U} \exp(-A|x_3|), \tag{8a}$$

$$p_1 V_1 + p_2 V_2 - B V_3 = 0, \quad \boldsymbol{U} = (p_1, p_2, -A)U. \tag{8b}$$

Terms (B, A) are roots of the transforms of, respectively, (2b) and (2c), given by

$$B = \sqrt{-D + c^2 p_1^2}, \quad A = \sqrt{-D + (c^2/c_D^2)p_1^2}, \quad D = p_1^2 + p_2^2. \tag{9}$$

Equation (8) is bounded for $x_3 \neq 0$ if branch cuts are introduced so that $\mathrm{Re}(B, A) \geq 0$ in the cut complex (p_1, p_2)-planes. Application of (7) to (6) and substitution of (8) and (9) gives equations for (U, V_1, V_2) in terms of transforms $\hat{U}_k$. The solutions for $x_3 \geq 0(+)$ and $x_3 \leq 0(-)$ are given by (A.1). Expressions for traction $(\sigma_{33}, \sigma_{31}, \sigma_{32})$ in plane $x_3 = 0$ are also required and, in light of (3), (7) and (A.1), their transforms are given by (A.3).

Transform inversion — general formulas

In (6), inhomogeneous terms (U_1, U_2, U_3) arise only for $(x_1, x_2) \in A_C$. In light of (A.3), therefore, the inversion operation corresponding to (7) gives $(\sigma_{33}, \sigma_{31}, \sigma_{32})$ for $x_3 = 0$ as linear combinations of expressions

$$\iint U_k \, d\xi_1 \, d\xi_2 \frac{1}{2\pi i} \int dp_1 \frac{1}{2\pi i} \int P_k \, dp_2 \exp[p_1(x_1 - \xi_1) + p_2(x_2 - \xi_2)]. \tag{10}$$

Here $U_k = U_k(\xi_1, \xi_2)$ and $P_k = P_k(p_1, p_2)$ is the corresponding coefficient. Double integration is over region A_C, and single integration is over the entire $\mathrm{Im}(p_1)$ and $\mathrm{Im}(p_2)$-axes. The form of (10) suggests definitions and transformations [Brock 2012]:

$$p_1 = p \cos \psi, \quad p_2 = p \sin \psi, \tag{11a}$$

$$\begin{bmatrix} x \\ y \end{bmatrix} = \begin{bmatrix} \cos \psi & \sin \psi \\ -\sin \psi & \cos \psi \end{bmatrix} \begin{bmatrix} x_1 \\ x_2 \end{bmatrix}, \quad \begin{bmatrix} \xi \\ \eta \end{bmatrix} = \begin{bmatrix} \cos \psi & \sin \psi \\ -\sin \psi & \cos \psi \end{bmatrix} \begin{bmatrix} \xi_1 \\ \xi_2 \end{bmatrix}. \tag{11b}$$

In (11), $\mathrm{Re}(p) = 0+$, $|\mathrm{Im}(p), x, y, \xi, \eta| < \infty$ and $|\psi| < \pi/2$. Parameters (p, ψ), $(x, \psi; y = 0)$ and $(\xi, \psi; \eta = 0)$ resemble quasipolar coordinate systems, i.e.,

$$d\xi_1 \, d\xi_2 = |\xi| \, d\xi \, d\psi, \quad dp_1 \, dp_2 = |p| \, dp \, d\psi. \tag{12}$$

Use of (11) and (12) in (9) and (A.3) give

$$D = p^2, \qquad\qquad B = B\sqrt{-p^2}, \qquad\qquad A = A\sqrt{-p^2}, \qquad K = Kp^2, \tag{13a}$$

$$B = \sqrt{1 - c^2 \cos^2 \psi}, \quad A = \sqrt{1 - (c^2/c_D^2) \cos^2 \psi}, \quad K = c^2 \cos^2 \psi - 2. \tag{13b}$$

In light of (7) and conditions for contour function $\Im$, (10) assumes the form

$$\frac{1}{i\pi} \int_\Psi P_k \, d\psi \int_N d\eta \frac{\partial}{\partial x} \int_X d\xi \frac{\partial U_k}{\partial \xi}(\xi, \eta) \frac{1}{2\pi i} \int \frac{|p|}{p} \frac{\sqrt{-p}}{\sqrt{p}} \, dp \exp(p(x - \xi)). \tag{14}$$

Symbols (N, X, Ψ) signify integration over ranges $|\psi| < \pi/2$, $N^- < \eta < N^+$ and $X_- < \psi < X_+$, respectively. Here $P_k = P_k(\psi)$, and p-integration is along the positive side of the entire imaginary axis. Terms in (8) are bounded for positive and real (B, A) if branches $\mathrm{Im}(p) = 0$, $\mathrm{Re}(p) < 0$ and $\mathrm{Im}(p) = 0$, $\mathrm{Re}(p) > 0$ are introduced for $\sqrt{\pm p}$, respectively, such that $\mathrm{Re}(\sqrt{\pm p}) > 0$ in the cut p-plane. The p-integration is given in Appendix B so that, in view of the condition that U_k vanish continuously on C [Brock 2012],

$$\frac{1}{\pi} \int_\Psi P_k \, d\psi \frac{\partial}{\partial x} \int_N d\eta \frac{1}{\pi} \int_X \frac{\partial U_k}{\partial \xi}(\xi, \eta) \frac{d\xi}{\xi - x}. \tag{15}$$

Limits $N^\pm(\psi)$ in (15) are defined by

$$\Im(\xi_1(\xi, N^\pm), \xi_2(\xi, N^\pm)) = 0, \quad \frac{dN^\pm}{d\xi} = 0. \tag{16}$$

That is, for given ψ, limits $N^\pm$ are the maximum and minimum values of η on C, and for given η, limits $X_\pm(\psi, \eta)$ locate the ends of lines that run parallel to the ξ-axis and that span C. Conditions on C imply that these limits exist, are single-valued, and vary continuously in ψ. In particular, the semi-infinite nature of A_C guarantees that $X_- \to -\infty$ for portions of Ψ. Figure 1 gives a generic sketch of A_C for the case that $N^+(\psi) \to \infty$ and $|X_-(\psi, \eta)|$ is finite but too large to appear.

In light of (7)–(13), traction in A_C itself, i.e., $x_3 = 0$, $(x_1, x_2) \in A_C$, can be written as

$$\sigma_{3k} = -\frac{1}{\pi} \int_\Psi d\psi \int_N d\eta \frac{\partial}{\partial x} \int_X d\xi \, \delta(\xi, \eta) \sigma_{3k}(x_1(\xi, \eta), x_2(\xi, \eta)). \tag{17}$$

In (17), δ is the Dirac function. Therefore, expressions for traction in A_C can be obtained by matching the integrands of (ψ, η)-integration in (17) with combinations of those in (15). Moreover, ξ in (15) and (17) is an integration variable representing parameter x that itself depends on (x_1, x_2) and ψ. As noted in connection with (11), coordinates (x_1, x_2) can be replaced by (x, ψ) for $y = 0$. Thus every point $(x_1, x_2) \in A_C$ lies on an integration path $\eta = 0$ that passes through both limit points of the ξ-integral. The resulting expressions for traction in A_C are given in Appendix C. Equation (13b) shows that (B, A) are positive and real so long as $c < 1$. Term R in (C.3) is the Rayleigh function [Achenbach 1975] of argument $c \cos \psi$ and vanishes at value $c \cos \psi = c_R$ ($0 < c_R < 1$) where $V_R = c_R V_S$ is the Rayleigh wave
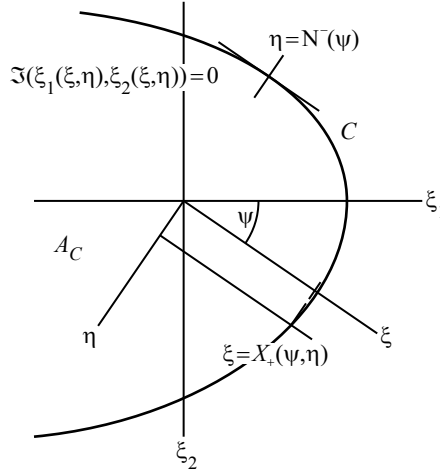
Figure 1. Schematic of semi-infinite area A_C and contour C.

speed. To avoid critical behavior, therefore, the translation speed of C is subject to restriction $0 < c < c_R$. Crack extension in the dynamic steady state can now be treated. The treatment begins with some basic results for extension caused by crack surface traction.

Related crack extension problem: basic results

Region A_C in the dynamic steady state is now a crack whose two surfaces are subjected to traction $(-\sigma_{33}^C, -\sigma_{31}^C, -\sigma_{32}^C)$, with $\sigma_{3k}^C > 0$. Crack geometry, i.e., C, $\Im(x_1, x_2) = 0$ and V, is the same as before. The conditions placed on U_k above are relevant for fracture. In light of 2D dynamic steady state analyses of semi-infinite cracks [Brock 1999] therefore, $(\sigma_{33}^C, \sigma_{31}^C, \sigma_{32}^C)$ must be finite and piecewise continuous. Behavior should also be such that, for $(x_1, x_2) \in A_C$,

$$\sigma_{3k}^C \approx O((x_1^2 + x_2^2)^{-\chi}), \quad \sqrt{x_1^2 + x_2^2} \to \infty \ (\chi > 1). \tag{18}$$

Coupled singular integral equations for x-derivatives of (now-unknown) components (U_1, U_2, U_3) are provided by (C.3), with σ_{3k} replaced by $-\sigma_{3k}^C$. Solution gives the derivatives and the functions themselves. To emphasize aspects of 3D behavior, σ_{3k}^C-values are maximum near $(x_1, x_2) = 0$. It is then reasonable to assume that any curvature of crack edge C will produce an essentially concave profile with respect to $(x_1, x_2) = 0$. In view of the original restrictions on C, then, two cases arise. For $X_+ = x_+(\psi) > 0$, $X_- = -x_-(\psi)$,

$$\frac{\partial U_k}{\partial x} = \frac{1}{\sqrt{x_+ - x}\sqrt{x + x_-}} \frac{(\text{vp})}{\pi} \int_X \frac{g_k(\xi, \psi)}{\xi - x} \sqrt{x_+ - \xi}\sqrt{\xi + x_-} \, d\xi, \tag{19a}$$

$$U_k = \frac{1}{\pi} \int_X g_k(\xi, \psi) \ln \left| \frac{\sqrt{x_+ - x}\sqrt{\xi + x_-} - \sqrt{x + x_-}\sqrt{x_+ - \xi}}{\sqrt{x_+ - x}\sqrt{\xi + x_-} + \sqrt{x + x_-}\sqrt{x_+ - \xi}} \right| \, d\xi. \tag{19b}$$

Continuity of C requires that $x_\pm(\pi/2) = x_\mp(-\pi/2)$. For $X_+ = x_+(\psi)$, $X_- \to -\infty$,

$$\frac{\partial U_k}{\partial x} = \frac{1}{\sqrt{x_+ - x}} \frac{(\text{vp})}{\pi} \int_X \frac{g_k(\xi, \psi)}{\xi - x} \sqrt{x_+ - \xi} \, d\xi, \tag{20a}$$

$$U_k = \frac{1}{\pi} \int_X g_k(\xi, \psi) \ln \left| \frac{\sqrt{x_+ - \xi} - \sqrt{x_+ - x}}{\sqrt{x_+ - \xi} + \sqrt{x_+ - x}} \right| d\xi. \tag{20b}$$

Continuity of C now requires that $x_+(\pm\pi/2) \to \infty$. Equations (19b) and (20b) vanish continuously on C, as required. In (19) and (20),

$$g_1 = \frac{1}{N} \left[\frac{M}{B} \left(\frac{\sigma_{32}^C}{\mu} \cos \psi - \frac{\sigma_{31}^C}{\mu} \sin \psi \right) \sin \psi - \frac{\sigma_{31}^C}{\mu} Bc^2 \cos^2 \psi \right], \tag{21a}$$

$$g_2 = \frac{1}{N} \left[\frac{M}{B} \left(\frac{\sigma_{32}^C}{\mu} \sin \psi - \frac{\sigma_{12}^C}{\mu} \cos \psi \right) \cos \psi - \frac{\sigma_{32}^C}{\mu} Bc^2 \cos^2 \psi \right], \tag{21b}$$

$$g_3 = -\frac{2A}{R} \frac{\sigma_{33}^C}{\mu} c^2 \cos^2 \psi. \tag{21c}$$

Substitution of (19a) and (20a) into (15), but then performing the ξ-integration for $x \notin X$ leads to, respectively, expressions for traction on plane $x_3 = 0$, $(x, \psi) \notin A_C$,

$$\sigma_{3k} = \frac{1}{\pi \sqrt{x_+ - x} \sqrt{x_- + x}} \int_X \frac{\sigma_{3k}^C(\xi, \psi)}{\xi - x} \sqrt{x_+ - \xi} \sqrt{\xi + x_-} \, d\xi, \tag{22a}$$

$$\sigma_{3k} = \frac{1}{\pi \sqrt{x_+ - x}} \int_X \frac{\sigma_{3k}^C(\xi, \psi)}{\xi - x} \sqrt{x_+ - \xi} \, d\xi. \tag{22b}$$

Brittle fracture parameter: energy release (rate)

After [Griffith 1921], crack growth occurs when the rate of surface energy release balances that of potential energy decrease. For the 2D brittle crack, this criterion equates the rate per unit length (of crack edge) of energy release and negative of power per unit length generated in the crack plane [Achenbach 1975; Freund 1990]. Here, total release rate $\Re$ and total power are considered. Use of (8) for the dynamic steady state gives

$$\Re = -V \int_\Psi d\psi \left[\int_{-\infty}^{\infty} |x| \, dx \, \sigma_{3k} \partial_1 U_k + \int_X |x| \, dx \, \sigma_{3k}^C \partial_1 U_k \right], \tag{23a}$$

$$\partial_1 = \cos \psi \frac{\partial}{\partial x} - \frac{\sin \psi}{|x|} \frac{\partial}{\partial \psi}, \qquad \partial_2 = \sin \psi \frac{\partial}{\partial x} + \frac{\cos \psi}{|x|} \frac{\partial}{\partial \psi}. \tag{23b}$$

The summation convention is understood in (23a). To illustrate the form of $\Re$, the ∂_1-operator is applied to case (20b) as

$$\partial_1 U_k = -\frac{(\text{vp})}{\pi \sqrt{x_+ - x}} \int_X g_k \, d\xi \left[\frac{\sqrt{x_+ - \xi}}{\xi - x} \cos \psi - \frac{\sin \psi}{|x| \sqrt{x_+ - \psi}} \frac{dx_+}{d\psi} \right]$$

$$+ \frac{\sin \psi}{\pi |x|} \int_X d\xi \ln \left| \frac{\sqrt{x_+ - \xi} + \sqrt{x_+ - x}}{\sqrt{x_+ - \xi} - \sqrt{x_+ - x}} \right| \frac{\partial g_k}{\partial \psi}. \tag{24}$$

The x-integration sum, (17), (19b), (22b) and (24) imply that $\Re = 0$ in (23a). But in the sense of a distribution each term in the sum gives [Achenbach and Brock 1973]

$$\frac{H(x_+ - x)}{\sqrt{x_+ - x}} \frac{H(x - x_+)}{\sqrt{x - x_+}} = \frac{\pi}{2}\delta(x - x_+). \tag{25}$$

Here H is the step function. Also, $\Re$ is assumed invariant with respect to its integrand in (23a). Singular behavior guarantees invariance in terms of x, so that the integrand need only be constant in terms of ψ. Therefore, for $|\psi| < \pi/2$,

$$\frac{\Re}{\sqrt{\mu\rho}} = \frac{-c}{\pi} \frac{d}{x_+ \, d\psi}(x_+ \sin\psi) \int_X \frac{\sigma_{3k}^C \, d\xi}{\mu\sqrt{x_+ - \xi}} \int_X \frac{g_k \, d\xi}{\sqrt{x_+ - \xi}}. \tag{26}$$

Equation (26) is, in effect, a nonlinear differential equation for $x_+(\psi)$. Equation (26) is based on (20). Thus for $|\psi| = \pi/2$, $x_+ \to \infty$ yet $\Re$ is invariant and finite. For $|\psi| \approx \pi/2$, Equations (13b), (18), (21), (C.3) and (26) lead to asymptotic forms

$$\int_X \frac{\sigma_{3k}^C(t, \psi)}{\sqrt{x_+ - t}} \, dt \approx -\frac{\Sigma_{3k}}{x_+^{\chi - 1/2}} G_\chi, \quad G_\chi = \int_{-1}^{\infty} \frac{du}{u^\chi \sqrt{1 + u}}, \tag{27a}$$

$$\frac{\Re}{\sqrt{\mu\rho}} \approx \frac{c}{8\pi^2} \frac{G_\chi^2}{x_+^{2\chi}} \frac{dx_+}{d\psi}\left(\frac{c_D^2}{c_D^2 - 1}\Sigma_{33}^2 + \Sigma_{31}^2 - \Sigma_{32}^2\right). \tag{27b}$$

It is noted that the right-hand side of (27b) is finite when $x_+ \approx O(1/\sqrt{\cos\psi})$ for $|\psi| \approx \pi/2$ and $\chi = \frac{3}{2}$. It is also to be noted that for $\psi = 0$, (26) in fact involves only $x_+(0)$ itself.

Brittle fracture parameter: strain energy density

Another brittle fracture model [Sih 1973] posits that an edge segment of a stationary crack will extend in a given direction if the strain energy density E achieves a maximum in that direction, where

$$\frac{E}{\mu} = \frac{c_D^2}{2}\varphi_1 - 2\varphi_2, \tag{28a}$$

$$\varphi_1 = e_{11} + e_{22} + e_{33}, \quad \varphi_2 = e_{11}e_{22} + e_{22}e_{33} + e_{33}e_{11} - e_{12}^2 - e_{23}^2 - e_{31}^2. \tag{28b}$$

Equation (28b) gives the first and second invariant of strain, where $2e_{ik} = \partial_i u_k + \partial_k u_i$. Behavior near the crack edge, i.e., distance $r \to 0$, for brittle fracture, is

$$E \approx \frac{S}{r}. \tag{29}$$

Therefore S is the key parameter. In keeping with the study of energy release rate, we examine the strain energy W itself in a thin "tube" that encases crack edge C. This value is infinite, but the result obtained below will correspond to (28). Results for $x_3 \neq 0$ are now required. In view of (7)–(14) and (A.1),

components of $\partial u_k / \partial x$ can be written as real or imaginary parts of a complex form as

$$\frac{1}{i\pi} \int_{\Psi} d\psi \int_N d\eta \frac{\partial}{\partial x} \int_X d\xi \frac{\partial U_k}{\partial \xi}(\xi, \eta) \frac{1}{2\pi i} \int \frac{|p|}{p} \left[P_k \frac{\sqrt{-p}}{\sqrt{p}} + i Q_k \right] dp$$

$$\times \exp(p(x - \xi) - \sqrt{-p}\sqrt{p}\Omega|x_3|). \quad (30)$$

Symbol Ω represents (A, B) defined by (13b). The p-integration is obtained from Appendix B. Use of (20a) and a result corresponding to (17) gives generic form

$$\frac{1}{\pi^2} \int_X g_k \, dt \sqrt{x_+ - t} \frac{1}{\pi} \int_X \frac{d\xi}{(t - \xi)\sqrt{\xi - x_+}} \frac{P_k + i Q_k}{x - \xi - i\Omega|x_3|}. \quad (31)$$

The ξ-integration is performed by residue theory. Integration of (31) with respect to x, in view of the condition that u_k vanish on C, gives a generic form for u_k-components

$$-\frac{1}{\pi^2}(P_k + i Q_k) \int_X g_k \ln \frac{\sqrt{P} - \sqrt{x_+ - t}}{\sqrt{P} + \sqrt{x_+ - t}} \, dt, \quad P = x - x_+ - i\Omega|x_3|. \quad (32)$$

Equation (28b) requires ∇u_k, and (11) shows that x_k-dependence in (32) is bound up in P which, for case $\Omega = A$, is

$$P = r_A \exp(i\phi_A), \quad (33a)$$

$$r_A = \sqrt{(x - x_+)^2 + A^2 x_3^2}, \quad \phi_A = \tan^{-1} \frac{A x_3}{x - x_+} \quad (|\phi_A| < \pi). \quad (33b)$$

Knowledge of ∇u_k near C suffices for (29), so, for $\Omega = A$, (32) can be replaced with the asymptotic result

$$\frac{1}{\pi^2}(P_k + i Q_k) \int_X \frac{g_k \, dt}{\sqrt{x_+ - t}} \sqrt{r_A} \exp\left(i \frac{\phi_A}{2}\right) + O(r_A). \quad (34)$$

This form suggests that for given ψ a standard polar coordinate system (r, ϕ), centered on C, be defined in the $x - x_3$ plane with

$$r = \sqrt{(x - x_+)^2 + x_3^2} \quad (r \approx 0), \quad \phi = \tan^{-1} \frac{x_3}{x - x_+} \quad (|\phi| < \pi). \quad (35)$$

Operations $(\partial_1, \partial_2, \partial_3)$ on (34) required for ∇u_k follow, respectively, in view of (11), (23b), (33) and (35), as

$$\frac{-1}{\pi^2 A_\Phi \sqrt{2r}}(P_k + i Q_k) \int_X \frac{g_k \, dt}{\sqrt{x_+ - t}}[A_+ + i A_- \operatorname{sgn}(\phi)] \frac{d}{x_+ \, d\psi}(x_+ \sin \psi), \quad (36a)$$

$$\frac{1}{\pi^2 A_\Phi \sqrt{2r}}(P_k + i Q_k) \int_X \frac{g_k \, dt}{\sqrt{x_+ - t}}[A_+ + i A_- \operatorname{sgn}(\phi)] \frac{d}{x_+ \, d\psi}(x_+ \cos \psi), \quad (36b)$$

$$\frac{i A}{\pi^2 A_\Phi \sqrt{2r}}(P_k + i Q_k) \int_X \frac{g_k \, dt}{\sqrt{x_+ - t}}[A_+ + i A_- \operatorname{sgn}(\phi)] \operatorname{sgn}(\phi). \quad (36c)$$

The result for $\Omega = B$ follows by replacing $(A_\pm, A_\Phi)$ with $(B_\pm, B_\Phi)$, where

$$A_\Phi = \sqrt{1 - (c^2/c_D^2)\cos^2\psi \sin^2\phi}, \quad A_\pm = \sqrt{A_\Phi \pm \cos\phi}, \tag{37a}$$

$$B_\Phi = \sqrt{1 - c^2\cos^2\psi \sin^2\phi}, \qquad B_\pm = \sqrt{B_\Phi \pm \cos\phi}. \tag{37b}$$

Derivatives with respect to ψ, it is noted, for (P_k, Q_k, g_k), $(A_\pm, A_\Phi, A)$ and $(B_\pm, B_\Phi, B)$ in (34) are associated with terms that vanish as $r \to 0$; see (24). To illustrate the results of (36), strain components for the case of pure crack surface compression $(\sigma_{31}^C = \sigma_{32}^C = 0)$ are given in Appendix D. Equations (28), (29), (36) and (D.1) show that

$$E \approx \frac{1}{r}\Sigma(\psi, \phi). \tag{38}$$

In view of (21), therefore, $\Sigma(\psi, \phi)$ is quadratic in

$$\int_X \frac{\sigma_{3k}^C \, dt}{\sqrt{x_+ - t}}, \quad \frac{d}{x_+ \, d\psi}(x_+ \sin\psi), \quad \frac{d}{x_+ \, d\psi}(x_+ \cos\psi). \tag{39}$$

Strain energy W in a thin tube ($r \approx 0$) that encases crack edge C can be written as

$$W = r \int_\Phi d\phi \int_\Psi \Sigma(\psi, \phi) \, dC(\psi), \quad dC(\psi) = \sqrt{x_+^2 + (dx_+/d\psi)^2} \, d\psi. \tag{40}$$

Symbol Φ signifies integration over range $|\phi| < \pi$ and $dC(\psi)$ is the increment of length along the crack edge. If W is assumed to be invariant, a critical strain energy density parameter for $|\psi| < \pi/2$ is

$$\frac{\partial^2 W}{\partial r \partial \psi} = S_C = \int_\Phi \Sigma(\psi, \phi) \, d\phi \sqrt{x_+^2 + (dx_+/d\psi)^2}. \tag{41}$$

While more complicated than energy release rate $\mathfrak{R}$ given by (26), (41) is in effect also a nonlinear differential equation for crack edge geometry parameter $x_+(\psi)$. Equation (40) is also based on (20), and for $|\psi| \approx \pi/2$, (37) gives

$$\left(\frac{A_+}{A_\Phi}, \frac{B_+}{B_\Phi}\right) = \sqrt{2}\cos\frac{\phi}{2}, \quad \left(\frac{A_-}{A_\Phi}, \frac{B_-}{B_\Phi}\right) = \sqrt{2}\left|\sin\frac{\phi}{2}\right|. \tag{42}$$

A standard table is used to carry out integration in (41). Use of (27a), (28), (D.1) and (D.2) lead to the asymptotic formula

$$S_C \approx \frac{1}{2\mu}\left[\frac{G_\chi \Sigma_{33}}{\pi^2(c_D^2 - 1)}\right]^2 \frac{dx_+}{d\psi}\left[c_D^2(2 - \pi c_D^2) + \frac{\pi}{2}\left(\frac{dx_+}{x_+ \, d\psi}\right)^2\right]. \tag{43}$$

If asymptotic traction behavior ($\chi = \frac{3}{2}$) featured with (27b) is imposed, (43) gives finite S_C for $|\psi| = \pi/2$ when $x_+ \approx O(1/\cos^2\psi)$ as $|\psi| \to \pi/2$. In addition, (D.1) shows that S_C does not give an algebraic equation for $x_+(0)$; see (26).

Illustration: application of energy release (rate) criterion

The strain energy density criterion is generally applied to static situations to ascertain the (possibly) out-of-plane direction that a crack edge segment may move [Sih 1973]. Therefore, planar crack edge behavior

ψ	$0°$	$5°$	$15°$	$30°$	$45°$	$60°$	$75°$	$85°$	$90°$
$c = 0.1$	1.0	0.989	0.95	0.912	0.932	1.051	1.406	2.187	∞
$c = 0.4$	1.0	0.987	0.936	0.881	0.887	0.987	1.319	2.238	∞

Table 1. Ratio $\dfrac{x_+(\psi)}{x_+(0)}$ for various (c, ψ).

in the dynamic steady state is illustrated here in terms of the energy release (rate) criterion. For simplicity,

$$\sigma_{31}^C = \sigma_{32}^C = 0, \quad \sigma_{33}^C = \frac{P\delta(r_0)}{2\pi r_0}, \quad r_0 = \sqrt{x_1^2 + x_2^2}. \tag{44}$$

Here P is a force, so that traction σ_{33}^C is the axially symmetric Dirac function in standard polar coordinates. In view of (21) and (42), criterion (26) reduces to (see (D.2))

$$\frac{\Re}{\sqrt{\mu\rho}} = \frac{2A}{\pi R}\left(\frac{G}{u}\right)^2 c^3 \cos^2 \psi \frac{d}{x_+ d\psi}(x_+ \sin \psi), \quad G = \int_X \frac{\sigma_{33}^C \, dt}{\sqrt{x_+ - t}}. \tag{45}$$

The expression for G is found in Appendix E, and so (45) gives differential equation

$$\frac{\Re}{\sqrt{\mu\rho}} = \left(\frac{P}{2\pi\mu}\right)^2 \frac{A}{R} c^3 \cos^2 \psi \frac{d}{x_+^3 \, d\psi}(x_+ \sin \psi). \tag{46}$$

Here $\Re$ is indeed finite at $|\psi| = \pi/2$ if $x_+ \approx O(1/\sqrt{\cos \psi})$, and, for $\psi = 0$,

$$\frac{\Re}{\sqrt{\mu\rho}} = \left(\frac{P}{2\pi\mu}\right)^2 \frac{A_1 c^3}{R_1 x_+^2(0)}, \quad R_1 = 4A_1 B_1 - K_1^2, \tag{47a}$$

$$A_1 = \sqrt{1 - c^2/c_D^2}, \quad B_1 = \sqrt{1 - c^2}, \quad K_1 = c^2 - 2. \tag{47b}$$

Thus, (44) gives the same asymptotic behavior for $\Re$ as that caused by a distributed traction governed by (18) with $\chi = \frac{3}{2}$. Equation (47a) is algebraic, and readily solved. Invariance of $\Re$ leads to the differential equation, for $\psi \neq 0$,

$$\frac{1}{x_+^3} \frac{dx_+}{d\psi} = \frac{A_1 R}{A R_1 \cos^2 \psi} \frac{1}{x_+^2(0)}. \tag{48}$$

Separation of variables (x_+, ψ) is possible in (48), and for $0 < \psi < \pi/2$ leads to

$$\frac{x_+^2(0)}{x_+^2(\psi)} = \frac{2A_1}{R_1} \sin^2 \psi \int_\psi^{\pi/2} \frac{d\varphi}{\sin^3 \varphi} \frac{R}{A \cos^2 \varphi}. \tag{49}$$

The integration in (49) produces (E.5) in Appendix E. That formula gives the appropriate result that the right-hand side of (49) is unity for $\psi = 0$, and behaves as $\cos \psi$ for $\psi \to \pi/2$. Case $-\pi/2 < \psi < 0$ also gives the right-hand side of (E.5), a result that in light of symmetry is also appropriate.

Sample calculation: energy release (rate) criterion

For a solid characterized by $c_D = 2$ and $c_R = 0.932$, (49) and (E.5) are used to calculate dimensionless ratio $x_+(\psi)/x_+(0)$ for $c = 0.1$ and $c = 0.4$ for values $0 \leq \psi \leq 90°$. The results appear in Table 1. Use

c	0.1	0.2	0.3	0.4	0.5	0.6	0.7	0.8
$\beta_1(c)$	0.259	0.3706	0.4631	0.5512	0.6442	0.7534	0.901	1.1579

Table 2. Dimensionless parameter $\beta_1(c)$, $c_R = 0.932$. Note: $\beta_1(0) = \beta_1(c_R) = 0$.

of (4) in (47a) gives a relation in terms of three dimensionless quantities as

$$\sqrt{\Re/PV_S}\left[\sqrt{\mu/P}\,x_+(0)\right] = \frac{\beta_1(c)}{2\pi}, \quad \beta_1(c) = c\sqrt{cA_1/R_1}. \tag{50}$$

Parameter $\beta_1(c)$ defines, therefore, variation in $x_+(0)$ with respect to (dimensionless) crack translation speed c, and calculations are given in Table 2. Combining the entries for $c = 0.1$ and $c = 0.4$ with Table 1 entries leads to schematics of crack edge contour C for $(x_1, x_2) > 0$ ($x > 0$, $0 < \psi < 90°$) in Figure 2. Both contours tend to the rectilinear, but are perturbed by a smooth indentation near the point force location (denoted by $\times$). It was noted in light of (43) that the strain energy density criterion [Sih 1973] predicts larger values of contour parameter x_+ for $|\psi| \approx \pi/2$ than those predicted by energy release (rate) [Freund 1990]. In view of Figure 2 this implies that the crack edge contour may deviate even more from lines that tend to the rectilinear.

Some comments

This study has produced equations for the radial measure $x_+(\psi)$ from a point on the crack surface to points on the crack edge. Solutions, therefore, define the crack contour. Such equations follow from the criterion for brittle crack growth imposed, and here energy release (rate) and strain energy density are illustrated. Nonlinear first-order differential equations arise in both cases. The strain energy density result is more complicated, because of nonlinearity in both the radial measure and its first derivative.

The case of compressive forces applied to corresponding points on the two crack surfaces is illustrated on the basis of energy release (rate). An analytic solution of the equation, and related calculations, show
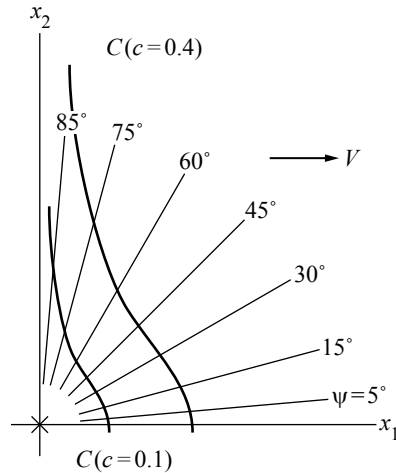
Figure 2. Schematic of crack edge contour, C (drawn to scale).

that the crack contour consists of lines that tend to the rectilinear at great distances from the point forces, but exhibit a pronounced indentation near them. The contours are sensitive to crack growth rate.

The 3D results of this paper are obtained on the assumption that crack growth achieves a dynamic steady state. Nevertheless, they may allow insight into aspects of brittle fracture response that do not arise in a 2D study. On a related note, the analytic results in this paper make use of a "hybrid" form: Cartesian fields are expressed in terms of quasipolar coordinates in the crack plane. The advantages of this are: (a) the solution can be obtained from classical singular integral equations, and (b) some factorization of x_+ and its derivative $dx_+/d\psi$ in the nonlinear equation is possible.

One difficulty, however, with the "hybrid" form is that description of solution behavior in terms of the three fracture modes must be extracted. When crack contour is known or a 2D study is involved, imposition of local Cartesian coordinates that are, respectively, normal to the crack plane, and normal and tangential to the crack edge, is feasible; see, e.g., [Freund 1990]. Based on experience [Brock 2012] with undefined area contours, the author decided that such a coordinate choice could prove to be an analytical stumbling block.

Appendix A

For $x_3 \geq 0(+)$ and $x_3 \leq 0(-)$, respectively,

$$c^2 p_1^2 U^\pm = -\frac{K\hat{U}_3}{2A} \pm (p_1\hat{U}_1 + p_2\hat{U}_2), \tag{A.1a}$$

$$c^2 p_1^2 V_1^\pm = p_1 B\hat{U}_3 \pm \left[c^2 p_1^2 \frac{\hat{U}_1}{2} - p_1(p_1\hat{U}_1 + p_2\hat{U}_2) \right], \tag{A.1b}$$

$$c^2 p_1^2 V_2^\pm = p_2 B\hat{U}_3 \pm \left[c^2 p_1^2 \frac{\hat{U}_2}{2} - p_2(p_1\hat{U}_1 + p_2\hat{U}_2) \right]. \tag{A.1c}$$

In (A.1), (B, A) are defined by (9), and

$$K = c^2 p_1^2 - 2D. \tag{A.2}$$

Transforms of traction for $x_3 = 0$ are given by

$$\frac{\hat{\sigma}_{33}}{\mu} = -\frac{\hat{U}_3}{2Ac^2 p_1^2}(4DAB + K^2), \tag{A.3a}$$

$$\frac{\hat{\sigma}_{31}}{\mu} = \frac{p_1}{Bc^2 p_1^2}(K - 2AB)(p_1\hat{U}_1 + p_2\hat{U}_2) + \frac{1}{2B}[(p_2^2 - c^2 p_1^2)\hat{U}_1 + p_1 p_2\hat{U}_2], \tag{A.3b}$$

$$\frac{\hat{\sigma}_{32}}{\mu} = \frac{p_2}{Bc^2 p_1^2}(K - 2AB)(p_1\hat{U}_1 + p_2\hat{U}_2) + \frac{1}{2B}[(p_1^2 - c^2 p_1^2)\hat{U}_2 + p_1 p_2\hat{U}_1]. \tag{A.3c}$$

Appendix B

Consider integrals involving real constants (X, Y) over the entire $\text{Im}(p)$-axis

$$\frac{1}{2\pi i} \int |p| \left(\frac{\sqrt{-p}}{\sqrt{p}}, 1 \right) \exp(pX - Y\sqrt{-p}\sqrt{p}) \frac{dp}{p} \quad (Y \geq 0). \tag{B.1}$$

As noted in connection with (11) and (12), $\text{Re}(\sqrt{\pm p}) \geq 0$ in the p-plane with branch cuts $\text{Im}(p) = 0$, $\text{Re}(p) < 0$ and $\text{Im}(p) = 0$, $\text{Re}(p) > 0$ respectively. In particular, for $\text{Re}(p) = 0+$ and, respectively, $\text{Im}(p) = q > 0$ and $\text{Im}(p) = q < 0$,

$$\sqrt{-p} = \left|\frac{q}{2}\right|^{1/2}(1 \mp i), \quad \sqrt{p} = \left|\frac{q}{2}\right|^{1/2}(1 \pm i). \tag{B.2}$$

Use of (B.2) reduces (B.1) to

$$\frac{1}{i\pi} \int_0^\infty (\sin qX, \cos qX) \exp(-Yq)\, dq. \tag{B.3}$$

Integration of (B.3) gives

$$\frac{1}{i\pi}\left[\frac{X}{X^2 + Y^2}, \frac{Y}{X^2 + Y^2}\right] = \frac{1}{i\pi}[\text{Re, Im}]\frac{1}{X - iY}. \tag{B.4}$$

It is noted that

$$\frac{1}{\pi}\frac{Y}{X^2 + Y^2} \to \delta(X) \quad (Y \to 0+). \tag{B.5}$$

Here δ is the Dirac function.

Appendix C

For $x_3 = 0$, $X_- < x < X_+$, $\psi \in \Psi$, i.e., $x_3 = 0$, $(x_1, x_2) \in C$,

$$\frac{\sigma_{33}}{2\mu} = -\frac{G_3}{\pi}(\text{vp}) \int_X \frac{\partial U_3}{\partial x}\frac{d\xi}{\xi - x}, \tag{C.1a}$$

$$\frac{\sigma_{31}}{2\mu} = -\frac{G_1}{\pi}(\text{vp}) \int_X \frac{\partial U_1}{\partial x}\frac{d\xi}{\xi - x} - \frac{G_{12}}{\pi}(\text{vp}) \int_X \frac{\partial U_2}{\partial x}\frac{d\xi}{\xi - x}, \tag{C.1b}$$

$$\frac{\sigma_{32}}{2\mu} = -\frac{G_{21}}{\pi}(\text{vp}) \int_X \frac{\partial U_1}{\partial x}\frac{d\xi}{\xi - x} - \frac{G_2}{\pi}(\text{vp}) \int_X \frac{\partial U_2}{\partial x}\frac{d\xi}{\xi - x}. \tag{C.1c}$$

In (C.1), $U_k = U_k(\xi, \psi)$, (vp) signifies principal value integration, and

$$G_1 = B + \frac{M}{Bc^2}, \quad G_2 = B + \frac{M}{Bc^2}\tan^2\psi, \quad G_{12} = G_{21} = \frac{M}{Bc^2}\tan\psi, \tag{C.2a}$$

$$G_3 = \frac{R}{Ac^2\cos^2\psi}. \tag{C.2b}$$

Terms in (C.2) are defined by (13b) and

$$M = 2N + c^2\cos^2\psi, \quad N = 2AB + K, \quad R = 4AB - K^2. \tag{C.3}$$

Appendix D

If $(\sigma_{31}^C, \sigma_{32}^C) = 0$ and $(X_- \to -\infty, |\psi| < \pi/2)$, strain for $r \approx 0$ is obtained from (44) as

$$e_{11} \approx -\frac{\cos\psi}{\pi^2\sqrt{2r}}\frac{G}{R}\left(K\frac{A_+}{A_\Phi} + 2AB\frac{B_+}{B_\Phi}\right)\frac{d}{x_+\,d\psi}(x_+\sin\psi), \tag{D.1a}$$

$$e_{22} \approx \frac{\sin\psi}{\pi^2\sqrt{2r}}\frac{G}{R}\left(K\frac{A_+}{A_\Phi} + 2AB\frac{B_+}{B_\Phi}\right)\frac{d}{x_+\,d\psi}(x_+\cos\psi), \tag{D.1b}$$

$$e_{33} \approx -\frac{A}{\pi^2\sqrt{2r}}\frac{G}{R}\left(KA\frac{A_+}{A_\Phi} + 2B\frac{B_+}{B_\Phi}\right), \tag{D.1c}$$

$$e_{23} \approx \frac{1}{2\pi^2\sqrt{2r}}\frac{G}{R}\left(K\frac{A_-}{A_\Phi} + 2B^2\frac{B_-}{B_+}\right)\sin\psi + \text{sgn}(\phi)\left(K\frac{A_-}{A_\Phi} + 2AB\frac{B_-}{B_\Phi}\right)\frac{d}{x_+\,d\psi}(x_+\cos\psi), \tag{D.1d}$$

$$e_{31} \approx \frac{1}{2\pi^2\sqrt{2r}}\frac{G}{R}\left(K\frac{A_-}{A_\Phi} + 2B^2\frac{B_-}{B_\Phi}\right)\cos\psi - \text{sgn}(\phi)\left(K\frac{A_-}{A_\Phi} + 2AB\frac{B_-}{B_\Phi}\right)\frac{d}{x_+\,d\psi}(x_+\sin\psi), \tag{D.1e}$$

$$e_{12} \approx \frac{1}{2\pi^2\sqrt{2r}}\frac{G}{R}\left(K\frac{A_+}{A_\Phi} + 2AB\frac{B_+}{B_\Phi}\right)\cos\psi\frac{d}{x_+\,d\psi}(x_+\cos\psi) - \sin\psi\frac{d}{x_+\,d\psi}(x_+\sin\psi). \tag{D.1f}$$

The factor G is given by

$$G = \int_X \frac{\sigma_{33}^C\,dt}{\sqrt{x_+ - t}}. \tag{D.2}$$

Appendix E

In terms of quasipolar coordinates (x, ψ), (41) gives

$$\sigma_{33}^C = P\frac{\delta(x)}{\pi|x|}, \quad |\psi| < \pi/2. \tag{E.1}$$

Function G in (42) is obtained in terms of representation

$$\sigma_{33}^C = P\frac{\epsilon}{\pi^2|x|(x^2 + \epsilon^2)} \quad (\epsilon \to 0). \tag{E.2}$$

Function $F_G(z)$ in the complex z-plane, where $x = \text{Re}(z)$, is defined as

$$F_G(z) = \frac{1}{\sqrt{z^2 - \epsilon_0^2}(z^2 + \epsilon^2)\sqrt{z - x_+}} \quad (\epsilon_0 \approx 0). \tag{E.3}$$

Here $F_G \approx O(z^{-3})$, $|z| \to \infty$ and exhibits branch cuts on the $\text{Re}(z)$-axis with branch points $z = (\pm\epsilon_0, x_+)$, and poles $z = \pm i\epsilon$. Thus integration over a closed contour that includes a portion $|z| \to \infty$, but excludes

the poles and branch cuts, can be performed by residue theory. Setting $\epsilon_0 = 0$ then leads to

$$G = \frac{P}{\pi \alpha \sqrt{2(1+\alpha)}} \frac{1}{x_+^{3/2}}, \quad \alpha = \sqrt{1 + \epsilon^2/x_+^2}, \tag{E.4a}$$

$$G = \frac{P}{2\pi x_+^{3/2}} \quad (\epsilon \to 0). \tag{E.4b}$$

Use of (E.4) leads to the integral in (49). Introduction of integration variable $u = c \cos \varphi$ gives a form that is readily carried out as

$$\int_\psi^{\pi/2} \frac{R \sin^2 \psi}{A \cos^2 \varphi} \frac{d\varphi}{\sin^3 \varphi} = \left(2B - \frac{K_1^2 A}{2A_1^2}\right) \cos \psi + 4(A - B) \frac{\sin^2 \psi}{\cos \psi}$$

$$+ \frac{2K_1}{A_1}\left(1 + \frac{K_1}{A_1^2}\right) \ln\left|\frac{A + A_1 \cos \psi}{A - A_1 \cos \psi}\right| \sin^2 \psi + 2\left(B_1 + \frac{1}{2B_1}\right) \ln\left|\frac{B + B_1 \cos \psi}{B - B_1 \cos \psi}\right| \sin^2 \psi. \tag{E.5}$$

The right-hand side behaves as $\cos \psi$ for $\psi = \pi/2$, and for $\psi = 0$ gives $R_1/2A_1$.

References

[Achenbach 1975] J. D. Achenbach, *Wave propagation in elastic solids*, North-Holland Series in Applied Mathematics and Mechanics, Elsevier, Amsterdam, 1975.

[Achenbach and Brock 1973] J. D. Achenbach and L. M. Brock, "On quasistatic and dynamic fracture", pp. 529–541 in *Proceedings of an international conference on dynamic crack propagation*, edited by G. C. Sih, Springer Netherlands, 1973.

[Brock 1999] L. M. Brock, "Effects of mixed-mode and crack surface convection in rapid crack growth in coupled thermoelastic solids", *Journal of Applied Mechanics* **67**:1 (10/12 1999), 59–65.

[Brock 2012] L. M. Brock, "Two cases of rapid contact on an elastic half-space: sliding ellipsoidal die, rolling sphere", *Journal of mechanics of materials and structures* **7**:5 (2012), 469–483.

[Brock 2014a] L. M. Brock, "The rigid die on a half-space with thermal relaxation and convection: influence of sliding speed, die temperature, and geometry", *Journal of Thermal Stresses* **37**:7 (2014), 832–851.

[Brock 2014b] L. M. Brock, "Sliding of a cup-shaped die on a half-space: influence of thermal relaxation, convection and die temperature", *Journal of mechanics of materials and structures* **9**:3 (2014), 347–363.

[Brock 2015] L. M. Brock, "Rapid sliding on a thermoelastic half-space: rigid die with two contact surfaces", *Journal of thermal stresses* (2015).

[Freund 1990] L. B. Freund, *Dynamic fracture mechanics*, Cambridge Monographs on Mechanics and Applied Mathematics, Cambridge University Press, 1990.

[Griffith 1921] A. A. Griffith, "The phenomena of rupture and flow in solids", *Philosophical Transactions of the Royal Society of London A: Mathematical, Physical and Engineering Sciences* **221**:582–593 (1921), 163–198.

[Sih 1973] G. C. Sih, "Energy-density concept in fracture mechanics", *Engineering Fracture Mechanics* **5**:4 (1973), 1037–1040.

[Sneddon 1972] I. N. Sneddon, *The use of integral transforms*, McGraw-Hill, New York, 1972.

LOUIS MILTON BROCK: louis.brock@uky.edu
Department of Mechanical Engineering, University of Kentucky, 265 RGAN, Lexington, KY 40506-0503, United States

msp

MECHANICAL DEGRADATION OF
NATURAL FIBER REINFORCED COMPOSITE MATERIALS
UNDER CONSTRAINED SWELLING

YIHUI PAN AND ZHENG ZHONG

Natural fiber reinforced composite materials (NFRCMs) have found more and more applications because of their excellent performances over traditional fiber reinforced composites. However, mechanical properties of these materials may be dramatically degraded in a humid environment, whether subject to mechanical loading or not. A nonlinear constitutive model is established for unidirectional natural fiber reinforced composites under large swelling deformation based on nonequilibrium thermodynamics, in which an internal variable is incorporated in the Helmholtz free energy to consider the irreversible energy dissipation induced by moisture absorption. The Helmholtz free energy is further decomposed into the base free energy of the isotropic matrix, the reinforcing energy of fiber stretching and the free energy of volume expansion. Two kinds of reinforcing energy (the I_4-dependent model and the I_5-dependent model) are employed to predict the degradation of the elastic modulus for the cases of free swelling and constrained swelling. It is found that the predictions from these two models are identical for the case of free swelling and agree well with available experimental data. As for the case of constrained swelling, these two models yield obviously different results.

1. Introduction

Natural fiber reinforced composite materials (NFRCMs) have been drawing great attention due to their excellent advantages over glass or other traditional fiber reinforced composites. For example, natural fibers possess high specific strength and modulus because of their light weight [Athijayamani et al. 2009; Medina et al. 2009]. Moreover, they are environmentally friendly with biodegradable properties. Hence, NFRCMs have found more and more applications in the aerospace and automobile industries. In spite of so many advantages, there are still some disadvantages to these new composite materials, such as moisture absorption and weak adhesion to hydrophobic matrices [Sgriccia et al. 2008]. The worst is the mechanical degradation of NFRCMs induced by moisture absorption in a humid environment, especially losses of tensile and shear moduli.

Natural fibers are usually hydrophilic and have a porous structure [Lu et al. 2003] which can transport large amounts of water from an external humid environment [Espert et al. 2004]. There are two main causes for the mechanical degradation of NFRCMs induced by moisture absorption. First, water uptake will cause natural fibers to swell and induce fiber aging, during which natural fibers gradually soften due to a loss of elastic moduli [Song et al. 2011]. Second, interfaces between the matrix and the fibers of

NFRCMs will be continuously damaged by moisture absorption [Dhakal et al. 2007], so that in the worst case, the interfaces would be totally damaged and the fibers completely pulled out [Sydenstricker et al. 2003], losing their reinforcing effects on the matrix.

Since moisture absorption in a humid environment is inevitable, it is significant to study moisture absorption and its effects on the mechanical properties of NFRCMs. However, Fick's diffusion law fails to describe the process of moisture absorption because the permeability of water diffusion is no longer a constant, which changes with interfacial damage and fiber aging during moisture absorption [Hu et al. 2010].

The moisture-induced swelling deformation of NFRCMs was originally studied by Tsai et al. [2004] based on a finite elasticity description, considering a finite strain flexure in an isotropic rectangular block. Then the theoretical framework was applied to fiber reinforced composite materials with absorbent matrix and hydrophobic fibers [Demirkoparan and Pence 2007a; 2007b; 2008; Fang et al. 2011].

The swelling-induced mechanical degradation of polymeric materials is another research topic of common interest. Baek and Pence [2009] developed a constitutive model considering the swelling and mechanical degradation of fiber reinforced composites based on the energy dissipation framework [Rajagopal and Srinivasa 2004; Rajagopal et al. 2007; Karra and Rajagopal 2012]. The purely mechanical induced degradation of fiber reinforced composites was also studied [Baek and Pence 2011].

In [Pan and Zhong 2014b], large swelling deformation and nonlinear mechanical responses of natural fiber reinforced composites are taken into account by adopting a special form of the Helmholtz free energy which depends on four scalar strain invariants reflecting the deformation characteristics of transverse isotropy of unidirectional fiber reinforced composites [Qiu and Pence 1997] and an internal variable describing the moisture absorption process. This model is referred to as the I_4-dependent model in the present paper.

In the present paper, instead of using the I_4-dependent model, another model for reinforcing energy which was studied in detail by Merodio and Ogden [2005] is employed to consider the unidirectional reinforcement of natural fibers in a neo-Hookean matrix, which is called the I_5-dependent model. The degradation of elastic modulus is predicted for the cases of free swelling and constrained swelling based on the newly developed model and compared with those obtained from the I_4-dependent model. It is found that the predictions from these two models are identical for the case of free swelling and deviate obviously from each other for the case of constrained swelling.

This paper is organized as follows. In Section 2, a general constitutive model is described based on nonequilibrium thermodynamics. Then in Section 3 we specialize the I_5-dependent model to study the mechanical degradation of NFRCMs under free swelling and constrained swelling. In Section 4, results are obtained for a unidirectional sisal fiber reinforced benzylated wood based on the I_5-dependent model and compared with those from the I_4-dependent model. Finally, in Section 5, we draw the conclusions.

2. Theoretical formulation

2.1. *Deformation decomposition.* Consider a natural fiber reinforced composite in a humid environment. The deformation gradient is defined by $\boldsymbol{F} = \partial \boldsymbol{x}/\partial \boldsymbol{X}$, where $\boldsymbol{X}$ represents the position vector of a material particle in the initial dry and undeformed configuration, and $\boldsymbol{x}$ is the corresponding position vector of this

particle in the current swollen and deformed configuration, from which the right and the left Cauchy–Green strain tensors are given as $\boldsymbol{C} = \boldsymbol{F}^T \cdot \boldsymbol{F}$ and $\boldsymbol{b} = \boldsymbol{F} \cdot \boldsymbol{F}^T$. Here the dot product "·" denotes a contraction (inner product) over one index between two tensors (or vectors), and the superscript "T" denotes the transpose of a tensor.

If we adopt a multiplicative decomposition of the deformation gradient into volume-changing (dilational) and volume-preserving (distortional) parts [Holzapfel 2000], then we have

$$\boldsymbol{F} = J^{1/3} \bar{\boldsymbol{F}}, \tag{1}$$

where $J = \det \boldsymbol{F}$ is the volume ratio and $\bar{\boldsymbol{F}}$ is called the modified deformation gradient tensor. Accordingly, the modified right and left Cauchy–Green strain tensors can be defined as $\bar{\boldsymbol{C}} = \bar{\boldsymbol{F}}^T \cdot \bar{\boldsymbol{F}}$ and $\bar{\boldsymbol{b}} = \bar{\boldsymbol{F}} \cdot \bar{\boldsymbol{F}}^T$. Here we refer to a case as free swelling when $\bar{\boldsymbol{C}} = \boldsymbol{I}$ (or equivalently $\bar{\boldsymbol{b}} = \boldsymbol{I}$) and otherwise as constrained swelling if $\bar{\boldsymbol{C}} \neq \boldsymbol{I}$ (or equivalently $\bar{\boldsymbol{b}} \neq \boldsymbol{I}$), with $\boldsymbol{I}$ being the second-order identity tensor.

Furthermore, three principal invariants of $\boldsymbol{C}$ (also $\boldsymbol{b}$) are given as

$$I_1 = \mathrm{tr} \boldsymbol{C} = J^{2/3} \mathrm{tr} \bar{\boldsymbol{C}} = J^{2/3} \bar{I}_1, \tag{2a}$$

$$I_2 = \tfrac{1}{2}[(\mathrm{tr} \boldsymbol{C})^2 - \mathrm{tr}(\boldsymbol{C}^2)] = \tfrac{1}{2} J^{4/3}[(\mathrm{tr} \bar{\boldsymbol{C}})^2 - \mathrm{tr}(\bar{\boldsymbol{C}}^2)] = J^{4/3} \bar{I}_2, \tag{2b}$$

$$I_3 = \det \boldsymbol{C} = J^2, \tag{2c}$$

where the notations "tr" and "det" denote, respectively, the trace and the determinant of a tensor, and $\bar{I}_1$ and $\bar{I}_2$ are the first and the second principal invariants of $\bar{\boldsymbol{C}}$, with the third principal invariant $\bar{I}_3 = 1$.

2.2. Material model.

For a transversely isotropic material, with the axis of transverse isotropy defined by a unit vector $\boldsymbol{a}_0$ in the initial configuration, the Helmholtz free energy depends not only on the deformation tensor $\boldsymbol{C}$, but also the second-order tensor $\boldsymbol{a}_0 \otimes \boldsymbol{a}_0$, which can be written as [Moon and Spencer 1988; Spencer 1984]

$$W = W(\boldsymbol{C}, \boldsymbol{a}_0 \otimes \boldsymbol{a}_0) = W(\bar{I}_1, \bar{I}_2, J, \bar{I}_4, \bar{I}_5), \tag{3}$$

where

$$\bar{I}_4 = \boldsymbol{a}_0 \cdot \bar{\boldsymbol{C}} \cdot \boldsymbol{a}_0 = \lambda_f^2, \quad \bar{I}_5 = \boldsymbol{a}_0 \cdot (\bar{\boldsymbol{C}})^2 \cdot \boldsymbol{a}_0, \tag{4}$$

and $\lambda_f = \sqrt{\bar{I}_4}$ is the fiber stretch.

As special cases, (3) reduces to the I_4-dependent model [Qiu and Pence 1997]

$$W = W(\bar{I}_1, \bar{I}_2, J, \bar{I}_4) \tag{5}$$

when the Helmholtz free energy is independent of $\bar{I}_5$, or the I_5-dependent model [Merodio and Ogden 2005]

$$W = W(\bar{I}_1, \bar{I}_2, J, \bar{I}_5) \tag{6}$$

when the Helmholtz free energy is independent of $\bar{I}_4$.

Furthermore, the free energy W is assumed to be decomposed into three parts:

$$W = W_m(\bar{I}_1, \bar{I}_2) + W_f(\bar{I}_4, \bar{I}_5) + W_v(J). \tag{7}$$

The first term in the right-hand side of (7) represents the base Helmholtz free energy of the isotropic matrix induced by mechanical loading, while the second term is the reinforcing energy associated with

the stretching of the embedded fibers under the mechanical loading and the last term stands for the free energy of volume expansion induced by fiber swelling.

2.3. *Internal variable.* Upon moisture absorption, the interface between the matrix and the fiber of NFRCMs may be damaged [Dhakal et al. 2007; Sgriccia et al. 2008]. At the same time, the fiber also undergoes aging due to large amounts of water absorbed by natural fibers [Espert et al. 2004; Gao et al. 2011; Song et al. 2011]. Since all these processes are thermodynamically irreversible with energy dissipation, an internal variable is tentatively introduced to account for the effect of the composite microstructure change induced by moisture absorption. The internal variable α varies from 0 to 1 such that $\alpha = 0$ corresponds to the initial dry state and $\alpha = 1$ represents the fully saturated state. It is known that in the dry state, the composite maintains its initial mechanical properties. As α evolves from 0 to 1, the mechanical properties, such as Young's modulus, gradually degrade due to moisture absorption. Such degradation effects are reflected by the softening of the matrix and the reinforcement. Hence, the Helmholtz free energy for this transversely isotropic composite should also depend on the internal variable α, so that (7) is further modified to give

$$W = W_m(\alpha, \bar{I}_1, \bar{I}_2) + W_f(\alpha, \bar{I}_4, \bar{I}_5) + W_v(J). \tag{8}$$

Here the internal variable α acts as an additional independent variable in (8).

Note that Baek and Pence [2009; 2011] used two internal variables to describe the mechanical degradation of matrix and the fiber, respectively. In this paper, only one internal variable is employed for natural fiber composites, since both the interface damage and the fiber degradation are treated as a unified thermodynamic process induced by moisture absorption. This treatment simplifies the solution of the evolution of the internal variable and also gives a sufficient accuracy in describing the mechanical degradation of natural fiber composites as illustrated in Section 4.

Since the internal variable α is related to the absorption process of the natural fiber, the volume ratio J of the composite is assumed to be a function of α, i.e.,

$$J = J(\alpha). \tag{9}$$

For an incompressible composite without moisture absorption, we have $J = 1$. Furthermore, a linear relation between J and α can be derived based on the assumption of molecular incompressibility [Hong et al. 2008] as

$$J = 1 + \theta\alpha, \tag{10}$$

where θ is the equilibrium volume fraction of water in the composites defined with respect to the initial dry configuration, and can be derived from experiments. Equation (10) is an ideal mixing approximation of the moisture absorption process that the swelling volume is the volume sum of the dry composite and the water uptake.

The constraint $J = J(\alpha)$ can be accounted for by introducing a Lagrange multiplier term into the Helmholtz free energy, so that

$$W = W_m(\alpha, \bar{I}_1, \bar{I}_2) + W_f(\alpha, \bar{I}_4, \bar{I}_5) + W_v(J) + \Pi[J - J(\alpha)], \tag{11}$$

where the Lagrange multiplier term Π is interpreted as an osmotic pressure and could be determined from boundary conditions.

2.4. *Thermodynamics.* When the composite is subject to mechanical loading and a humid environment, there are two mechanisms doing work on the composite: mechanical loading and chemical potential of the external environment. During this process, the Clausius–Duhem inequality

$$J\boldsymbol{\sigma} : \boldsymbol{d} + \mu r + \mu\dot{\alpha} - \boldsymbol{q} \cdot \nabla\mu \geq \dot{W} \tag{12}$$

holds, where $\boldsymbol{\sigma}$ is the Cauchy stress, μ is the chemical potential, r stands for the internal source of water (however, in most cases there is no internal source and $r = 0$), $\boldsymbol{q}$ represents the water flowing out through the element area, and the rate of deformation tensor is defined as

$$\boldsymbol{d} = \tfrac{1}{2}(\dot{\boldsymbol{F}} \cdot \boldsymbol{F}^{-1} + \boldsymbol{F}^{-T} \cdot \dot{\boldsymbol{F}}^{T}). \tag{13}$$

From (11), the rate of the Helmholtz free energy $\dot{W}$ is calculated as

$$\dot{W} = 2\mathbb{P} : [\omega_1\bar{\boldsymbol{b}} + \omega_2\bar{\boldsymbol{b}}^2 + \omega_4\bar{\boldsymbol{a}} \otimes \bar{\boldsymbol{a}} + \omega_5(\bar{\boldsymbol{a}} \otimes \bar{\boldsymbol{b}} \cdot \bar{\boldsymbol{a}} + \bar{\boldsymbol{b}} \cdot \bar{\boldsymbol{a}} \otimes \bar{\boldsymbol{a}})] : \boldsymbol{d} + J\omega_3\boldsymbol{I} : \boldsymbol{d} + Y^{\alpha}\dot{\alpha}, \tag{14}$$

with

$$
\begin{aligned}
\omega_1 &= \frac{\partial W_m}{\partial \bar{I}_1} + \bar{I}_1 \frac{\partial W_m}{\partial \bar{I}_2}, & \omega_2 &= -\frac{\partial W_m}{\partial \bar{I}_2}, & \omega_3 &= \frac{\partial W_v}{\partial J} + \Pi, \\
\omega_4 &= \frac{\partial W_f}{\partial \bar{I}_4}, & \omega_5 &= \frac{\partial W_f}{\partial \bar{I}_5}, & Y^{\alpha} &= \frac{\partial (W_m + W_f)}{\partial \alpha},
\end{aligned}
\tag{15}
$$

where $\boldsymbol{b}$ and $\bar{\boldsymbol{b}}$ are the left Cauchy–Green strain tensors corresponding to $\boldsymbol{F}$ and $\bar{\boldsymbol{F}}$, respectively, $\boldsymbol{I}$ is the second-order identity tensor, the projection tensor $\mathbb{P} = \mathbb{I} - (\boldsymbol{I} \otimes \boldsymbol{I})/3$ is defined with respect to the current configuration, $\mathbb{I}$ is the fourth-order identity tensor, $\bar{\boldsymbol{a}} = \bar{\boldsymbol{F}} \cdot \boldsymbol{a}_0$ stands for the fiber direction after mechanical loading, and Y^{α} is the thermodynamic force conjugate to the thermodynamic flow $\dot{\alpha}$.

Substituting (14) into (12) when $r = 0$, we have

$$(J\boldsymbol{\sigma} - \mathbb{P} : \bar{\boldsymbol{\sigma}} - J\boldsymbol{\sigma}^{S}) : \boldsymbol{d} + (\mu - Y^{\alpha})\dot{\alpha} - \boldsymbol{q} \cdot \nabla\mu \geq 0, \tag{16}$$

where

$$
\begin{aligned}
\bar{\boldsymbol{\sigma}} &= 2[\omega_1\bar{\boldsymbol{b}} + \omega_2\bar{\boldsymbol{b}}^2 + \omega_4\bar{\boldsymbol{a}} \otimes \bar{\boldsymbol{a}} + \omega_5(\bar{\boldsymbol{a}} \otimes \bar{\boldsymbol{b}} \cdot \bar{\boldsymbol{a}} + \bar{\boldsymbol{b}} \cdot \bar{\boldsymbol{a}} \otimes \bar{\boldsymbol{a}})], \\
\boldsymbol{\sigma}^{S} &= \omega_3\boldsymbol{I}.
\end{aligned}
\tag{17}
$$

In the thermodynamic inequality (16), the first and the second terms represent, respectively, the energy dissipation caused by external forces and chemical potential. If we assume that the equilibriums of mechanical loading and chemical potential are achieved instantaneously, then

$$\boldsymbol{\sigma} = J^{-1}\mathbb{P} : \bar{\boldsymbol{\sigma}} + \boldsymbol{\sigma}^{S}, \tag{18}$$

where $J^{-1}\mathbb{P} : \bar{\boldsymbol{\sigma}}$ and $\boldsymbol{\sigma}^{S}$ are the Cauchy stresses due to isochoric elastic deformation and volumetric swelling deformation, respectively, and

$$\mu = Y^{\alpha}, \tag{19}$$

which relates the chemical potential to the variation of the Helmholtz free energy with the internal variable.

The third term stands for the energy dissipation induced by water transport, which requires that the following inequality should hold:

$$\boldsymbol{q} \cdot \nabla \mu \leq 0. \tag{20}$$

Hence, the energy dissipation caused by the thermodynamic flow $\dot{\alpha}$ with its conjugate force Y^{α} is given as

$$\Xi = -Y^{\alpha} \dot{\alpha}. \tag{21}$$

3. Mechanical degradation due to moisture absorption

In this section, the theoretical formulations developed above are specialized with the I_5-dependent model to study the mechanical degradation of NFRCMs under constrained swelling and free swelling.

3.1. *Moisture absorption.* To study the influence of moisture absorption on the mechanical properties of NFRCMs, for simplicity and without loss of generality we study a cubic NFRCM sample exposed to a humid environment and simultaneously subjected to (possible) mechanical loading, corresponding to the case of constrained swelling. The isochoric elastic deformation is described by three principal stretches $\bar{\lambda}_1, \bar{\lambda}_2, \bar{\lambda}_3$ of the deformation gradient $\bar{\boldsymbol{F}}$, with

$$\bar{I}_1 = \bar{\lambda}_1^2 + \bar{\lambda}_2^2 + \bar{\lambda}_3^2, \quad \bar{I}_2 = \bar{\lambda}_1^2 \bar{\lambda}_2^2 + \bar{\lambda}_2^2 \bar{\lambda}_3^2 + \bar{\lambda}_3^2 \bar{\lambda}_1^2 \quad \text{and} \quad \bar{I}_3 = (\bar{\lambda}_1 \bar{\lambda}_2 \bar{\lambda}_3)^2 = 1.$$

Considering that the interfaces between the matrix and the fibers are deteriorated gradually due to moisture absorption [Sgriccia et al. 2008], we modify the neo-Hookean model for the isotropic polymer matrix to obtain [Baek and Pence 2009; Karra and Rajagopal 2012]

$$W_m = \tfrac{1}{2} G [1 - \beta_1(c)\alpha](\bar{I}_1 - 3) = \tfrac{1}{2} G [1 - \beta_1(c)\alpha] \Big[\sum_i (\bar{\lambda}_i)^2 - 3 \Big], \tag{22}$$

where G is the initial shear modulus of the matrix, $\beta_1(c)$ is a dimensionless parameter reflecting the influence of the degradation on the matrix, which depends on the fiber content c. Note that the interface damage increases with the fiber content, so that β_1 should be a monotonically increasing function of c. Equation (22) is called the modified neo-Hookean model, which reduces to the original neo-Hookean model if $\alpha = 0$.

If we assume the initial fiber direction is taken along the X_1-axis in the initial configuration, then $\bar{I}_5 = \bar{\lambda}_1^4$, with $\bar{\lambda}_1$ being the fiber stretch induced by mechanical loading. Accordingly, the reinforcing energy based on the I_5-dependent model is given by [Merodio and Ogden 2005]

$$W_f = \tfrac{1}{2} G \bar{\gamma} (\bar{I}_5 - 1)^2 = \tfrac{1}{2} G \bar{\gamma} [(\bar{\lambda}_1)^4 - 1]^2, \tag{23}$$

where $\bar{\gamma}$ is the relative stiffness of the fiber with respect to the matrix, which can be taken as $\bar{\gamma} = c\gamma$ for the first approximation, with γ being a coefficient of proportionality. Further considering the interface damage and the fiber degradation, (23) is modified to the form [Baek and Pence 2009]

$$W_f = \tfrac{1}{2} G \bar{\gamma} (1 - \beta_2 \alpha)[(\bar{\lambda}_1)^4 - 1]^2, \tag{24}$$

where β_2 is a dimensionless constant referred to as the maximum degradation parameter of the fiber. In the case of $\alpha = 0$, the modified reinforcing energy reduces to the original one given by Merodio and

Ogden [2005]. The volume expansion energy W_v induced by the fiber swelling is specified as [Hong et al. 2008]

$$W_v = -G\bar{\gamma} \ln J. \tag{25}$$

With the above specified Helmholtz free energies for the matrix W_m, the reinforcing energy W_f and the volume expansion energy W_v, the constitutive relation of the composite is derived by substituting (10), (22), (24) and (25) into (18), as

$$\sigma_{11} = \tfrac{1}{3}Gd_1(\alpha)[2(\bar{\lambda}_1)^2 - (\bar{\lambda}_2)^2 - (\bar{\lambda}_3)^2] + (\Pi - c\gamma GJ^{-1}) + \tfrac{8}{3}c\gamma Gd_2(\alpha)[(\bar{\lambda}_1)^8 - (\bar{\lambda}_1)^4], \tag{26a}$$

$$\sigma_{22} = \tfrac{1}{3}Gd_1(\alpha)[2(\bar{\lambda}_2)^2 - (\bar{\lambda}_1)^2 - (\bar{\lambda}_3)^2] + (\Pi - c\gamma GJ^{-1}) + \tfrac{4}{3}c\gamma Gd_2(\alpha)[-(\bar{\lambda}_1)^8 + (\bar{\lambda}_1)^4], \tag{26b}$$

$$\sigma_{33} = \tfrac{1}{3}Gd_1(\alpha)[2(\bar{\lambda}_3)^2 - (\bar{\lambda}_1)^2 - (\bar{\lambda}_2)^2] + (\Pi - c\gamma GJ^{-1}) + \tfrac{4}{3}c\gamma Gd_2(\alpha)[-(\bar{\lambda}_1)^8 + (\bar{\lambda}_1)^4], \tag{26c}$$

with

$$d_1(\alpha) = (1+\theta\alpha)^{-1}(1-\beta_1\alpha) \quad \text{and} \quad d_2(\alpha) = (1+\theta\alpha)^{-1}(1-\beta_2\alpha). \tag{27}$$

Here $d_1(\alpha)$ and $d_2(\alpha)$ are regarded as degradation functions describing, respectively, the degradation of the shear modulus G and the relative stiffness $\bar{\gamma}$.

To derive the evolution equation of α, the dissipation function Ξ in (21) should be specified. Here we take the form that has been successfully used to describe material degradations from different dissipation mechanisms, e.g., thermo-oxidization, hydrolysis and swelling [Rajagopal and Srinivasa 2004; Rajagopal et al. 2007; Baek and Pence 2009; Soares et al. 2009; Karra and Rajagopal 2012]:

$$\Xi(\alpha, \dot{\alpha}) = \frac{\bar{D}\dot{\alpha}^{(n+1)/n}}{(1-\alpha)^{1/n}}, \tag{28}$$

where n is a rate-sensitive index and $\bar{D}$ is a parameter governing the speed of energy dissipation. To further reflect the effect of fiber volume fraction on the swelling speed, $\bar{D}$ is assumed to be proportional to the fiber content, so that $\bar{D} = cD$ with D being a coefficient of proportionality [Pan and Zhong 2014a; 2014b]. Then a combination of (21) with (28) yields

$$\left(\frac{\dot{\alpha}}{1-\alpha}\right)^{1/n} = \frac{G\beta_1}{2cD}\Big[\sum_i(\bar{\lambda}_i)^2 - 3\Big] + \frac{\gamma G\beta_2}{2D}[(\bar{\lambda}_1)^4 - 1]^2 + \frac{\Pi\theta}{cD}. \tag{29}$$

Equation (29) is an evolution equation of the internal variable α depending on the elastic stretches $\bar{\lambda}_i$, which provides a supplement of the constitutive relations given by (26).

In particular, if the cubic composite sample is immersed in water and swells freely without any mechanical loading, then we have $\bar{\lambda}_1 = \bar{\lambda}_2 = \bar{\lambda}_3 = 1$ and $\sigma_{11} = \sigma_{22} = \sigma_{33} = 0$. From (26a), the osmotic pressure is derived as

$$\Pi = c\gamma GJ^{-1}. \tag{30}$$

We further substitute (30) into (29) and set $\bar{\lambda}_i = 1$, and then derive the evolution equation of α for the case of free swelling as

$$\left(\frac{\dot{\alpha}}{1-\alpha}\right)^{1/n} = \frac{\gamma\theta G}{JD}, \tag{31}$$
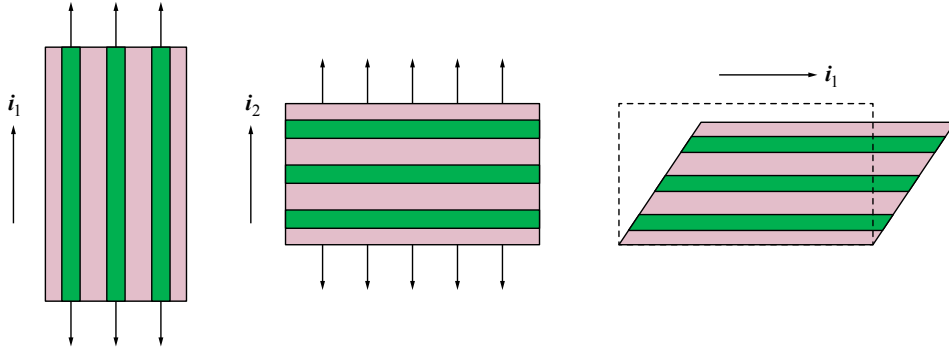
Figure 1. Three loading cases for deriving five elastic coefficients: (left) tensile along the fiber direction, (center) tensile transverse to the fiber direction, and (right) simple shear along the fiber direction.

which takes the same form as that in [Pan and Zhong 2014b] using the I_4-dependent model. But the evolution equations based on these two models are different in the case of constrained swelling.

3.2. *The evolutions of five elastic coefficients.* Based on the constitutive relation (26), the five elastic coefficients of a transversely isotropic composite material are derived for three loading cases (elastic deformation), as illustrated in Figure 1.

In the first case, a uniaxial tensile test along the reinforcing direction (X_1-axis) is studied, as shown in Figure 1(left). According to the incompressibility condition, the stretches should satisfy the relation

$$\bar{\lambda}_2 = \bar{\lambda}_3 = (\bar{\lambda}_1)^{-1/2}, \tag{32}$$

from which two Poisson's ratios are derived as

$$\upsilon_{12} = \upsilon_{13} = -\left.\frac{d\bar{\lambda}_2}{d\bar{\lambda}_1}\right|_{\bar{\lambda}_1=1} = \frac{1}{2}. \tag{33}$$

According to the boundary condition $\sigma_{22} = \sigma_{33} = 0$, the Lagrange multiplier Π is obtained as

$$\Pi = \tfrac{1}{3}Gd_1(\alpha)[(\bar{\lambda}_1)^2 - (\bar{\lambda}_1)^{-1}] + \tfrac{4}{3}c\gamma Gd_2(\alpha)[(\bar{\lambda}_1)^8 - (\bar{\lambda}_1)^4] + c\gamma GJ^{-1}. \tag{34}$$

Substituting (34) into (26a), the tensile stress σ_{11} along the fiber direction is obtained as

$$\sigma_{11} = Gd_1(\alpha)[(\bar{\lambda}_1)^2 - (\bar{\lambda}_2)^{-1}] + 4c\gamma Gd_2(\alpha)[(\bar{\lambda}_1)^8 - (\bar{\lambda}_1)^4]. \tag{35}$$

The tensile modulus E_1 along the fiber direction can be determined by the tangential modulus at $\bar{\lambda}_1 = 1$ from (35), and is calculated as

$$E_1 = \left.\frac{d\sigma_{11}}{d\bar{\lambda}_1}\right|_{\bar{\lambda}_1=1} = 3Gd_1(\alpha) + 16c\gamma Gd_2(\alpha). \tag{36}$$

The second case concerns a tensile loading transverse to the fiber direction, as illustrated in Figure 1(center), from which the Poisson's ratios υ_{21} and υ_{23} can be determined. In this case, the relation between

the three principal stretches is given as

$$\bar{\lambda}_3 = (\bar{\lambda}_1 \bar{\lambda}_2)^{-1}. \tag{37}$$

From the given boundary conditions $\sigma_{11} = \sigma_{33} = 0$, it is established that

$$G(1 - \beta_1 \alpha)[(\bar{\lambda}_1)^2 - (\bar{\lambda}_3)^2] + 4c\gamma G(1 - \beta_2 \alpha)[(\bar{\lambda}_1)^8 - (\bar{\lambda}_1)^4] = 0. \tag{38}$$

Substituting (37) into (38), we then obtain the Poisson's ratio υ_{21} as

$$\upsilon_{21} = -\frac{d\bar{\lambda}_1}{d\bar{\lambda}_2}\bigg|_{\bar{\lambda}_2 = 1} = \frac{1 - \beta_1 \alpha}{2[(1 - \beta_1 \alpha) + 4c\gamma(1 - \beta_2 \alpha)]}. \tag{39}$$

Similarly, the Poisson's ratio υ_{23} is derived as

$$\upsilon_{23} = -\frac{d\bar{\lambda}_3}{d\bar{\lambda}_2}\bigg|_{\bar{\lambda}_2 = 1} = \frac{(1 - \beta_1 \alpha) + 8c\gamma(1 - \beta_2 \alpha)}{2[(1 - \beta_1 \alpha) + 4c\gamma(1 - \beta_2 \alpha)]}. \tag{40}$$

The third loading case is a simple shear along the fiber direction, as shown in Figure 1(right), in which the deformation gradient is given as $\bar{F} = I + k e_1 \otimes e_2$. Then, from (17), the shear stress σ_{12} is given by

$$\sigma_{12} = Gd_1(\alpha)k + 2G\gamma d_2(\alpha)k^3. \tag{41}$$

Hence the shear modulus is derived as

$$G_{12} = G_{21} = \frac{\partial \sigma_{12}}{\partial k}\bigg|_{k=0} = Gd_1(\alpha). \tag{42}$$

We have now obtained all five of the independent elastic coefficients. Other elastic coefficients can be derived based on some elastic relationships of transverse isotropy. For example, the tensile modulus E_2 is calculated as $E_2 = E_1 \upsilon_{21}/\upsilon_{12}$.

4. Results and discussion

In this section, we will use the theory established above on the I_5-dependent model to predict the evolution of the moisture absorption and the mechanical degradation for a unidirectional sisal fiber reinforced benzylated wood in the cases of constrained swelling and free swelling, and compare the results to those derived based on the I_4-dependent model.

At first, some necessary material parameters are fitted based on the experimental results of Lu et al. [2003], in which three samples with different fiber contents were prepared: Sample 1 (fiber content $c_1 = 0.102$, equilibrium volume fraction of water $\theta_1 = 0.085$), Sample 2 ($c_2 = 0.196$, $\theta_2 = 0.114$) and Sample 3 ($c_3 = 0.304$, $\theta_3 = 0.148$). In their experiment, each sample was immersed in water to simulate the moisture absorption process in a humid environment. At several time intervals, they were taken out of the water to measure the loss of tensile modulus. By means of similar procedures [Pan and Zhong 2014b], the shear modulus (G), the relative stiffness (γ), and the maximum degradation parameters of the matrix and fiber ($\bar{\beta}_1$ and β_2) can be obtained by fitting the experimental data of the tensile modulus of the dry samples ($\alpha = 0$) and the fully saturated samples ($\alpha = 1$) based on (36), while the evolution
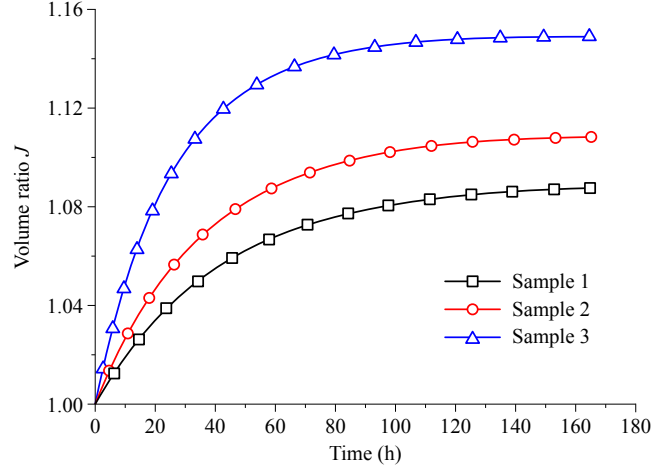
**Figure 2.** The predicted evolution of the volume ratio J for three samples under free swelling.

speed parameter (D) can be derived by fitting the evolution data of $\alpha(t)$ for Sample 1 based on (31). These parameters necessary for the I_5-dependent model are given as

$$G = 0.13\,\text{GPa}, \quad \gamma = 17.5, \quad \bar{\beta}_1 = 70.11, \quad \beta_2 = 0.56, \quad D = 3.22 \times 10^4\,\text{Nsm}^{-2}. \tag{43}$$

Employing the molecular incompressibility condition $J = 1 + \theta\alpha$, we can further obtain theoretically the evolution of the volume ratio of each sample from (26) and (31), which is illustrated in Figure 2. For these samples with three different fiber contents, the variation trends are identical, where the swelling speed is much faster at the initial stage, then tends to slow down, and finally terminates at the equilibrium state. This phenomenon is interpreted as the gradual increase of the chemical potential inside the composite. Moreover, a comparison between these samples shows that the kinetic swelling process is sensitive to the fiber content such that the swelling speed of a composite with higher fiber content is bigger than that with lower fiber content.

Next, the theoretical framework established in Sections 2 and 3 is used to predict the mechanical degradation of a sisal fiber reinforced benzylated wood (Sample 2) subject to constrained swelling. By means of those five material parameters for the I_5-dependent model, given in (43), we study the modulus loss for free swelling ($\bar{C} = I$) and constrained swelling ($\bar{C} \neq I$). Here we consider two cases of constrained swelling: (1) $\bar{\lambda}_1 = 1/(0.95)^2$, $\bar{\lambda}_2 = \bar{\lambda}_3 = 0.95$, and (2) $\bar{\lambda}_1 = 1/(1.05)^2$, $\bar{\lambda}_2 = \bar{\lambda}_3 = 1.05$, compared with the case of free swelling ($\bar{\lambda}_1 = \bar{\lambda}_2 = \bar{\lambda}_3 = 1$).

In terms of (29), (31) and (36), the evolutions of the modulus E_1 under the case of free swelling and two cases of constrained swelling are calculated based, respectively, on the I_5-dependent model and the I_4-dependent model, as shown in Figure 3. The material parameters used for the I_4-dependent model are taken directly from [Pan and Zhong 2014b]: the shear modulus $G = 0.13\,\text{GPa}$, the relative stiffness $\gamma = 70.13$, the maximum degradation parameters of matrix $\bar{\beta}_1 = 70.11$ and fiber $\beta_2 = 0.56$, and the evolution speed parameter $D = 1.28 \times 10^5\,\text{Nsm}^{-2}$. It can be seen from Figure 3 that the modulus E_1 degrades with time due to the moisture absorption, for both free and constrained swelling. At the beginning the modulus degrades rapidly and gradually slows down. For free swelling, the predictions from the I_5-dependent
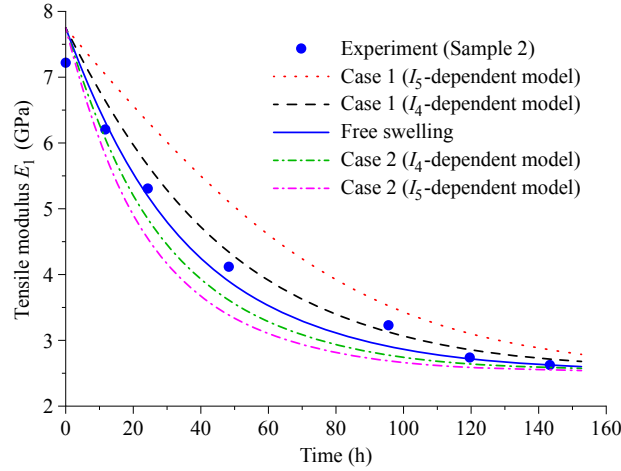
Figure 3. The evolution of the tensile modulus E_1 predicted from the I_5-dependent model and the I_4-dependent model in the cases of free swelling and constrained swelling.

model and the I_4-dependent model give identical results and match well with experimental data obtained by Lu et al. [2003]. However, in the case of constrained swelling, a remarkable difference can be found between the curves obtained from these two models. Compared to free swelling ($\bar{\lambda}_1 = \bar{\lambda}_2 = \bar{\lambda}_3 = 1$), the modulus E_1 degrades more slowly for a tensile compressive elastic deformation along the fiber direction (Case 1 with $\bar{\lambda}_1 = \bar{\lambda}_2^{-2} = \bar{\lambda}_3^{-2} > 1$) and more quickly for a compressive elastic deformation along the fiber direction (Case 2 with $\bar{\lambda}_1 = \bar{\lambda}_2^{-2} = \bar{\lambda}_3^{-2} < 1$). This prediction reveals that the mechanical degradation of NFRCMs can be largely influenced by different constraints during swelling. It is interesting to see that the I_5-dependent model predicts a smaller modulus loss for Case 1 and a bigger modulus loss for Case 2, compared to the I_4-dependent model.

5. Conclusions

This paper establishes a constitutive model of unidirectional natural fiber reinforced composites subjected to mechanical loading and moisture absorption. An internal variable is introduced to consider irreversible energy dissipation by moisture absorption, and is incorporated in the Helmholtz free energy, which can be decomposed into the isotropic matrix part, the reinforcing part and the volume expansion part. With specialized free energies, the degradations of elastic modulus are predicted for unidirectional natural fiber reinforced composites in the cases of free swelling and constrained swelling based on the I_4-dependent model and the I_5-dependent model for reinforcing energy. It is found that these two models give results that are identical in the case of free swelling and different in the case of constrained swelling. However, the predictions from these two models reveal a consistent conclusion that the mechanical degradation of NFRCMs largely depends on the external constraints during the swelling process. This may provide an effective approach to reduce the mechanical degradation induced by moisture absorption.

Acknowledgments

References

[Athijayamani et al. 2009] A. Athijayamani, M. Thiruchitrambalam, U. Natarajan, and B. Pazhanivel, "Effect of moisture absorption on the mechanical properties of randomly oriented natural fibers/polyester hybrid composite", *Materials Science and Engineering: A* **517**:1–2 (2009), 344–353.

[Baek and Pence 2009] S. Baek and T. J. Pence, "On swelling induced degradation of fiber reinforced polymers", *Internat. J. Engrg. Sci.* **47**:11-12 (2009), 1100–1109.

[Baek and Pence 2011] S. Baek and T. J. Pence, "On mechanically induced degradation of fiber-reinforced hyperelastic materials", *Math. Mech. Solids* **16**:4 (2011), 406–434.

[Demirkoparan and Pence 2007a] H. Demirkoparan and T. J. Pence, "The effect of fiber recruitment on the swelling of a pressurized anisotropic non-linearly elastic tube", *International Journal of Non-Linear Mechanics* **42**:2 (2007), 258–270. Special Issue in Honour of Dr Ronald S. Rivlin.

[Demirkoparan and Pence 2007b] H. Demirkoparan and T. J. Pence, "Swelling of an internally pressurized nonlinearly elastic tube with fiber reinforcing", *International Journal of Solids and Structures* **44**:11–12 (2007), 4009–4029.

[Demirkoparan and Pence 2008] H. Demirkoparan and T. J. Pence, "Torsional swelling of a hyperelastic tube with helically wound reinforcement", *J. Elasticity* **92**:1 (2008), 61–90.

[Dhakal et al. 2007] H. N. Dhakal, Z. Y. Zhang, and M. O. W. Richardson, "Effect of water absorption on the mechanical properties of hemp fibre reinforced unsaturated polyester composites", *Composites Science and Technology* **67**:7–8 (2007), 1674–1683.

[Espert et al. 2004] A. Espert, F. Vilaplana, and S. Karlsson, "Comparison of water absorption in natural cellulosic fibres from wood and one-year crops in polypropylene composites and its influence on their mechanical properties", *Composites Part A: Applied Science and Manufacturing* **35**:11 (2004), 1267–1276.

[Fang et al. 2011] Y. Fang, T. J. Pence, and X. Tan, "Fiber-directed conjugated-polymer torsional actuator: nonlinear elasticity modeling and experimental validation", *Mechatronics, IEEE/ASME Transactions on* **16**:4 (Aug 2011), 656–664.

[Gao et al. 2011] C. Gao, Y. Wan, F. He, H. Liang, H. Luo, and J. Han, "Mechanical, moisture absorption, and photodegradation behaviors of bacterial cellulose nanofiber-reinforced unsaturated polyester composites", *Advances in Polymer Technology* **30**:4 (2011), 249–256.

[Holzapfel 2000] G. A. Holzapfel, *Nonlinear solid mechanics*, John Wiley & Sons, Ltd., Chichester, 2000. A continuum approach for engineering.

[Hong et al. 2008] W. Hong, X. Zhao, J. Zhou, and Z. Suo, "A theory of coupled diffusion and large deformation in polymeric gels", *Journal of the Mechanics and Physics of Solids* **56**:5 (2008), 1779–1793.

[Hu et al. 2010] R.-H. Hu, M. young Sun, and J.-K. Lim, "Moisture absorption, tensile strength and microstructure evolution of short jute fiber/polylactide composite in hygrothermal environment", *Materials & Design* **31**:7 (2010), 3167–3173.

[Karra and Rajagopal 2012] S. Karra and K. R. Rajagopal, "A model for the thermo-oxidative degradation of polyimides", *Mechanics of Time-Dependent Materials* **16**:3 (2012), 329–342.

[Lu et al. 2003] X. Lu, M. Q. Zhang, M. Z. Rong, G. Shi, and G. C. Yang, "All-plant fiber composites II: water absorption behavior and biodegradability of unidirectional sisal fiber reinforced benzylated wood", *Polymer Composites* **24**:3 (2003), 367–379.

[Medina et al. 2009] L. Medina, R. Schledjewski, and A. K. Schlarb, "Process related mechanical properties of press molded natural fiber reinforced polymers", *Composites Science and Technology* **69**:9 (2009), 1404–1411. Special Issue on the 12th European Conference on Composite Materials (ECCM12), organized by the European Society for Composite Materials (ESCM).

[Merodio and Ogden 2005] J. Merodio and R. W. Ogden, "Mechanical response of fiber-reinforced incompressible non-linearly elastic solids", *International Journal of Non-Linear Mechanics* **40**:2–3 (2005), 213–227. Special Issue in Honour of C. O. Horgan.

[Moon and Spencer 1988] P. Moon and D. E. Spencer, *Field theory handbook*, 2nd ed., Springer, Berlin, 1988. Including coordinate systems, differential equations and their solutions.

[Pan and Zhong 2014a] Y. Pan and Z. Zhong, "Modeling of the mechanical degradation induced by moisture absorption in short natural fiber reinforced composites", *Composites Science and Technology* **103**:0 (2014), 22–27.

[Pan and Zhong 2014b] Y. Pan and Z. Zhong, "A nonlinear constitutive model of unidirectional natural fiber reinforced composites considering moisture absorption", *J. Mech. Phys. Solids* **69** (2014), 132–142.

[Qiu and Pence 1997] G. Y. Qiu and T. J. Pence, "Remarks on the behavior of simple directionally reinforced incompressible nonlinearly elastic solids", *J. Elasticity* **49**:1 (1997), 1–30.

[Rajagopal and Srinivasa 2004] K. R. Rajagopal and A. R. Srinivasa, "On the thermomechanics of materials that have multiple natural configurations. I. Viscoelasticity and classical plasticity", *Z. Angew. Math. Phys.* **55**:5 (2004), 861–893.

[Rajagopal et al. 2007] K. R. Rajagopal, A. R. Srinivasa, and A. S. Wineman, "On the shear and bending of a degrading polymer beam", *International Journal of Plasticity* **23**:9 (2007), 1618–1636.

[Sgriccia et al. 2008] N. Sgriccia, M. C. Hawley, and M. Misra, "Characterization of natural fiber surfaces and natural fiber composites", *Composites Part A: Applied Science and Manufacturing* **39**:10 (2008), 1632–1637.

[Soares et al. 2009] J. S. Soares, K. R. Rajagopal, and J. E. Moore, "Deformation-induced hydrolysis of a degradable polymeric cylindrical annulus", *Biomech. Model Mechanobiol.* **9**:2 (2009), 177–186.

[Song et al. 2011] J.-H. Song, S.-D. Mun, and C.-S. Kim, "Mechanical properties of sisal natural fiber composites according to strain rate and absorption ratio", *Polymer Composites* **32**:8 (2011), 1174–1180.

[Spencer 1984] A. J. M. Spencer, "Constitutive theory for strongly anisotropic solids", pp. 1–32 in *Continuum theory of the mechanics of fibre-reinforced composites*, edited by A. J. M. Spencer, International Centre for Mechanical Sciences **282**, Springer Vienna, 1984.

[Sydenstricker et al. 2003] T. H. D. Sydenstricker, S. Mochnaz, and S. C. Amico, "Pull-out and other evaluations in sisal-reinforced polyester biocomposites", *Polymer Testing* **22**:4 (2003), 375–380.

[Tsai et al. 2004] H. Tsai, T. J. Pence, and E. Kirkinis, "Swelling induced finite strain flexure in a rectangular block of an isotropic elastic material", *J. Elasticity* **75**:1 (2004), 69–89.

YIHUI PAN: 083633@tongji.edu.cn
School of Aerospace Engineering and Applied Mechanics, Tongji University, Shanghai, 200092, China

ZHENG ZHONG: zhongk@tongji.edu.cn
School of Aerospace Engineering and Applied Mechanics, Tongji University, Shanghai, 200092, China

msp

ON THE OCCURRENCE OF LUMPED FORCES AT CORNERS IN CLASSICAL PLATE THEORIES: A PHYSICALLY BASED INTERPRETATION

LAURA GALUPPI AND GIANNI ROYER-CARFAGNI

The paradigmatic example of a twisted square plate is here considered. An *equivalent* partition of the plate in a grid of beams *à la* Grashof is found such that, as the number of beams tends to infinity, the grid exhibits the same deflection of the plate. This scheme is used to interpret, through the distinction between Euler–Bernoulli and Timoshenko beam theories, the different types of natural boundary conditions that can arise in the Kirchhoff–Love and Mindlin–Reissner theories of plates. A physically based interpretation for the occurrence of lumped forces at the plate corners through the formation of a boundary layer is provided.

1. Introduction

It is well known that the solution of the biharmonic equation governing the bending of plates in Kirchhoff–Love theory is compatible with only two distinct conditions at each boundary point, whereas in general three boundary data can be independently assigned on an unconstrained border. This contradiction for the order of the equation is a two-hundred-year-old problem. The paradox arose when the three-boundary-data statement by Poisson [1829] was criticized by Kirchhoff [1850], who obtained only two natural conditions at the border within a variational framework, using a static equivalence sometimes referred to as the "Kirchhoff transformation" [Vasil'ev 2012]. This result arose from the first variation of the energy functional, but it was not corroborated by any physically based interpretation. A long discussion ensued among the most eminent scientists of the period with the purpose of reconciling the Poisson and Kirchhoff theories. The dispute culminated with the elementary interpretation by Thomson and Tait [1883], who showed how to reduce the torque per unit length on the contour to a shear transverse force. Friedrichs and Dressler [1961] and Gol'Denveiser and Kolos [1965] have independently shown that the plate theory is the leading term of the expansion solution (in a small thickness parameter) for the linear elastostatics of thin, flat, isotropic bodies. As expected, this leading term alone is unable to satisfy arbitrarily prescribed edge conditions.

There has been a renewed interest during the last years in the fundamental problem of understanding the relationship between the three-dimensional elasticity theory and theories for lower-dimensional objects (plates, shells, rods). Due to the availability of sophisticated methods of variational convergence [Ciarlet 1997], important achievements have been obtained by showing that various theories of plates arise as a rigorous variational limit (or Γ-limit) of the equations of three-dimensional elasticity as the

thickness tends to zero, both in the linear and in the nonlinear case [Friesecke et al. 2006]. An approach of this kind allows one to rigorously recover the Kirchhoff–Thomson–Tait boundary conditions.

In particular, the Kirchhoff transformation results in the appearance of lumped forces at corners of rectangular plates, which are sometimes suspiciously treated as a drawback of the theory [Alfutov 1992]. Mutually exclusive interpretations either admit the existence of actual supporting reactions associated with the Kirchhoff transformation, possibly due to internal constraints [Podio-Guidugli 1989], or completely deny the physical meaning of this approach [Zhilin 1995]. Vasil'ev [2012] has discussed the applicability of the Kirchhoff transformation, concluding that, for plates with fixed contour, the reduction of twisting moments to shear forces can be performed only approximately: in general, it is not applicable for static boundary conditions where the torque is prescribed on the plate contour. In such cases, one has to consider higher-order theories like Mindlin–Reissner theory [Mindlin 1951; Reissner 1945], accounting for the boundary effect due to shear strains.

The aim of this note is to give an elementary, physically based, interpretation for the occurrence of lumped forces at plate corners, predicted by the Kirchhoff transformation, through the paradigmatic example of a twisted square plate. The approach is somehow dual to the customary derivation of plate theory as a downgrade limit of the equations of three-dimensional elasticity: here, plate theory is considered as a proper *upgrade* of lower-order beam theory. A partition *à la* Grashof [1878] of the plate as a grid of beams will provide an immediate interpretation of the diffusion of stress from the corners, where the forces are applied, to the interior of the body. Such diffusion strongly depends upon the shear stiffness of the constituting beams. Different types of responses can be obtained if one assumes for the beams either the Euler–Bernoulli or the Timoshenko [1940] models. This distinction is at the base of the different types of boundary conditions arising in the Kirchhoff–Love or Mindlin–Reissner theories, which somehow represent the counterparts, for plates, of the Euler–Bernoulli and the Timoshenko one-dimensional approaches, respectively.

2. Practice

Let $\mathscr{B} \equiv \Omega \times [-h, h] \subset \mathbb{R}^3$, $\Omega \subset \mathbb{R}^2$, denote the undistorted reference configuration of a flat plate, with boundary $\partial\Omega \times [-h, h]$ supposed piecewise regular. Introduce a right-handed orthogonal reference system $\boldsymbol{x} = (x_1, x_2, x_3)$, with $x_1, x_2 \in \Omega$ and x_3 at a right angle to them, and let $(\boldsymbol{e}_1, \boldsymbol{e}_2, \boldsymbol{e}_3)$ denote the associated unit vectors. It is customary [Timoshenko and Woinowsky-Krieger 1959] to define the stress state inside the plate through thickness-averaged descriptors of the Cauchy stress field $\tau_{ij}\boldsymbol{e}_i \otimes \boldsymbol{e}_j$, $i, j = 1, 2, 3$. In particular, the shear forces per unit length Q_α and the moments per unit length $M_{\alpha\beta}$, $\alpha, \beta = 1, 2$, are defined as

$$Q_\alpha = \int_{-h}^{h} \tau_{\alpha 3} \, dx_3, \quad M_{\alpha\beta} = \int_{-h}^{h} x_3 \tau_{\alpha\beta} \, dx_3, \quad \alpha, \beta = 1, 2. \tag{2-1}$$

In this way the problem becomes two-dimensional, and definable in the domain Ω and its boundary $\partial\Omega$.

Let $p\boldsymbol{e}_3$, with $p = \hat{p}(x_1, x_2)$, represent the force per unit area acting orthogonally to Ω. With a little abuse of notation, define

$$\boldsymbol{Q} = \sum_{\alpha=1}^{2} Q_\alpha \boldsymbol{e}_\alpha, \quad \boldsymbol{M} = \sum_{\alpha,\beta=1}^{2} M_{\alpha\beta} \boldsymbol{e}_\alpha \otimes \boldsymbol{e}_\beta, \quad \alpha, \beta = 1, 2, \tag{2-2}$$

where clearly $M = M^T$. The equilibrium in the x_3 direction and the equilibrium of moments around any axis parallel to Ω read, respectively,

$$\operatorname{div} Q = -p, \quad \operatorname{div} M = Q, \tag{2-3}$$

where "div" denotes the divergence operator in $\mathbb{R}^2$. By combining the aforementioned relationships one readily obtains the equilibrium equation $\operatorname{div}(\operatorname{div} M) = -p$.

Denoting with a comma partial differentiation with respect to the indicated variable, the Kirchhoff–Love kinematical hypothesis [Timoshenko and Woinowsky-Krieger 1959] consists in assuming that the displacement field $u = u_1 e_1 + u_2 e_2 + u_3 e_3$ has the form

$$u_3(x) = w(x_1, x_2), \quad u_\alpha(x) = -x_3 w_{,\alpha}(x_1, x_2), \quad \alpha = 1, 2, \tag{2-4}$$

where we have not considered (for simplicity, and because it is here irrelevant) the membrane strain due to forces in the plate middle-plane. Consequently, the strain components ε_{ij}, $i, j = 1, 2, 3$, read

$$\varepsilon_{\alpha\beta} = -x_3 \, w_{,\alpha\beta}(x_1, x_2), \quad \varepsilon_{\alpha 3} = 0, \quad \varepsilon_{33} = 0, \quad \alpha, \beta = 1, 2. \tag{2-5}$$

If the material is homogeneous and isotropic, denoting by E the Young's modulus and by ν the Poisson's ratio, one finds

$$\begin{cases} M_{11} = -\dfrac{2h^3 E}{3(1 - \nu^2)}[w_{,11} + \nu\, w_{,22}], \\[2mm] M_{22} = -\dfrac{2h^3 E}{3(1 - \nu^2)}[w_{,22} + \nu\, w_{,11}], \\[2mm] M_{12} = -\dfrac{2h^3 E}{3(1 + \nu)}\, w_{,12}. \end{cases} \tag{2-6}$$

This theory, as is clear from (2-5), neglects shear deformations, but the shear strains Q_α of (2-2) can be recovered from just the equilibrium considerations from (2-3).

The strains due to shear are accounted for in the Mindlin–Reissner theory of moderately thick plates [Reissner 1945; Mindlin 1951], where the displacement field is assumed of the form

$$u_3(x) = w(x_1, x_2), \quad u_\alpha(x) = -x_3 \varphi_\alpha(x_1, x_2), \quad \alpha = 1, 2, \tag{2-7}$$

where φ_α is the rotation of fibers parallel to e_α with, in general, $\varphi_\alpha \neq w_{,\alpha}$. The strain components thus become

$$\varepsilon_{\alpha\beta} = -\tfrac{1}{2}x_3(\varphi_{\alpha,\beta} + \varphi_{\beta,\alpha}), \quad \varepsilon_{\alpha 3} = \tfrac{1}{2}(w_{,\alpha} - \varphi_\alpha), \quad \varepsilon_{33} = 0; \quad \alpha, \beta = 1, 2. \tag{2-8}$$

From these, the constitutive equations read

$$\begin{cases} M_{11} = -\dfrac{2h^3 E}{3(1 - \nu^2)}\, [\varphi_{1,1} + \nu\varphi_{2,2}], \\[2mm] M_{22} = -\dfrac{2h^3 E}{3(1 - \nu^2)}\, [\varphi_{2,2} + \nu\varphi_{1,1}], \\[2mm] M_{12} = -\dfrac{h^3 E}{3(1 + \nu)}\, [\varphi_{1,2} + \varphi_{2,1}], \end{cases} \tag{2-9}$$

$$\begin{cases} Q_1 = -\kappa\, Gh\, [w_{,1} - \varphi_1], \\ Q_2 = -\kappa\, Gh\, [w_{,2} - \varphi_2], \end{cases} \qquad (2\text{-}10)$$

where κ is the shear correction factor, usually assumed equal to $\frac{5}{6}$.

Both in the Kirchhoff–Love and the Mindlin–Reissner theories, the governing field equations in terms of displacements are obtained by inserting the constitutive equations (2-6), or (2-9)–(2-10), into the equilibrium equations (2-3). The first theory gives rise to the well-known biharmonic equation in w, whereas the second theory produces two differential equations in w and φ_α.

At the boundary $\partial\Omega$ define the orthogonal right-handed triad of unit vectors $(\boldsymbol{m}, \boldsymbol{t}, \boldsymbol{n})$, with $\boldsymbol{n}$ parallel and in the same direction as $\boldsymbol{e}_3$, while $\boldsymbol{m} = m_1\boldsymbol{e}_1 + m_2\boldsymbol{e}_2$ is the outward unit normal to $\partial\Omega$ and, consequently, $\boldsymbol{t} = t_1\boldsymbol{e}_1 + t_2\boldsymbol{e}_2 = -m_2\boldsymbol{e}_1 + m_1\boldsymbol{e}_2$ is tangent to $\partial\Omega$. Introduce then a curvilinear abscissa s, parametrized by arc length and oriented as $\boldsymbol{t}$. The static state at $\partial\Omega$ is defined by the bending moment $M_m\boldsymbol{t}$, by the torque $-M_{mt}\boldsymbol{m}$ and by the shear force $Q_m\boldsymbol{n} = Q_m\boldsymbol{e}_3$, all of them per unit length of the border. One has

$$M_m = \boldsymbol{M}\boldsymbol{m} \cdot \boldsymbol{m}, \quad M_{mt} = \boldsymbol{M}\boldsymbol{m} \cdot \boldsymbol{t}, \quad Q_m = \boldsymbol{Q} \cdot \boldsymbol{m}. \qquad (2\text{-}11)$$

The boundary conditions are substantially different in the two aforementioned theories of plates, in agreement with the order of the governing differential equations.

In Mindlin–Reissner theory, the geometric boundary conditions may involve three quantities: the displacement u_3 and the two rotation components in both the normal direction $\boldsymbol{m}$ (i.e., $\varphi_m = \varphi_1 m_1 + \varphi_2 m_2$) and in the tangential direction $\boldsymbol{t}$ (i.e., $\varphi_t = \varphi_1 t_1 + \varphi_2 t_2$). The corresponding natural boundary conditions involve, respectively, Q_m, M_m and M_{mt}, that is, the shear force, the bending moment and the torque (per unit length), defined in (2-11).

On the other hand, it is well-known that in Kirchhoff–Love theory the three quantities Q_m, M_m and M_{mt} cannot be prescribed independently. In fact, the Kirchhoff transformation defines the *effective* shear force per unit length

$$V_m\boldsymbol{n} = V_m\boldsymbol{e}_3 = [Q_m + (M_{mt})_{,s}]\boldsymbol{n}, \qquad (2\text{-}12)$$

which is dual in energy with the vertical displacement at the boundary. Therefore, on $\partial\Omega$ the geometric boundary conditions prescribe either the displacement w in the direction $\boldsymbol{e}_3$ or its derivative $w_{,m}$ with respect to the outward unit normal $\boldsymbol{m}$, to which correspond the natural boundary conditions on the effective shear force V_m, defined as per (2-12), and on the bending moment M_m, given by $(2\text{-}11)_1$.

If the boundary presents a corner at $s = s_0$, denote by $\boldsymbol{m}(s_0^+)$, $\boldsymbol{t}(s_0^+)$ and $\boldsymbol{m}(s_0^-)$, $\boldsymbol{t}(s_0^-)$ the normal and tangential unit vectors at $s = s_0^+$ and $s = s_0^-$, respectively. Then, the Kirchhoff transformation implies the occurrence of lumped forces $F(s_0)\boldsymbol{e}_3$ at the corner given by

$$F(s_0) = \boldsymbol{M}(s_0)\boldsymbol{m}(s_0^+) \cdot \boldsymbol{t}(s_0^+) - \boldsymbol{M}(s_0)\boldsymbol{m}(s_0^-) \cdot \boldsymbol{t}(s_0^-) = M_{mt}(s_0^+) - M_{mt}(s_0^-), \qquad (2\text{-}13)$$

which are usually considered to be physically justified by the presence of unbalanced torques.

3. A paradigmatic example

The following example can be found in most textbooks (see, e.g., [Timoshenko and Woinowsky-Krieger 1959, Section 11] or [Belluzzi 1986, exercise 1187]). With reference to Figure 1, let Ω be the square
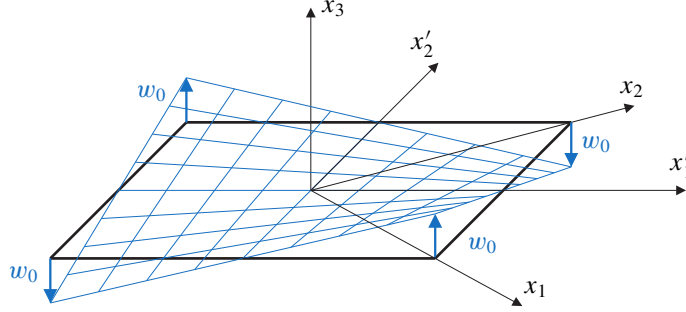
Figure 1. Reference and deformed configurations of the square plate.

defined by the vertices $(x_1, x_2) = (d/2, 0)$, $(0, d/2)$, $(-d/2, 0)$, $(0, -d/2)$, where d is the length of the diagonal. Our aim here is to determine states of stress that are compatible with a vertical displacement of the type

$$w(x_1, x_2) = 4w_0 \frac{x_1^2 - x_2^2}{d^2}, \tag{3-1}$$

which represents a hyperbolic paraboloid.

3.1. *State of stress and boundary conditions.* It is easy to verify that in a Kirhhoff–Love plate one has from (2-6), (2-3)$_2$ and (2-11)$_2$ that

$$M_{11} = -M_{22} = -\frac{16h^3 E}{3(1+v)d^2} w_0, \quad M_{12} = 0, \quad Q_1 = Q_2 = 0. \tag{3-2}$$

Then, clearly, from (2-12), $V_m = 0$. But, from (2-13), four concentrated forces are acting at the four corners of the plate and, more precisely,

$$F_0 e_3 \quad \text{at } (d/2, 0), \ (-d/2, 0); \quad -F_0 e_3 \quad \text{at } (0, d/2), \ (0, -d/2); \quad F_0 = \frac{32h^3 E}{3(1+v)d^2} w_0. \tag{3-3}$$

Denoting by (x_1', x_2') an auxiliary reference system rotated by $\pi/4$ with respect to (x_1, x_2), as represented in Figure 1, it is possible to verify that

$$M_{1'1'} = M_{2'2'} = 0, \quad M_{1'2'} = \frac{\boldsymbol{M}}{2}(\boldsymbol{e}_1 + \boldsymbol{e}_2) \cdot (-\boldsymbol{e}_1 + \boldsymbol{e}_2) = -\frac{16h^3 E}{3(1+v)d^2} w_0. \tag{3-4}$$

Therefore, whereas the four borders of the plate are stress free, in the immediate neighborhood, on lines parallel to each border, the torque per unit length is not zero. This turns out to be an apparent contradiction of the theory [Alfutov 1992].

Consider, on the other hand, a Mindlin–Reissner plate. We look for a solution which is associated with a null shear deformation: the purpose of this choice is to find, within the framework of this higher-order theory, the same state of stress predicted by Kirchhoff–Love theory. In fact, if in (2-8) $\varepsilon_{\alpha 3} = 0$, $\alpha = 1, 2$, then $\varphi_\alpha = w_{,\alpha}$ and, consequently, one finds from (2-9) the field (3-2). At the boundary the only nonzero component of stress is the torque per unit length, which is equal to $M_{1'2'}$ of (3-4).

In conclusion, in a twisted plate deformed according to (3-1) with no shear, both Kirchhoff–Love and Mindlin–Reissner theories prescribe the same state of stress *inside* the plate, but the associated boundary
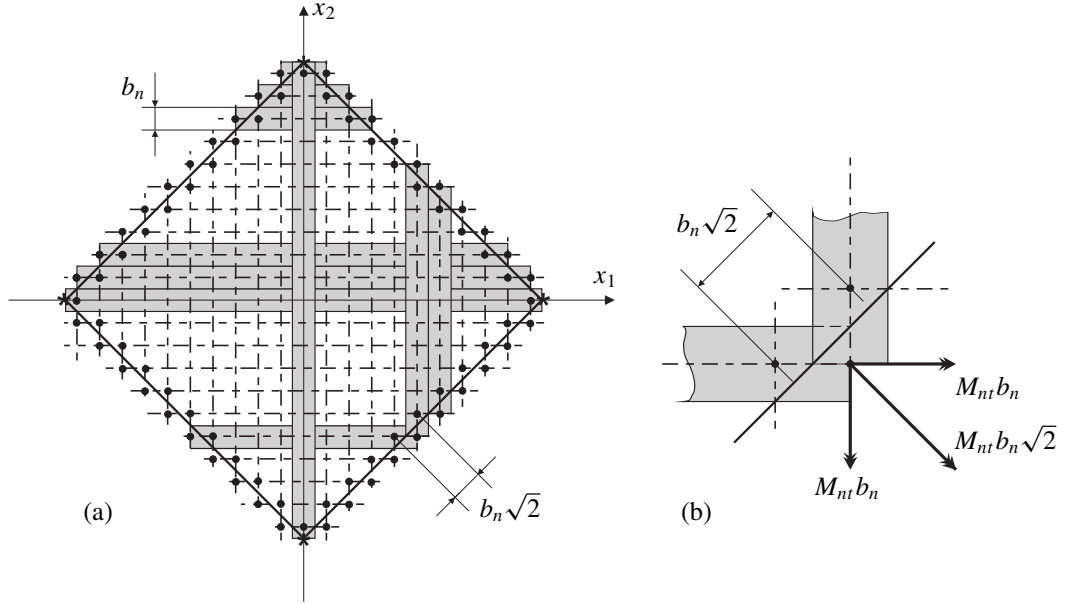
Figure 2. Partition *à la* Grashof of the square plate. (a) Ideal division into beams;
(b) decomposition of the torque at the border into two bending moments for the beams.

conditions are completely different since they predict lumped forces at the corners in the first case and uniformly distributed torque per unit length in the second case. The aim of the next section is to give an elementary physically based explanation of this finding.

3.2. *Partition* à la *Grashof*. The Grashof approximation [1878], according to which plates are considered as grids of beams, is commonly used in practical applications. Here, we will discuss a partition which is *exact*, in the sense that, when the number of beams tends to infinity, one recovers the same deflection of the plate. To do so, the body of Figure 1 is ideally divided by imaginary cuts into $(2n + 1)$ beams of the same width in the x_1 direction, and by an equal partition in the x_2 direction. Consequently, as represented in Figure 2(a), the width b_n of each beam and the corresponding cross-sectional moment of inertia I_n read, respectively,

$$b_n = \frac{d}{2n+1}, \quad I_n = \frac{2b_n h^3}{3} = \frac{2d h^3}{3(2n+1)}. \tag{3-5}$$

Consider first the Mindlin–Reissner solution described in the previous section. The border of the plate is loaded by a uniformly distributed torque per unit length, which can be distributed to each beam according to the corresponding partition of influence, of length $b_n\sqrt{2}$ as represented in Figure 2(b). Clearly, x_1 and x_2 are axes of geometric and loading symmetry for the structure. The moment resultant can then be decomposed in the two components in the e_1 and e_2 directions, which represent two bending moments for the beams.

Observe that the partition of the twisting moment into two bending moments only, with no torsion moments for the beams, is not arbitrary. In fact, each beam should carry torsion moments of opposite signs at the ends in order to satisfy equilibrium, but such a distribution violates the symmetry of the problem.[1]

In conclusion, each beam in the x_1 (resp. x_2) direction is uniformly bent by the moment $M_1^{(n)}$ (resp. $M_2^{(n)}$) given by

$$M_1^{(n)} = -M_2^{(n)} = -\frac{d}{2n+1} \frac{16h^3 E}{3(1+\nu)d^2} w_0. \tag{3-6}$$

The corresponding curvatures χ_1 and χ_2, taking into account that the transversal strain of each composing beam is restrained by the flexure of the orthogonal sets of beams, read

$$\chi_1 \simeq w_{,11} = -\frac{M_1^{(n)}}{E I_n/(1+\nu)} = 8\frac{w_0}{d^2}, \quad \chi_2 = -\frac{M_2^{(n)}}{E I_n/(1+\nu)} = -\chi_1 \simeq w_{,22}, \tag{3-7}$$

which clearly coincides with the expectation from the assumed deformation (3-1).

It should be noticed that in this case each beam is subject to pure bending. Therefore, the flexure of (3-7) remains the same whether one assumes the Euler–Bernoulli model or the Timoshenko model for the beam, i.e., whether one does or does not neglect shear deformations.

Consider now the case in which the boundary is stress-free apart from the four lumped forces F_0 of (3-3), acting at the points marked with stars in Figure 2(a). Let us suppose that the beams are connected by spherical hinges only at those points marked with dots in Figure 2(a), i.e., at those points which are closer to the border of the reference domain Ω. It will be verified, *a posteriori*, that in the limit $n \to \infty$ the deformation of the beam lattice associated with the aforementioned static state is compatible, in the sense that the deflection of each nodal point is the same if it belongs to either one of the two orthogonal beams passing through it.

Then, with symmetry considerations, the grid is statically determined and the forces acting in each beam can be directly calculated. Three possible conditions, as represented in Figure 3, need to be distinguished:

- Each one of the two longest beams of length $(2n + 1)b_n = d$ in Figure 3, whose axes coincide with one of the diagonals, is bent by the applied loads F_0 (at the plate corners), and by the reaction forces of the two orthogonal short beams hinged to them, which by statics are also equal to F_0. Such forces form pairs with lever arm $b_n/2$.

- Consequently, each one of the four shortest beams in proximity to the corners, denoted by $i = 1$ in Figure 3, of length $2b_n$, is loaded by a concentrated force F_0 in the middle and transfers two concentrated forces $F_0/2$ to the orthogonal beams of length $2nb_n$.

- One can repeat the same construction and derive that the other beams, of length $4b_n \le l \le 2nb_n$, are bent by pairs of forces at the extremities, each one formed by two forces $F_0/2$ with arm b_n.

The maximal bending moment acting in each beam is, in absolute value, equal to

$$M_F = \tfrac{1}{2}b_n F_0 = \frac{16h^3 E}{3(2n+1)(1+\nu)d} w_0, \tag{3-8}$$

---

[1]If the plate deformation was represented by a beam lattice with the beams parallel to the edges, the only distribution of loads that could respect the symmetry of this new partition would be a state of zero bending (all beams remain straight) and pure torsion.
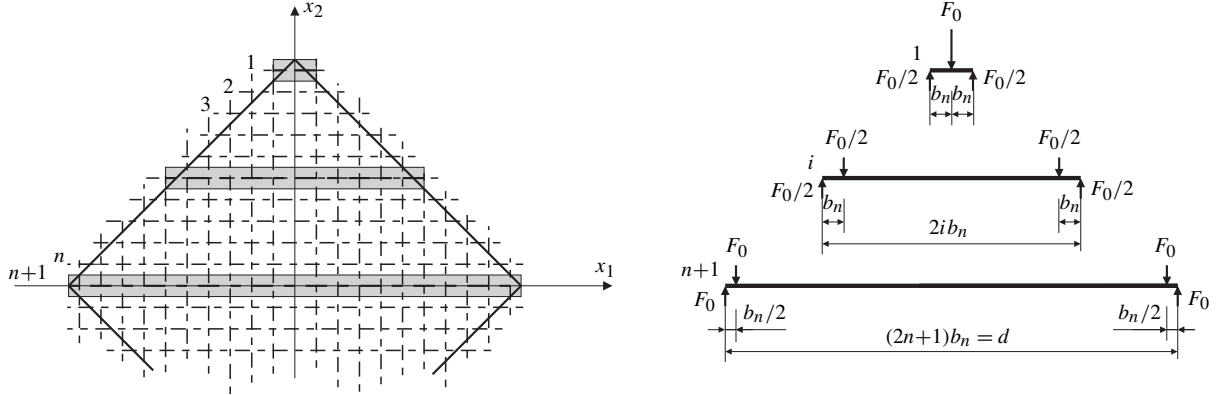
Figure 3. Bending of beams in the Grashof partition: shortest beams of length $2b_n$, intermediate beams, beams along the diagonals.

which coincides with the value prescribed by (3-6). It is then clear that in the limit of an infinite partition ($n \to \infty$), one recovers the same curvature as in (3-7). In fact, since $b_n \to 0$, the arm of the pair of forces tends to zero, but the reduction of the corresponding bending moment is exactly compensated by the reduction of the cross-sectional inertia, according to $(3\text{-}5)_2$.

It is then a simple exercise to show that if the curvature of each beam is of the form (3-7) then the deflections of the nodal points of the beam lattice accommodate one another and the resulting deformed shape is given by (3-1). Therefore, the static state that has been derived from the assumed distribution of internal constraints for the constituting elementary beams of Figure 2 is balanced and compatible.

However, one should notice that the two longest diagonal beams present a shear equal to F_0 in portions in proximity to each end of length $b_n/2$, whereas all the other beams undergo a shear equal to $F_0/2$ at the extremal portions of length b_n. As $b_n \to 0$, the corresponding shear stress tends to infinity because the width of each beam tends to zero. Denoting by γ_F and $\gamma_{F/2}$ the shear strain in the diagonal beams and in the other beams, respectively, one finds that there are relative displacements δ_F and $\delta_{F/2}$ associated with such a shear strain. These read

$$\delta_F = \gamma_F \cdot \frac{1}{2}b_n = \kappa \frac{F_0}{G\,2hb_n} \cdot \frac{1}{2}b_n = \kappa \frac{F_0}{G\,4h}, \quad \delta_{F/2} = \gamma_{F/2}b_n = \kappa \frac{F_0/2}{G\,2hb_n}b_n = \kappa \frac{F_0}{G\,4h}, \tag{3-9}$$

and are independent of n. Thus, as $n \to \infty$, a shear dislocation remains at the beam extremities.

Consequently, if the constituting elements are beams *à la* Timoshenko, one can no longer recover, with the aforementioned partition *à la* Grashof, the deformation of the plate prescribed by (3-1). The counterpart of Timoshenko beam theory for plates is Mindlin–Reissner theory. The proposed elementary example thus illustrates why Mindlin–Reissner theory cannot account for the possibility of concentrated forces at the plate corners compatibly with the assumed displacement (3-1).

On the other hand, Euler–Bernoulli beam theory cannot account for shear strain. Consequently, if one assumes this model for the Grashof partition, the concentrated displacement due to slip is null and one recovers the same curvature prescribed by (3-7). The resulting deformation is again compatible with an expression of the form (3-1). Remarkably, there is a "transformation" of the *bending with shear* produced by the lumped forces into *pure bending*. Such a transformation, made possible by the shear-insensitivity

of the constituting beams, occurs in a boundary layer whose thickness is of the order of b_n, which tends to zero as $n \to \infty$.

From this example it is clear what role is played by the Kirchhoff transformation, which regulates the substitution of the torque per unit length with lumped forces at the corners due to the assumed shear-stiffness of the constitutive model. Such a substitution takes place in a boundary layer of evanescent thickness. On the other hand, in Mindlin–Reissner theory this transformation is not allowed because of the different types of deformation that are associated with the two systems of forces due to the shear deformability of the plate.

It should also be remarked that the Kirchhoff transformation is not required, but it simply states the static and kinematic equivalence of diverse equipollent system of actions as boundary conditions. In fact, the deformation indicated by (3-1) is perfectly compatible with a Kirchhoff–Love plate twisted by lumped forces, but it is also compatible with other boundary data, e.g., uniformly distributed torque per unit length applied at the border. This model cannot distinguish between the two static distributions because their difference produces shear stress only, which are associated with a null deformation. Indeed, infinite boundary data that are statically and kinematically equivalent can be found. For example, as shown in [Fosdick and Royer-Carfagni 2015], it is sufficient to take just a part of the applied forces and, for that, use the Kirchhoff transformation, while maintaining the remaining part unaltered.

4. Discussion and conclusions

Despite its simplicity, the elementary example just discussed gives an immediate, physically based, interpretation of the Kirchhoff transformation. The static and kinematic equivalence of various systems of forces and torques at the border, obtained through the notion of effective shear, is a straightforward consequence of the basic assumptions that shear deformations in Kirchhoff–Love plates are null. Such an equivalence cannot be established in Mindlin–Reissner plates, because although the aforementioned equivalent systems have the same resultant and the same moment-resultant, they are associated with different types of shear deformations that this model can detect.

Indeed, there are infinite boundary data that are compatible with the same deformation of Kirchhoff–Love plates, i.e., those which give the same result when the Kirchhoff transformation is applied. This is somehow a limit of the theory, but it would be erroneous to conclude, as is sometimes done in the technical literature [Vasil'ev 2012], that this theory is compatible with the only boundary datum that results from Kirchhoff transformation. The elementary example just illustrated shows that Kirchhoff transformation simply establishes an equivalence of various systems of forces, but does not select among these a privileged one.

In particular, the shear-stiffness assumption of Kirchhoff–Love plates allows for the possibility of lumped forces at the corners, but this is not a paradox of the theory [Alfutov 1992]. The partition *à la* Grashof allows one to recognize that there is a thin layer in proximity to the boundary where, due to the aforementioned shear stiffness, there is a transformation of the bending with shear (produced by the concentrated forces) into pure bending in the neighboring internal portions. Therefore, there is no paradox in the classical solution of a Kirchhoff–Love plate twisted by concentrated forces at the corners, where the borders are stress-free, but the torque per unit length is nonzero on fibers parallel to the borders, at an arbitrarily small distance.

However, the example has shown that this transformation is possible only at the price of infinite shear stresses occurring in a boundary layer of evanescent thickness in proximity to the borders. Indeed, the assumption of Kirchhoff–Love theory is that (transverse) shear deformations are negligibly small and, accordingly, they are assumed to be null: this implies the plate to be shear-rigid. The latter hypothesis is certainly correct in most cases of the practice, where shear stresses remain finite, but in the case of concentrated forces the shear stress becomes infinite.

Therefore, Kirchhoff–Love theory cannot consistently be applied when the border presents sharp corners with concentrated forces, because these would generate infinite shear stress, regardless of the thickness of the plate. In fact, the formation of a boundary layer [Lobkovsky 1996] cannot be neglected. For such cases a more refined theory, possibly accounting for shear deformations like Mindlin and Reissner's, appears to be necessary to reproduce the actual "diffusion" of such forces inside the body.

Acknowledgement

References

[Alfutov 1992] N. A. Alfutov, "On paradoxes of the theory of thin elastic plates", *Mech. Solids* **3** (1992), 65–72.

[Belluzzi 1986] O. Belluzzi, *Scienza delle costruzioni*, vol. 3, Zanichelli, Bologna, 1986.

[Ciarlet 1997] P. G. Ciarlet, *Mathematical elasticity, 2: Theory of plates*, Studies in Mathematics and its Applications **27**, North-Holland, Amsterdam, 1997.

[Fosdick and Royer-Carfagni 2015] R. Fosdick and G. Royer-Carfagni, "Singular shear-force states in elementary plate theory", *J. Elasticity* **118**:1 (2015), 89–99.

[Friedrichs and Dressler 1961] K. O. Friedrichs and R. F. Dressler, "A boundary-layer theory for elastic plates", *Comm. Pure Appl. Math.* **14**:1 (1961), 1–33.

[Friesecke et al. 2006] G. Friesecke, R. D. James, and S. Müller, "A hierarchy of plate models derived from nonlinear elasticity by gamma-convergence", *Arch. Ration. Mech. Anal.* **180**:2 (2006), 183–236.

[Gol'denveizer and Kolos 1965] A. L. Gol'denveizer and A. V. Kolos, "К построению двумерных уравнений теории упругих тонких пластинок", *Prikl. Mat. Mekh.* **29**:1 (1965), 141–155. Translated as "On the derivation of two-dimensional equations in the theory of thin elastic plates" in *J. Appl. Math. Mech.* **29**:1 (1965), 151–166.

[Grashof 1878] F. Grashof, *Theorie der Elasticität und Festigkeit*, Gaertner, Berlin, 1878.

[Kirchhoff 1850] G. Kirchhoff, "Über das Gleichgewicht und die Bewegung einer elastischen Scheibe", *J. Reine Angew. Math.* **40** (1850), 51–58.

[Lobkovsky 1996] A. E. Lobkovsky, "Boundary layer analysis of the ridge singularity in a thin plate", *Phys. Rev. E* **53**:4 (1996), 3750–3759.

[Mindlin 1951] R. D. Mindlin, "Influence of rotatory inertia and shear on flexural motions of isotropic, elastic plates", *J. Appl. Mech.* **18** (1951), 31–38.

[Podio-Guidugli 1989] P. Podio-Guidugli, "An exact derivation of the thin plate equation", *J. Elasticity* **22**:2-3 (1989), 121–133.

[Poisson 1829] S. D. Poisson, "Mémoire sur l'équilibre et le mouvement des corps élastiques", *Mém. Acad. Sci. Paris* **18** (1829), 357–570.

[Reissner 1945] E. Reissner, "The effect of transverse shear deformation on the bending of elastic plates", *J. Appl. Mech.* (A) **12** (1945), 69–77.

[Thomson and Tait 1883] W. Thomson and P. Tait, *Treatise on natural philosophy, part 2*, Cambridge University Press, 1883.

[Timoshenko 1940] S. Timoshenko, *Strength of materials*, 2nd ed., Van Norstad, New York, 1940.

[Timoshenko and Woinowsky-Krieger 1959] S. Timoshenko and S. Woinowsky-Krieger, *Theory of plates and shells*, 2nd ed., McGraw-Hill, New York, 1959.

[Vasil'ev 2012] V. V. Vasil'ev, "Kirchhoff and Thomson–Tait transformations in the classical theory of plates", *Mech. Solids* **47**:5 (2012), 571–579.

[Zhilin 1995] P. A. Zhilin, "On the classical plate theory and the Kelvin–Tait transformation", *Mech. Solids* **30** (1995), 124–129.

LAURA GALUPPI: laura.galuppi@unipr.it
Dipartimento di Ingegneria Industriale, Università degli Studi di Parma, Parco Area delle Scienze 181/A, I-43124 Parma, Italy

GIANNI ROYER-CARFAGNI: gianni.royer@unipr.it
Dipartimento di Ingegneria Industriale, Università degli Studi di Parma, Parco Area delle Scienze 181/A, I-43124 Parma, Italy

msp

SUBMISSION GUIDELINES

ORIGINALITY

Authors may submit manuscripts in PDF format online at the Submissions page. Submission of a manuscript acknowledges that the manuscript is original and has neither previously, nor simultaneously, in whole or in part, been submitted elsewhere. Information regarding the preparation of manuscripts is provided below. Correspondence by email is requested for convenience and speed. For further information, write to contact@msp.org.

LANGUAGE

Manuscripts must be in English. A brief abstract of about 150 words or less must be included. The abstract should be self-contained and not make any reference to the bibliography. Also required are keywords and subject classification for the article, and, for each author, postal address, affiliation (if appropriate), and email address if available. A home-page URL is optional.

FORMAT

Authors can use their preferred manuscript-preparation software, including for example Microsoft Word or any variant of TEX. The journal itself is produced in LATEX, so accepted articles prepared using other software will be converted to LATEX at production time. Authors wishing to prepare their document in LATEX can follow the example file at www.jomms.net (but the use of other class files is acceptable). At submission time only a PDF file is required. After acceptance, authors must submit all source material (see especially Figures below).

REFERENCES

Bibliographical references should be complete, including article titles and page ranges. All references in the bibliography should be cited in the text. The use of BibTEX is preferred but not required. Tags will be converted to the house format (see a current issue for examples); however, for submission you may use the format of your choice. Links will be provided to all literature with known web locations; authors can supply their own links in addition to those provided by the editorial process.

FIGURES

Figures must be of publication quality. After acceptance, you will need to submit the original source files in vector format for all diagrams and graphs in your manuscript: vector EPS or vector PDF files are the most useful. (EPS stands for Encapsulated PostScript.)

Most drawing and graphing packages—Mathematica, Adobe Illustrator, Corel Draw, MATLAB, etc.—allow the user to save files in one of these formats. Make sure that what you're saving is vector graphics and not a bitmap. If you need help, please write to graphics@msp.org with as many details as you can about how your graphics were generated.

Please also include the original data for any plots. This is particularly important if you are unable to save Excel-generated plots in vector format. Saving them as bitmaps is not useful; please send the Excel (.xls) spreadsheets instead. Bundle your figure files into a single archive (using zip, tar, rar or other format of your choice) and upload on the link you been given at acceptance time.

Each figure should be captioned and numbered so that it can float. Small figures occupying no more than three lines of vertical space can be kept in the text ("the curve looks like this:"). It is acceptable to submit a manuscript with all figures at the end, if their placement is specified in the text by means of comments such as "Place Figure 1 here". The same considerations apply to tables.

WHITE SPACE

Forced line breaks or page breaks should not be inserted in the document. There is no point in your trying to optimize line and page breaks in the original manuscript. The manuscript will be reformatted to use the journal's preferred fonts and layout.

PROOFS

Page proofs will be made available to authors (or to the designated corresponding author) at a Web site in PDF format. Failure to acknowledge the receipt of proofs or to return corrections within the requested deadline may cause publication to be postponed.

Journal of Mechanics of Materials and Structures